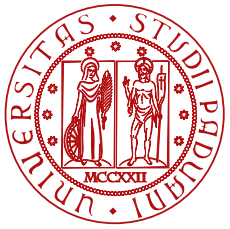

Università degli Studi di Padova

Dipartimento di Ingegneria dell'Informazione

Master Thesis in ICT for Internet and Multimedia

Optical Disordered Materials for Passive Radiative Cooling

Master Candidate

Atakan Erdogan

Student ID 2108648

Supervisor

Prof. Maria-Guglielmina Pelizzo

University of Padova

Co-supervisor

Dr. Giuseppe Emanuele Lio.

University of Florence

Academic Year
2024/2025

Abstract

Passive radiative cooling is a novel approach to thermal management that enables surfaces to achieve sub-ambient temperatures by naturally emitting heat into outer space while minimizing solar heat gain through broadband reflection across the solar spectrum, all without requiring any electrical energy input. This dual functionality can be effectively achieved by using irregular materials that promote multiple scattering and spectrally selective light transport of micro- and nanoscale structures, thereby increasing the performance of reflection in the solar spectrum, and particularly the IR emission ratio in the atmospheric window (8–13 μm) where thermal radiation escapes with minimal absorption. In this thesis, experimental characterization of hybrid coatings combining commercial paint matrices with nanoporous polymer films was carried out, demonstrating high solar reflectance, strong mid-infrared emissivity, and measurable sub-ambient cooling under outdoor conditions. These investigations included optical, morphological, and thermal analyses that established the feasibility and performance limits of scalable PRC coatings. Based on the insights gained from this experimental part of our studies, this thesis then advances towards a simulation-based design of polymer-based disordered optical coatings composed of boron nitride nanofibers embedded in a low-index matrix, demonstrating how their volumetric scattering and refractive index contrast can be tuned through multi-layer or graded single-layer architectures to achieve higher solar reflectance and selective mid-infrared emission under realistic illumination conditions.

Sommario

Il raffreddamento radiativo passivo è un nuovo approccio alla gestione termica che consente alle superfici di raggiungere temperature inferiori a quelle ambientali emettendo calore in modo naturale nello spazio esterno e riducendo al minimo l'accumulo di calore solare attraverso la riflessione a banda larga su tutto lo spettro solare, il tutto senza richiedere alcun apporto di energia elettrica. Questa doppia funzionalità può essere efficacemente ottenuta utilizzando materiali irregolari che favoriscono la diffusione multipla e il trasporto spettralmente selettivo della luce di strutture su scala micro e nanometrica, aumentando così le prestazioni di riflessione nello spettro solare e, emissivita IR nella finestra atmosferica (8–13 μm) dove la radiazione termica fuoriesce con un assorbimento minimo. In questa tesi è stata effettuata la caratterizzazione sperimentale di rivestimenti ibridi che combinano matrici di vernici commerciali con film polimerici nanoporosi, dimostrando un'elevata riflettanza solare, una forte emissività nell'infrarosso medio e un raffreddamento misurabile al di sotto della temperatura ambiente in condizioni esterne. Queste indagini hanno incluso analisi ottiche, morfologiche e termiche che hanno stabilito la fattibilità e i limiti prestazionali dei rivestimenti PRC scalabili. Sulla base delle conoscenze acquisite dalla parte sperimentale dei nostri studi, questa tesi procede poi verso una progettazione basata sulla simulazione di rivestimenti ottici disordinati a base di polimeri composti da nanofibre di nitruro di boro incorporate in una matrice a basso indice, dimostrando come la loro dispersione volumetrica e il contrasto dell'indice di rifrazione possano essere regolati attraverso architetture multistrato o monostrato graduato per ottenere una maggiore riflettanza solare e un'emissione selettiva nell'infrarosso medio in condizioni di illuminazione realistiche.

Contents

List of Figures

List of Tables

List of Code Snippets

List of Acronyms

RC Radiative Cooling

PDRC Passive Daytime Radiative Cooler

PRC Passive Radiative Cooling

UV Ultraviolet

UV-Vis Ultraviolet – Visible

NIR Near Infrared Region

IR Infrared Region

MIR Mid-Infrared Region

LWIR Long Wave Infrared

EM Electromagnetic

AFM Atomic Force Microscopy

IEA International Energy Agency

Ag Silver

Al Aluminum

ALD Atomic Layer Deposition

BN Boron Nitride

CIE Commission Internationale de l'Éclairage

CubeSat Cube Satellite

DBR Distributed Bragg Reflector

DMD Dielectric–Metal–Dielectric

FDTD Finite-Difference Time-Domain

FE-SEM Field-Emission Scanning Electron Microscopy

FoM Figure of Merit

FTIR Fourier-Transform Infrared Spectroscopy

HfO2 Hafnium Dioxide

hBN Hexagonal Boron Nitride

HMM Hyperbolic Metamaterial

MLI Multi-Layer Insulation

MIR Mid-Infrared

NIPS Non-solvent Induced Phase Separation

PAN Polyacrylonitrile

PE Polyethylene

PMMA Poly(methyl methacrylate)

PTFE Polytetrafluoroethylene

PVDF-HFP Poly(vinylidene fluoride-co-hexafluoropropylene)

RCWA Rigorous Coupled-Wave Analysis

SEM Scanning Electron Microscopy

SiC Silicon Carbide

SiO2 Silicon Dioxide

Si3N4 Silicon Nitride

SPhP Surface Phonon Polariton

SoA State of the Art

TARC Temperature-Adaptive Radiative Coating

TASC Thermally Adaptive Smart Coating

TE Transverse Electric (polarization)

TiO2 Titanium Dioxide

TM Transverse Magnetic (polarization)

TIPS Thermally Induced Phase Separation

TMM Transfer Matrix Method

ZFLO Zone-Folded Longitudinal Optical (phonon mode)

ATR Attenuated Total Reflectance

Au Gold

DRA Diffuse Reflectance Accessory

EPS Expanded Polystyrene

LED Light Emitting Diode

NA Numerical Aperture

NPF Nanoporous Film

NTC Negative Temperature Coefficient

PID Proportional Integral Derivative

PMT Photo Multiplier Tube

PVC Polyvinyl Chloride

VOC Volatile Organic Compounds

COMSOL COMSOL Multiphysics

FEM Finite Element Method

5LS Five-Layer Stacked

DtC Dense-to-Coarse

EWFD Electromagnetic Waves, Frequency Domain

PML Perfectly Matched Layer

SWR Solar-Weighted Reflectance

AM1.5G Air Mass 1.5 Global solar spectrum

AW Atmospheric Window

XRD X-Ray Diffraction

TEM Transmission Electron Microscopy

EDS Energy Dispersive X-Ray Spectroscopy

FAFM Flexible Alumina Fiber Membrane

GNM Graded Nanocomposite Metamaterial

HGPM Hierarchical Gradient Porous Metamaterial

1 Introduction

Cooling is a significant end-use of energy globally, and from logistics to portable technologies, from personal living spaces to data centers, cooling and cooling technologies are emerging as an important need in many areas and sectors around the world. Conventional cooling systems currently in use are one of the major drivers of electricity consumption. According to data from the International Energy Agency, demand for space cooling alone is expected to more than double by 2050. This growth will place serious pressure on energy consumption, causing electricity demand to peak during the summer months in particular. Cooling needs are no longer just a matter of comfort; they have become a fundamental requirement for economic efficiency, food and drug safety, data processing capacity, and industrial production.

The cooling methods commonly used today are largely mechanical systems that rely on electrical energy. These systems place a significant load on power grids, especially during periods of heavy use, and cause high levels of greenhouse gas emissions due to the fossil fuels used in energy production. Estimates indicate that these methods account for approximately 15% of global electricity consumption and contribute significantly to carbon emissions. Additionally, the impact of the refrigerant gases used on the ozone layer and global warming, independent of energy consumption, contributes to an increase in environmental burden.

In recent years, technological developments aimed at increasing energy efficiency and reducing environmental impact have gained momentum. Significant progress has been made in high-efficiency compressors, advanced heat

exchanger designs, and more environmentally friendly refrigerants. However, even these innovations cannot completely eliminate energy dependence. Additionally, the rapidly increasing penetration of air conditioning, particularly in developing countries, is making it challenging to balance these gains on a global scale. Therefore, the need for alternative cooling approaches that do not strain the electrical grid, require minimal maintenance, and have minimal environmental impact is becoming increasingly prominent.

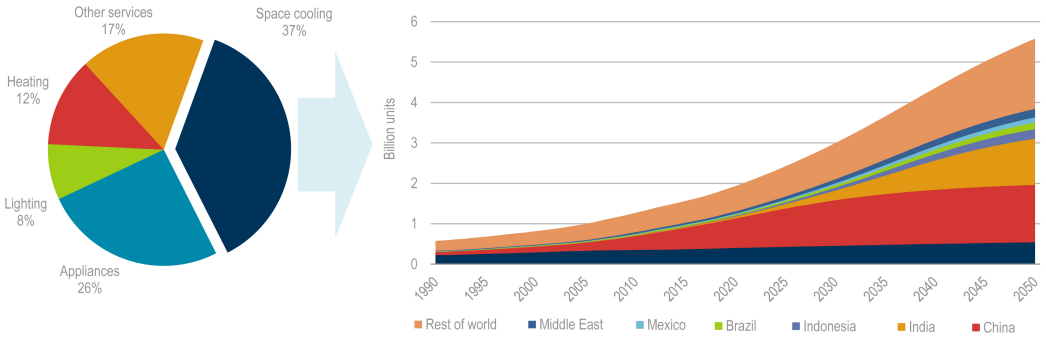

Figure 1.1: Distribution of increase in final demand for electricity in homes by 2050 (%) and increase in the number of air conditioners by country (billion units) [1].

In this context, innovative cooling solutions can both reduce energy consumption and play an important role in combating climate change. Passive cooling techniques based on the principles of reflecting sunlight and directly transferring heat into space can reduce surface temperatures without requiring energy input. As a result, they have the potential to reduce both energy costs and carbon emissions. In regions with favorable climatic conditions, such solutions can form the foundation of a long-term and sustainable cooling strategy.

Passive Radiative Cooling (PRC) enables surfaces to dissipate heat into space through the 8–13 μm atmospheric window without energy input, while also reflecting a large portion of solar radiation. This thesis investigates optical coating designs and materials to enhance PRC performance, with the aim of achieving high reflectivity and selective thermal emission by optimizing structure, optical properties, and geometry through combined electromagnetic modeling and thermal analysis.

The experimental part of this work was carried out through a collaboration between the University of Florence and the University of Padova. Our efforts focused on fabricating and testing nanoporous film–based coatings and glass

bubble–enhanced paint systems. Optical and morphological analyzes were performed at CNR-IFN LUXOR in Padova, while samples were prepared and outside cooling tests were carried out in Florence. These experiments demonstrated sub-ambient cooling in paint-like PRC systems and highlighted the limitations of common testing configurations.

Building on these results, the second stage addressed simulation-driven optimization. Using COMSOL Multiphysics, we modeled multilayer disordered coatings with boron nitride nanofiber scatterers embedded in polymer matrices. Two architectures, a five-layer stacked (5LS) and a dense-to-coarse (DtC) gradient, were designed to ensure broadband solar reflectance and selective emissivity in the atmospheric transparency window. Iterative improvement of structural parameters through simulations is aimed at providing guidelines for scalable, high-performance PRC coatings.

Together, in the hands-on experimental program (reported in Chapter 2) and in the COMSOL-based numerical optimization (reported in Chapter 4) form a coherent research trajectory from proof-of-concept fabrication to predictive design and engineering of high-performance passive radiative cooling systems.

The thesis is organized as follows:

- **Chapter 1:** introduction.
- **Chapter 2:** It presents a state-of-the-art review of Passive Radiative Cooling technologies, focusing on recent advances and representative modern implementations.
- **Chapter 3:** It reports the experimental investigation of our hybrid PRC system combining nanoporous polymer films with reflective paint coatings, describing the fabrication process, optical and thermal characterization, and outdoor measurements that demonstrate high solar reflectance, strong mid-infrared emissivity, and sub-ambient cooling performance.
- **Chapter 4:** It gives the details of the numerical modeling of disordered multilayer structures using FEM-based simulations, discussing parametric sweeps and design optimizations in COMSOL Multiphysics, presents the post-process using MATLAB, and shows the results of our state-of-the-art studies.
- **Chapter 5:** discussion and conclusion.

2

Theory and Technologies for Passive Radiative Cooling

In this chapter, we present the fundamental principles and performance criteria of Passive Radiative Cooling (PRC) systems and review the state-of-the-art material strategies that have emerged in recent years. We discuss the optical and thermal mechanisms of PRC systems, their scalability, and comparisons of performance criteria, ranging from multilayer photonic coatings to paint and polymer-based systems, as well as the bio-based methods.

2.1 Principles and Metrics of Passive Radiative Cooling

Passive Radiative Cooling (PDRC) is fundamentally governed by the balance of radiative and non-radiative heat fluxes between a surface and its surroundings. The central idea is to exploit the natural transparency of the Earth's atmosphere in the mid-infrared (MIR) region (8–13 µm), known as the *atmospheric window*, to radiate thermal energy directly into outer space. Simultaneously, the material must suppress solar absorption (0.3–2.5 µm) to prevent heating under direct sunlight.

2.1.1 Radiative Heat Exchange Fundamentals

The net cooling power of a PDRC surface at temperature T under ambient temperature T_{amb} can be expressed as:

$$P_{\text{net}}(T) = P_{\text{rad}}(T) - P_{\text{atm}}(T_{amb}) - P_{\text{sun}} - P_{\text{nonrad}} \tag{2.1}$$

where:

- $P_{\text{rad}}(T)$: thermal radiation emitted by the surface into the atmosphere,
- $P_{\text{atm}}(T_{amb})$: downwelling atmospheric thermal radiation absorbed by the surface,
- P_{sun}: absorbed solar irradiance,
- P_{nonrad}: non-radiative parasitic heat gains (conduction, convection).

The spectral radiance of the surface emission is governed by Planck's law:

$$I_\lambda(T) = \frac{2hc^2}{\lambda^5} \cdot \frac{1}{\exp\left(\frac{hc}{\lambda k_B T}\right) - 1} \tag{2.2}$$

and the total radiative power is determined by integrating over all wavelengths and solid angles, weighted by the spectral emissivity $\varepsilon(\lambda, \theta)$.

The ideal design condition for a PDRC material can thus be expressed as:

$$\varepsilon(\lambda) \approx 1 \quad \text{for } \lambda \in [8, 13]\ \mu\text{m}, \quad R(\lambda) \approx 1 \quad \text{for } \lambda \in [0.3, 2.5]\ \mu\text{m} \tag{2.3}$$

That is, the ideal cooler acts as an infrared blackbody in the MIR and as a solar mirror in the visible–NIR range [2, 3].

2.1.2 Atmospheric Window and Radiative Pathways

The 8–13 µm atmospheric window is the most exploited spectral range for PDRC, as water vapor and CO_2 absorption are minimal in this region. However, recent studies suggest that the 13–20 µm "second window" could also be harnessed, especially in dry and high-altitude climates, potentially enhancing cooling capacity [4].

The radiative pathway is strongly influenced by local atmospheric conditions:

- **Humidity**: increases IR absorption, reducing cooling potential,
- **Cloud coverage**: blocks the atmospheric window,
- **Elevation**: improves radiative cooling efficiency by reducing air mass.

These dependencies highlight the need to couple material design with climatic and geographic considerations.

2.1.3 Figures of Merit (FoM) in PDRC

Several Figures of Merit have been introduced to compare different PDRC materials:

1. **Steady-State Temperature Drop (ΔT)**

$$\Delta T = T_{amb} - T_{eq} \tag{2.4}$$

   where T_{eq} is the equilibrium temperature when $P_{\text{net}}(T_{eq}) = 0$. This is simple but highly setup-dependent.

2. **Net Cooling Power (P_{net})** Reported in W/m^2, often at fixed solar irradiance (1000 W/m^2) and ambient temperature (300 K). A rigorous metric that accounts for both optical and thermal properties.

3. **Cooling Figure of Merit (FoM_c)**

$$\text{FoM}_c = \frac{P_{\text{net}}}{P_{\text{rad,ideal}}} \tag{2.5}$$

   where $P_{\text{rad,ideal}}$ is the theoretical maximum blackbody emission in the atmospheric window. Enables normalized comparison across climates and setups.

4. **Spectral Selectivity Ratio** Ratio of average emissivity in the MIR window to average absorptivity in the solar band. Highlights the trade-off between selectivity and broadband response.

5. **Environmental Durability Index (emerging)** Combines optical FoMs with resistance to UV, soiling, and mechanical wear.

2.1.4 Selective vs. Broadband Radiative Cooling

Two main design philosophies exist:

- **Selective Emitters**: multilayer dielectric stacks engineered for sharp emission in 8–13 µm. They provide high peak efficiency but are sensitive to atmospheric variations [2].
- **Broadband Emitters**: disordered porous polymers and $BaSO_4$-based coatings that emit across the full IR spectrum. While theoretically less efficient, they are more robust to humid or polluted environments [5, 6, 7].

In practice, selective designs excel in controlled, dry climates, whereas broadband designs are advantageous in real-world, variable conditions. This trade-off is central to the development of scalable PDRC technologies.

2.2 Photonic and Multilayer Structures

Multilayer photonic coatings constitute the most spectrally precise class of passive daytime radiative coolers. By tailoring interference in stratified dielectrics over a metallic back-reflector, these devices simultaneously suppress solar absorption (0.3–2.5 µm) and enhance emissivity within the atmospheric window (8–13 µm). The approach set the first practical benchmark for daytime sub-ambient operation and continues to anchor the performance ceiling against which scalable broadband solutions are compared [2, 3, 8].

2.2.1 Families of Photonic Radiative Coolers and Their State of the Art

Planar multilayers (dielectric/metal/dielectric)

Planar HfO_2/SiO_2 stacks on Ag demonstrated sub-ambient cooling of ~5 K and field net powers on the order of 40–60 W m^{-2}, establishing the feasibility of selective daytime radiative cooling in outdoor conditions [2].

Subsequent research moved in several directions. One line of work aimed at lowering the number of dielectric layers while still preserving high spectral selectivity, for example by using TiO_2/SiO_2 sputtered stacks. Another direction focused on replacing silver with more chemically stable metals such as

aluminum, accepting a slight penalty in near-infrared reflectance for improved durability. A third avenue explored aperiodic or needle-optimized multilayer sequences, designed to flatten the solar stopband while positioning narrow infrared resonances precisely within the 8–13 µm atmospheric window [8].

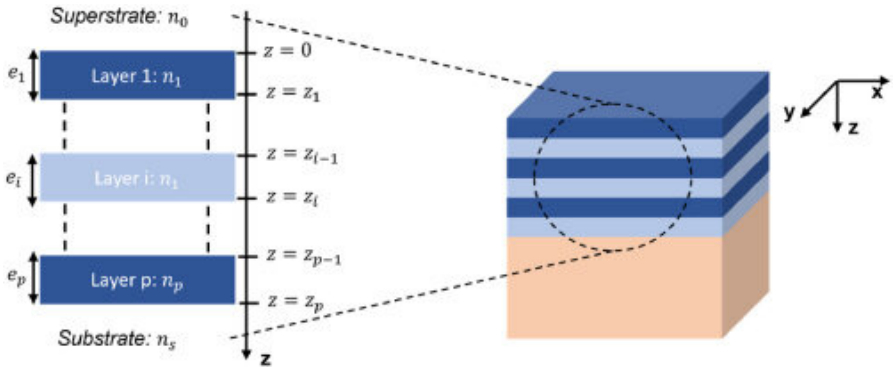

Figure 2.1: General structure of a multilayer stack.

More recently, cost-oriented designs have investigated compact inorganic stacks such as $Si_3N_4/SiO_2/Al_2O_3/Si_3N_4$ deposited on aluminum, which have already demonstrated measurable sub-ambient performance. These results point to a possible pathway toward lower-cost but still selective multilayer emitters [4].

Photonic crystals and quasi-periodic stacks

Photonic crystals extend selectivity by engineering bandgaps and resonance densities beyond 1D. Early 2D/"chirped" photonic-crystal concepts combined phonon-polaritonic emitters with dielectric reflectors to maximize window emissivity while minimizing solar absorption; these ideas underpin many SoA numerical optimizations for selective emitters [9, 10]. Quasi-periodic aperiodic stacks further relax periodicity to place multiple MIR resonances while retaining a wide solar stopband; theoretical designs report sub-ambient potential with reduced layer counts and broadened angle tolerance [11, 12]. Silicon carbide (SiC) is used to create photonic crystal structures. Below, it is shown its usage in stack structure.

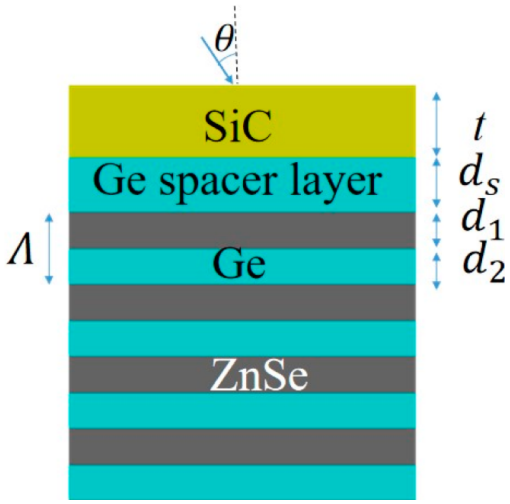

Figure 2.2: Cross-section view of the thermal emitter based on SiC film with DBR reflector [9].

Metasurfaces and resonant selective emitters

Metasurfaces add resonant degrees of freedom through subwavelength unit cells on top of (or instead of) planar stacks. This enables engineered emissivity lineshapes, polarization/angle control, and multifunctionality (e.g., color with cooling). SoA studies report selective emitters using TiO_2/SiO_2 or SiO_2/Si_3N_4 meta-resonators that preserve high $\overline{R}_{\odot}$ while forming narrow MIR bands. Recent double-layer SiO_2/TiO_2 "metamaterial" emitters have been numerically and experimentally explored for stronger window-selective emission with simplified stacks, though fabrication sophistication and scalability remain open issues [13, 8].

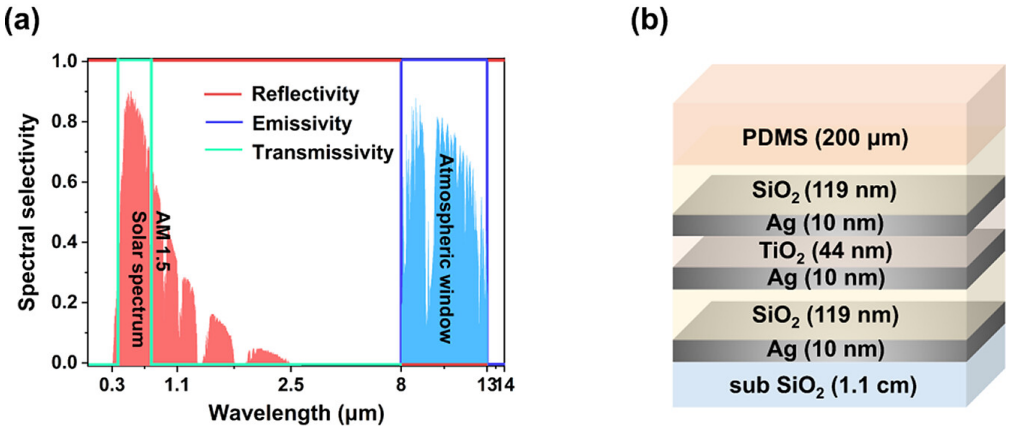

Figure 2.3: Reflection, transmission, and emissivity spectra of the ideal transparent radiative cooler. (b) Structural diagram of the HMMs glass.

Angular robustness and hemispherical performance

A recognized gap between lab-grade spectra and outdoor performance is angular sensitivity. SoA approaches incorporate graded-index caps, weakly scattering topographies, or meta-units with flattened dispersion to reduce the degradation of hemispherical figures (angle-weighted $\langle R \rangle$ and $\langle \varepsilon \rangle$) under diffuse skylight. Reviews now classify multilayer/photonic-crystal/metasurface strategies by their angle dependence and propose standardized reporting of hemispherical metrics to ensure fair benchmarking [8, 14, 15].

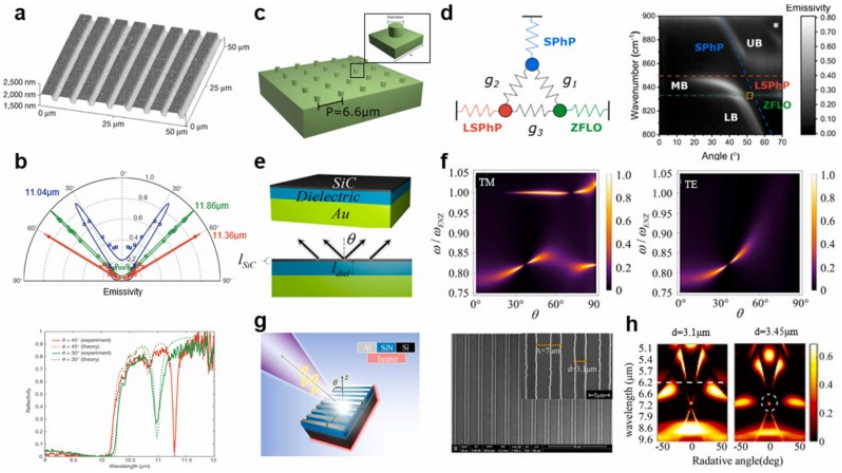

Figure 2.4: Narrowband directional emission with rainbow effect. (a) 3D profile of a SiC metagrating characterized via atomic force microscopy. (b) The theoretical and experimental emissivity of the grating in p-polarization. (c) Illustration of 4H-SiC emission structure on 6.6 μm pitches exciting hybrid propagating SPhPs, localized SPhPs, and ZFLO modes. (d) The experimental angular dispersion relations for 2D nanostructured arrangements at p-polarization. (e) Layered 2D structure and labeled parameters. (f) TM (left) and TE (right) emissivity of SiC/air/gold multilayer film in SiC SPhPs spectral region, with $l_{diel} = 3.5\,\frac{\lambda_{ENZ}}{4}$. (g) Schematic plot and scanning electron microscopy (SEM) images for Al grating-SiN-Si sandwiched structure. (h) Measured angle-dependent spectral emissivity for gratings with a constant period and different widths [16].

2.2.2 Performance Benchmarks and Comparative Landscape

Representative devices consistently report near-unity solar reflectance, sharp MIR emissivity features, and daytime ΔT of 3–5 K with net powers of tens of W m^{-2} in clear-sky testing [2, 8]. The broader SoA, however, shows diversification rather than raw performance gains: colored/metasurface designs deliver architectural compatibility at small penalties in $\overline{R}_{\odot}$; quasi-periodic stacks reduce

layer counts; semi-transparent multilayers target window integration; and cost-oriented inorganic stacks explore Al-based reflectors and simplified dielectrics while preserving selectivity [4, 11, 17, 18]. Table 2.1 collates representative SoA exemplars across these families.

Table 2.1: Representative state-of-the-art photonic/multilayer radiative coolers: device families, design levers, and reported highlights.

Family	Design levers	Reported highlights
Planar aperiodic multilayers	HfO_2/SiO_2, TiO_2/SiO_2 on Ag/Al; needle optimization; TMM	ΔT ~3–5 K; 40–60 $W\,m^{-2}$; earliest daytime proof; recent cost-focused $Si_3N_4/SiO_2/Al_2O_3$ stacks [2, 8]
Photonic crystals / quasi-periodic stacks	Chirped/graded periods; bandgap placement; angle-tolerant modes	Theoretical/experimental routes to fewer layers and improved angular tolerance; selective MIR bands with solar stopbands [11]
Metasurfaces (resonant selective emitters)	Subwavelength resonators; dispersion control; RCWA/FDTD co-design	Tunable emissivity lineshapes, polarization/angle control; fabrication complexity still a barrier [8, 13]
Colored selective coolers	Interferometric structural color; DMD cavities; color–cooling co-optimization	~4 K sub-ambient under >1000 $W\,m^{-2}$ with vivid colors; design maps for gamut vs. $\overline{R}_\odot$ [19, 17, 20]
Semi-transparent multilayers (windows)	NIR-reflecting photonic stacks + MIR emissive layers	Visible-transmissive radiative cooling windows; façade integration prospect [18, 21]

2.3 Disordered Materials for PRC

Disordered materials constitute the backbone of scalable PDRC and our both experiments and simulation-based studies as well. Their efficiency arises from random particle ensembles and porous morphologies, which naturally broaden the scattering spectrum and stabilize performance against angular or fabrication variations. Unlike photonic multilayers, whose performance strongly depends on precise stacking, disordered systems maintain functionality even with imperfections and are therefore more compatible with real-world operating conditions. The detailed representation of this method, which must be examined across a broad spectrum ranging from paint-based solutions that form the ba-

sis of our experimental study to the disordered and multilayered use of nanostructured particles that shed light on our simulation-based work, is provided in the following sections.

2.3.1 Particle-Based Paints

Particle-based paints and coatings represent the most practical and scalable PDRC solution: high-index dielectric particles dispersed in a polymer binder generate diffuse Mie scattering of sunlight, while host and fillers provide mid-infrared emissivity. Unlike photonic multilayers requiring nanometer precision or nanoporous films dependent on controlled phase separation, paint-format approaches are fully compatible with mature industrial methods such as spray-, blade-, or roll-to-roll coating [5, 6, 7].

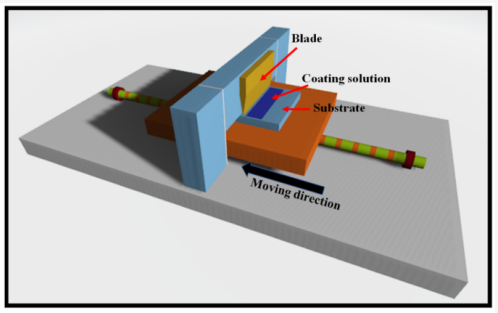

(a) Blade coating process.

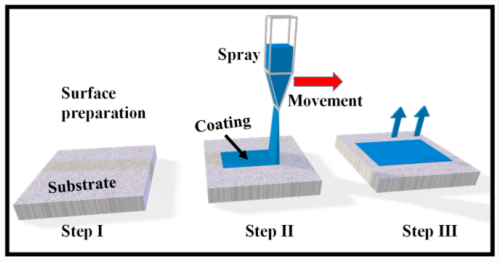

(b) Spray coating process.

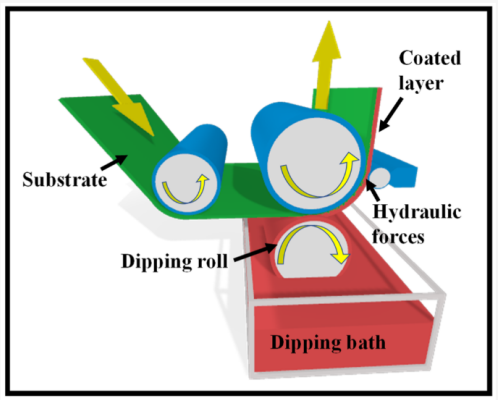

(c) Roll/dip coating process.

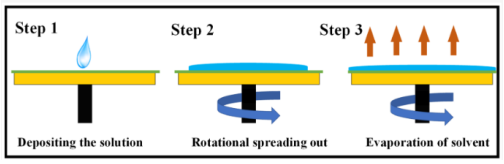

(d) Spin coating process.

Figure 2.5: Schematic illustrations of scalable coating techniques: (a) blade coating, (b) spray coating, (c) roll/dip coating, and (d) spin coating [22].

The most direct and industrially compatible pathway toward daytime sub-

ambient radiative cooling has emerged in the form of particle-filled paints, where high–index dielectric particles are dispersed in polymeric binders to create strong diffuse scattering of solar photons. The optical principle rests on Mie scattering: particle diameters on the order of the solar wavelengths ($x = 2\pi r/\lambda \sim 1$) efficiently backscatter visible and near-infrared light, while smaller particles enhance ultraviolet rejection. A polydisperse distribution therefore yields broadband solar reflectance, and high volume loadings ensure optical depth without resorting to nanometer-level structural precision. At the same time, both the matrix and fillers supply vibrational resonances in the 8–13 µm atmospheric window, enabling high emissivity. These design levers, index contrast, size distribution, and loading, form the foundation of radiative cooling paints, making them robust against angular variation and scalable by conventional paint coating methods.

A landmark demonstration was achieved with a $CaCO_3$-acrylic formulation applied by blade coating. "An infrared emissivity greater than 0.93 across the atmospheric window" was obtained, and "when backed with a silver coating, the metamaterial shows a noontime radiative cooling power of 93 W m^{-2} under direct sunshine" [5]. This study established that large-area paints with randomized particle ensembles could surpass 94% solar reflectance and achieve steady-state surface temperatures 4–5 K below ambient. More importantly, it demonstrated that precise periodic order is not necessary: particle statistics and high refractive-index contrast are sufficient to deliver performance rivaling multilayer photonic coatings.

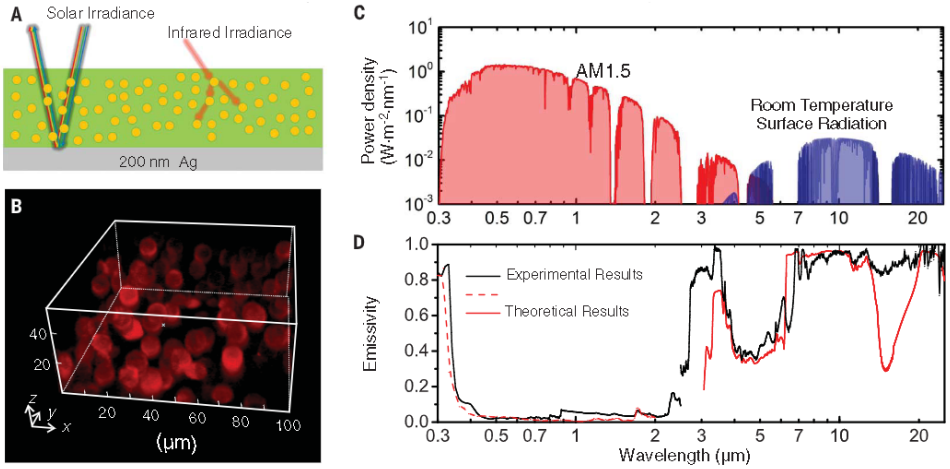

Figure 2.6: Spectroscopic response of the hybrid metamaterial: (A) schematic with silver backing, (B) confocal image showing microspheres, (C) solar and blackbody spectra, (D) measured and simulated emissivity/absorptivity [5].

Subsequent work refined these principles by pushing the optical limits of particle size engineering. By formulating a $BaSO_4$ paint with carefully chosen particle distributions around several hundred nanometers, "a solar reflectance of 98.1% and a sky window emissivity of 0.95" was achieved, with "field tests indicating surface temperatures more than 4.5 °C below ambient temperatures or an average cooling power of 117 W m^{-2}" [7]. The extremely low extinction coefficient of $BaSO_4$ in the solar band, combined with its relatively high refractive index ($n \approx 1.64$ in the visible), enabled this record performance. This "ultra-white paint" set the current benchmark for daytime PDRC paints, proving that particle size polydispersity and optimized volume fractions can drive cooling power beyond 100 W m^{-2} under AM1.5G conditions without multilayer stacks or metallic mirrors. The implication is profound: paints can define the upper end of radiative cooling performance while being deployable by conventional spray or roll-to-roll coating.

Recognizing the need for thinner and lighter coatings, specialized particle systems have also been explored. For example, "ultrawhite hBN-acrylic paints achieve solar reflectance of 97.9% and sky window emissivity of 0.83 with only 150 μm thickness" [23]. Here, the high refractive index of hexagonal boron nitride provided strong scattering with reduced areal density, while the phonon-polaritonic resonances of hBN sustained thermal emission in the window band. These paints are particularly promising for applications constrained by mass or thickness, such as lightweight building panels, vehicles, and even aerospace

structures. The ability to maintain high $\overline{R}_{\odot}$ with reduced thickness expands the design envelope of radiative cooling paints beyond architectural surfaces toward mobile and specialty use cases.

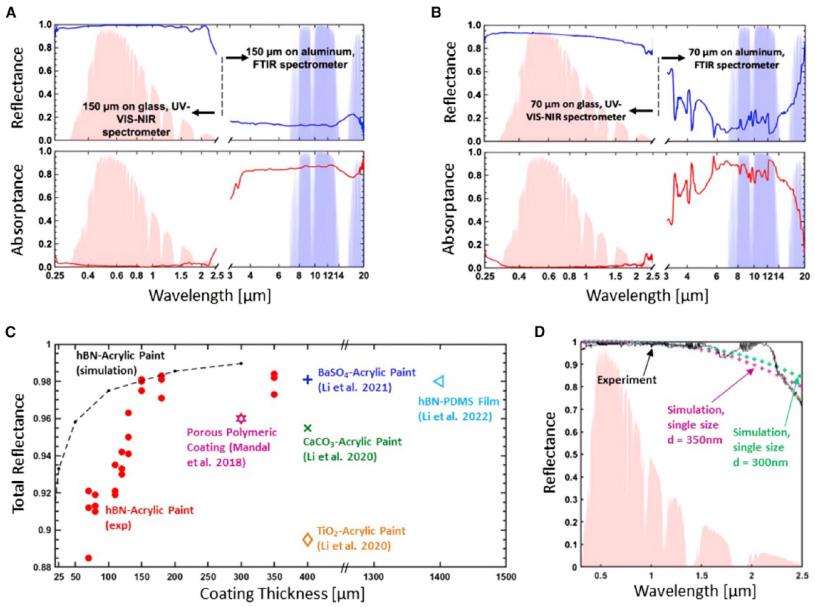

Figure 2.7: Spectral characterization of hBN–acrylic coatings: (A) 150-µm layer, (B) 70-µm layer, (C) solar reflectance vs. thickness with simulations, (D) comparison of experimental and simulated reflectance [23].

Beyond TiO_2, extensive reviews highlight that a broad range of scattering particles, including $CaCO_3$, SiO_2, and Al_2O_3, have been utilized, each with specific advantages and drawbacks [24]. TiO_2 provides strong scattering even at low filler fractions due to its high refractive index, whereas $CaCO_3$ is attractive for low-cost applications, and SiO_2 contributes low visible absorption but requires hybridization for sufficient performance. A consistent conclusion is that broadband scattering is maximized when particle sizes fall between 200 nm and 1 µm, with smaller nanoparticles risking Rayleigh-dominated losses and larger ones compromising homogeneity. The binder also emerges as a decisive factor in maintaining dispersion, preventing agglomeration, and ensuring durability. This combination of particle size engineering, refractive index contrast, and binder optimization defines the main engineering framework for scalable, high-performance particle-based disordered coatings.

Taken together, TiO_2 remains a cost-effective baseline; $BaSO_4$ systems represent industrial scalability with record optical performance; and hBN enables

lightweight, thin coatings. Across these paints, broadband solar reflectance is governed by polydisperse particle-size distributions (typically 200 nm–1 µm), high refractive-index contrast, and sufficient volume fraction, while an appropriate binder maintains dispersion and long-term durability. In practice, design objectives trade off among maximizing $R_{\odot}$, minimizing thickness/areal density, and tailoring mechanical compatibility for the target substrate.

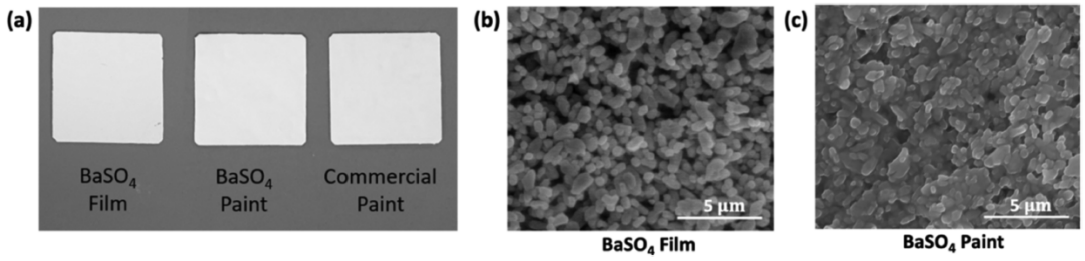

Figure 2.8: Radiative cooling coatings and SEM images. (a) $BaSO_4$ film, $BaSO_4$-acrylic paint, and commercial paint. (b) SEM image of $BaSO_4$ film. (c) SEM image of $BaSO_4$-acrylic paint. Average particle size ~398 ± 130 nm with air voids in both film and paint [7].

2.3.2 Nanoporous and Polymer–Based Architectures

Polymer-based porous coatings have been developed as an alternative to particle-based solutions in PRC, creating micro- and nanopores within polymer matrices to enhance multiple scattering in the solar spectrum while providing strong thermal emission. P(VDF-HFP) coatings achieved 96% solar reflectance and 97% emissivity with 6 °C sub-ambient cooling and ~120 W/m² cooling power [6], while PMMA coatings produced via the breath-figure method offered 5–7 °C cooling and nearly 100 W/m² power with 92–94% reflectance and >95% emissivity [25]. The high performance arises from hierarchical morphology where micro-pores enhance Mie scattering and nano-pores provide multi-directional scattering. However, limitations such as low melting temperature, UV-induced degradation, and mechanical fragility remain significant challenges, motivating the development of hybrid systems for long-term stability.

Hybrid polymer-ceramic systems have been introduced to address these weaknesses. ZrO_2 nanoparticles embedded in PVDF-HFP enhanced scattering while also improving UV and abrasion resistance, achieving 6 °C sub-ambient cooling with 97% reflectance, >95% emissivity, and 110 W/m² cooling power without deterioration after 1000 hours of UV exposure [26]. Similarly, ceramic-based

hierarchical structures such as Al_2O_3 reported record values of 99.6% solar reflectance and 97.5% infrared emission with 6 °C cooling and 120 W/m² cooling power [27]. Although ceramics deliver peak optical performance, their density and fragility limit flexible applications. To balance efficiency and durability, three-phase composites incorporating silica microspheres into polymer matrices demonstrated 8 °C cooling, 115 W/m² cooling power, and improved mechanical integrity under field conditions [28].

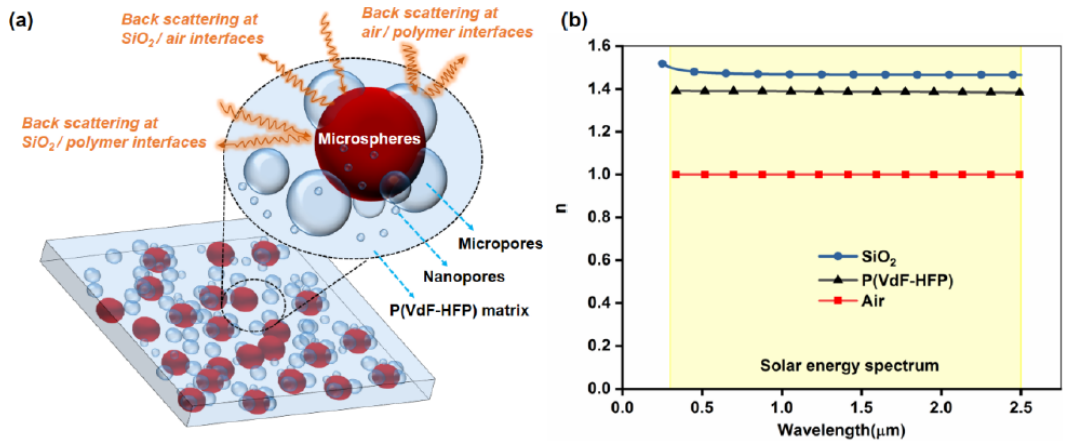

Figure 2.9: (a) Conceptual sketch of a three-phase self-assembled hybrid porous composite (air pores, silica microspheres, and polymer matrix), showing interfaces that enhance optical scattering. Silica spheres introduce additional silica/air and silica/polymer interfaces, facilitating Mie scattering and improving total solar reflection. (b) Refractive index contrast of silica and P(VDF-HFP) relative to air within the solar spectrum, indicating stronger scattering at the silica/air interface [28].

As of its flexibility and high advantage, nanoporous polymer-based strategies have expanded into wearable systems. Hierarchical metafabrics integrating nanoparticles into fibers and PTFE layers provided 5 °C sub-ambient cooling with 92.4% reflectivity and 94.5% emissivity, reducing body temperature by 3–5 °C in field tests [29]. When considered together, these results show a clear chronological progression: pure polymer coatings achieved high optical efficiency [6, 25], hybrid structures improved durability [26], ceramics reached peak optical performance [27], three-phase composites balanced efficiency and robustness [28], and textile-based approaches brought PRC to the scale of personal thermal management [29].

2.3.3 Hybrid and Hierarchical Disordered Designs

The unique contribution of hierarchical gradient porous metamaterials (HGPM) lies in their gradual morphology formed across the pore size and volume fraction, which enhances backscattering in the solar band while suppressing interface reflections in the 8–13 µm window, achieving ~97% solar reflectance, 97.6% emission, an ambient temperature difference of 8.7 °C, and 94.1 $W{\cdot}m^{-2}$ cooling power under open-air conditions [30]. In the graded nanocomposite metamaterial approach, the goal is to go beyond single-surface black bodies with a **double-sided** radiation architecture, where power densities exceeded 280 $W{\cdot}m^{-2}$ under laboratory conditions and >12 °C cooling in open air was reported [31]. Furthermore, futuristic biomimetic adaptive cooling designs aim to address the "overcooling" problem by dynamically adjusting spectral response across the day-night cycle, providing high R_{solar} and $\varepsilon_{(813\mu m)}$ during daytime while suppressing excessive radiative loss at night [32]. These approaches reveal that hierarchical, graded, and adaptive designs form a roadmap where scalability, selectivity, and comfort are integrated into PRC architectures.

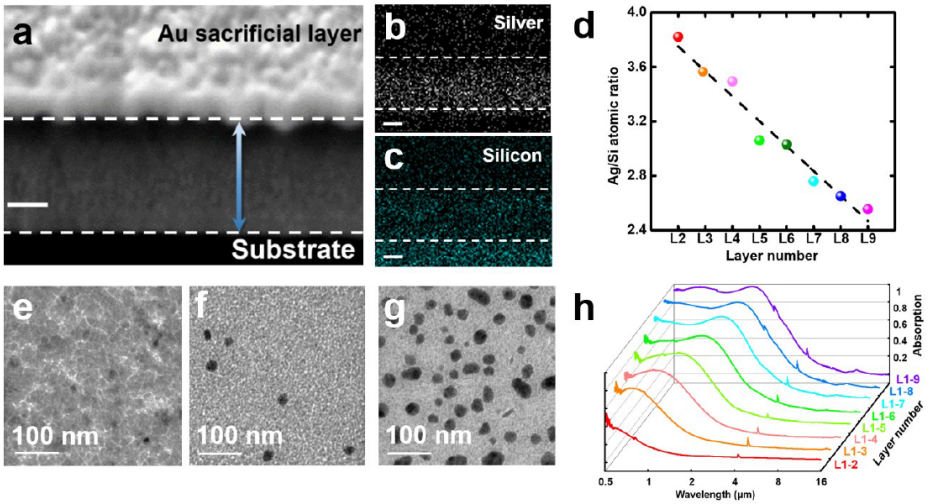

Figure 2.10: (a) SEM image of the cross section of a GNM plate. The arrow indicates the GNM region. The top Au layer is the sacrificial layer for SEM imaging. (b)-(c) EDS element mapping images for (b) Ag and (c) Si, respectively. (d) Element atomic ratio of Ag/Si for the reference sample of each layer (Layer 2 to Layer 9). (e)-(g) TEM images of three reference samples: (e) Layer 8, (f) Layer 5 and (g) Layer 3.(h) Absorption spectra of GNM samples with different numbers of stacked layers [31].

2.4 Bio-based PRC Materials

Sustainability goals and low embodied carbon targets are accelerating interest in bio-based alternatives beyond particle-based paints. Cellulose films provide strong visible backscattering and mid-IR emission while remaining lightweight, low-cost, and biodegradable [33]. Similarly, "cooling wood," achieved by lignin removal, enables panels and facades with enhanced reflectance and preserved strength. These materials can be produced by scalable methods such as molding or lamination, with performance governed by fiber and fibril architecture [34]. Current challenges lie in UV stability and outdoor durability, for which hydrophobic coatings, UV stabilizers, and layered composites are being developed [33, 35].

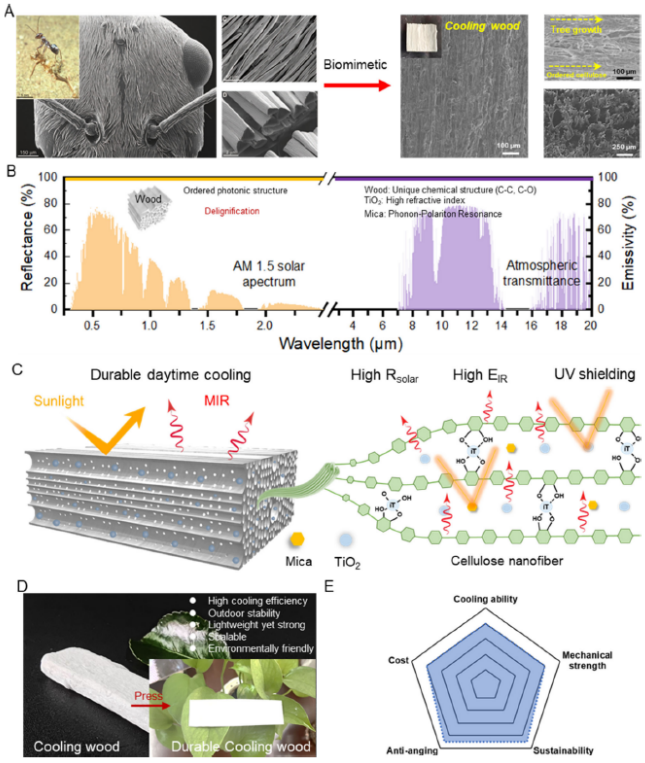

Figure 2.11: Design concept, mechanism, and advantages of durable cooling wood (DCW): (A) Bioinspired design concept of this work: learning from nature to design durable cooling wood, reproduced or adapted with permission from ref 34. Copyright 2015, The American Association for the Advancement of Science. (B) Optical optimization principle of DCW in this work. (C) Durable daytime radiative cooling mechanism. (D) Optical image of DCW. (E) Advantages of DCW [33].

Performance Benchmarks and Comparative Landscape

Among all these applications, as it is told in the last two sections, paint-based, particle-based coatings, and multilayer structures are coming to the forefront. Here is the comparison tables of each implementation methods and state-of-the-art approaches:

Table 2.2: Representative optical metrics of state-of-the-art PDRC materials (measured values as reported).

Approach / Material	$R_{\odot}$	$\varepsilon_{8-13\mu m}$	P_{net} [W/m^2]	ΔT [K]
Planar multilayer [2]	0.94	0.94	40.1	4.9
$CaCO_3$ paint [5]	0.945	0.936	93	4–5
$BaSO_4$ paint [7]	0.981	0.95	117	4.7
hBN paint [23]	0.979	0.83	60–90	3–5
NP PVDF-HFP film [6]	0.945	>0.90	>90	6
Electrospun mat [36]	0.91	0.98	80	3–4
NP-PE textile [37]	0.91	0.95	–	2–3
Glass coating [18]	–	0.90	20–50	–

3

Characterization of PRC Nanoporous Paint-Based Coatings

In this chapter, we will present the experimental study of paint-based nanoporous PRC coatings. We will report sample preparation and indexing, the optical, morphological, and thermal measurement protocols, and the resulting performance metrics in which solar-weighted reflectance, mid-IR emissivity, temperature drop ΔT, and cooling power P_{cool} of our experiments.

3.1 Sample Preperation

The experimental campaign carried out in this thesis was based on the preparation and analysis of paint-based nanoporous coatings for passive radiative cooling (PRC). The work was developed in collaboration with the University of Florence, where the samples were fabricated, while the full optical and thermal characterization was conducted in the laboratories of the University of Padova. The strategy followed a systematic approach, combining substrate engineering, controlled dispersion of scattering particles, and integration of a nanoporous polymeric film to enhance both solar reflectance and long-wave infrared emissivity.

3.1.1 Substrate Design

Two distinct metallic substrates were selected in order to provide a controlled variation in the baseline optical properties:

- **V95 substrate**: a high-reflectivity aluminum multilayer system, obtained by physical vapor deposition (PVD) of 50 nm Al, 20 nm SiO_2, and 20 nm TiO_2. The resulting stack exhibits a visible reflectance exceeding 95%. A thin bluish protective layer was added to avoid degradation during handling.
- **S90 substrate**: a simplified aluminum base with a single Al layer deposited by PVD. Due to natural surface oxidation, a native Al_2O_3 layer forms spontaneously, lowering the reflectance to approximately 90%. A yellowish protective coating was applied for sample preservation.

The adoption of two substrate types ensured that the effect of the upper nanoporous coatings could be decoupled from substrate reflectance. In particular, the V95 surface maximizes the reflective baseline, while the S90 represents a more realistic, industrially scalable reference.

3.1.2 Paint (Polymer Matrix) and Additives

The base coating was a commercial water-based acrylic binder (ThermoShield Exterior, VOC ≤ 3 g L^{-1}), which already incorporates a set of standard pigments and fillers such as TiO_2, ZnO, kaolin, $CaCO_3$, and silicates. While the commercial formulation exhibits relatively high whiteness, its optical response is insufficient to achieve strong sub-ambient cooling under direct sunlight. For this reason, targeted additives were introduced:

- **Hollow glass microspheres (3M IM30K and IM16K)**: with average diameters of ~20 μm, these lightweight particles contain air-filled cavities and act as efficient Mie scatterers. Their addition reduces density while enhancing broadband diffuse reflectance, especially in the near-infrared range where many paints otherwise suffer from absorption dips.
- **Calcium carbonate ($CaCO_3$) powders**: introduced to strengthen scattering in both visible and near-infrared bands. Due to their relatively high refractive index, they contribute to broadband reflectance enhancement.

- **PVDF-HFP powders**: deliberately added in order to tailor the infrared spectral response. This fluoropolymer selectively improves emissivity in the 8–13 μm atmospheric transparency window, thus increasing net radiative cooling power. The use of dry powders avoided the need for harmful organic solvents such as acetone or toluene, ensuring compliance with EU environmental regulations on VOC content.

The synergy between these additives aimed to simultaneously maximize solar reflectance and thermal emittance while retaining the mechanical stability and processability of the paint matrix.

3.1.3 Sample Paint Coating

The modified paints were applied manually using a brush. While manual deposition may introduce some variability in surface uniformity, this approach allowed rapid preparation of multiple samples under comparable conditions. For each substrate type (V95 and S90), different formulations were applied, ranging from the pure acrylic base to composites with single or combined additives. In selected cases, multiple coats were applied sequentially, yielding thicker films. This step was motivated by the need to investigate the role of thickness in suppressing substrate-related absorption and enhancing diffuse scattering.

After drying, the coating thicknesses were measured using a Tesa Digital Caliper with a resolution of ±0.02 mm. Depending on the number of coats, the resulting dry thickness varied from 0.14 mm to nearly 1 mm. On the V95 substrate, thicknesses of 0.14, 0.32, 0.47, and 0.74 mm were obtained for one to four coats, respectively, while on the S90 substrate, the range extended from 0.15 to 0.96 mm [38].

3.1.4 Nanoporous Polymer Film Integration

A further structural element was introduced by laminating a nanoporous PP-PE-PP trilayer membrane (Celgard C210, pore size ~40 nm, thickness ~16 μm) on top of the coatings. The film served a dual purpose: (i) increasing solar reflectance in the UV by multiple scattering within the nanopores, and (ii) acting as a protective hydrophobic layer against dust and moisture. Two configurations were studied:

1. **Open configuration**: the film was directly rolled onto the wet paint surface, ensuring intimate contact.

2. **Enclosed configuration**: the film was suspended ~1.5 cm above the sample, functioning as a convection shield enclosing the sample slot.

This comparison was crucial, as the open case more closely mimics scalable deployment, while the enclosed case highlights convection-related artifacts that may bias cooling measurements.

3.1.5 Sample Indexing

The samples are divided into two types: the first set has been deposited on a substrate of raw Al on which a film of Al (50 nm), one of SiO2 (20 nm) and one of TiO2 (20 nm) have been deposited via PVD. The resulting substrate gets referred as V95 and it is provided as reference substrate on the second-last top rights position, covered with a protective bluish layer. The second set of samples were created by using a substrate of Al with just one coat of Al deposited via PVD. Let's notice that due to the intrinsic nature of the material there has been a natural growth of Al2O3 on the top surface. The resulting substrate gets referred as S90 and it is provided as reference substrate on top rights with a protective yellowish layer.

For the paint formulation, a commercial water-based acrylic binder (*Exterieur by ThermoShield*) with low Volatile Organic Compounds (VOCs ≤ 3 g L^{-1}), incorporating TiO_2, ZnO, kaolin, $CaCO_3$, silicates, and water [6], was employed as the base. Into this matrix, several scattering agents were manually introduced, namely $CaCO_3$, $BaSO_4$, PVDF-HFP in powder form, and IM30K and IM16K SiO_2 glass bubbles supplied by 3M. The exact weight fractions for each additive are listed in Tables 5.1 and 5.2. Through the synergistic combination of these materials, a lightweight paint mixture was obtained, characterized by strong optical performance across both the UV–Vis and NIR regions.

The SiO_2 bubbles, together with the additional scatterers, are primarily responsible for boosting the emissivity of the acrylic base, especially in the NIR domain. PVDF-HFP was deliberately added to enhance selective absorption in the LWIR, and it was used in its powder form to eliminate the need for organic solvents such as acetone or toluene. This adjustment ensured the production of a paint fully compliant with EU environmental regulations for VOCs. Application of the mixture was carried out manually using a brush on two types of

substrates, V95 and S90. For certain formulations, an additional coat was applied (e.g., 2C, 3C, 2F, 7G, 8G) to increase the final thickness.

IM30K AND IM16K SiO_2 MICROPARTICLES

These hollow glass spheres, manufactured by 3M, have an average diameter of about 20 micrometer and contain an air-filled cavity. Their inclusion reduces the material density, improves thermal stability, and lowers production costs. Both IM30K and IM16K are designed for lightweight applications, with IM30K being slightly denser, thereby enabling a greater weight reduction when necessary. IM30K spheres are particularly suited to harsher processing conditions compared to IM16K. Owing to their unique morphology, these microspheres scatter light strongly in the visible range (380–750 nm) while also maintaining significant emissivity in the infrared, making them attractive components for high-performance radiative coatings.

The indexing and properties of the samples used are shown in the table below:

Table 3.1: Description of V95 substrate samples with different base formulations and coatings.

V95 substrate samples	
B	Acrylic base
2B	Base+33% w/v glass bubbles (3M) IM30K type
3B	Base+26% w/v of $CaCO_3$ powder
4B	Base+16% w/v of PVDF-HFP
5B	Base+33% w/v glass bubbles (3M) IM30K type+26% w/v of $CaCO_3$ powder
6B	Base+33% w/v glass bubbles (3M) IM30K type+16% w/v of PVDF-HFP
2C	Base+33% w/v glass bubbles (3M) IM30K type+26% w/v of $CaCO_3$ powder+16% w/v of PVDF-HFP (two coats of paints)
3C	Base+33% w/v glass bubbles (3M) IM30K type+26% w/v of $CaCO_3$ powder+16% w/v of PVDF-HFP (three coats of paints)
1A	Commercial white paint already incorporating glass bubbles
3A	1A+20% w/v glass bubbles (3M) IM16K type
1F	Polar BEAR (commercial water-based cooling paint) one coat of paint
2F	Polar BEAR (commercial water-based cooling paint) two coat of paint
3F	Thermoshield (commercial solvent-based cooling paint) one coat of paint
4F	Thermoshield (commercial solvent-based cooling paint) one coat of paint
3M	TBD composition

Table 3.2: Description of S90 substrate samples with different base formulations and coatings.

S90 substrate samples	
1G	Acrylic base
2G	Base+33% w/v glass bubbles (3M) IM30K type
3G	Base+50% w/v glass bubbles (3M) IM30K type
4G, 4G_BIS	Base+33% w/v glass bubbles (3M) IM16K type
5G, 5G_BIS	Base+50% w/v glass bubbles (3M) IM16K type
6G	Base+25% w/v glass bubbles (3M) IM30K type+25% w/v glass bubbles (3M) IM16K type (one coat of paint)
7G	Base+50% w/v glass bubbles (3M) IM30K type (two coats of paint)
8G	Base+25% w/v glass bubbles (3M) IM30K type+25% w/v glass bubbles (3M) IM16K type (two coats of paint)

The appearance of the samples is as follows:

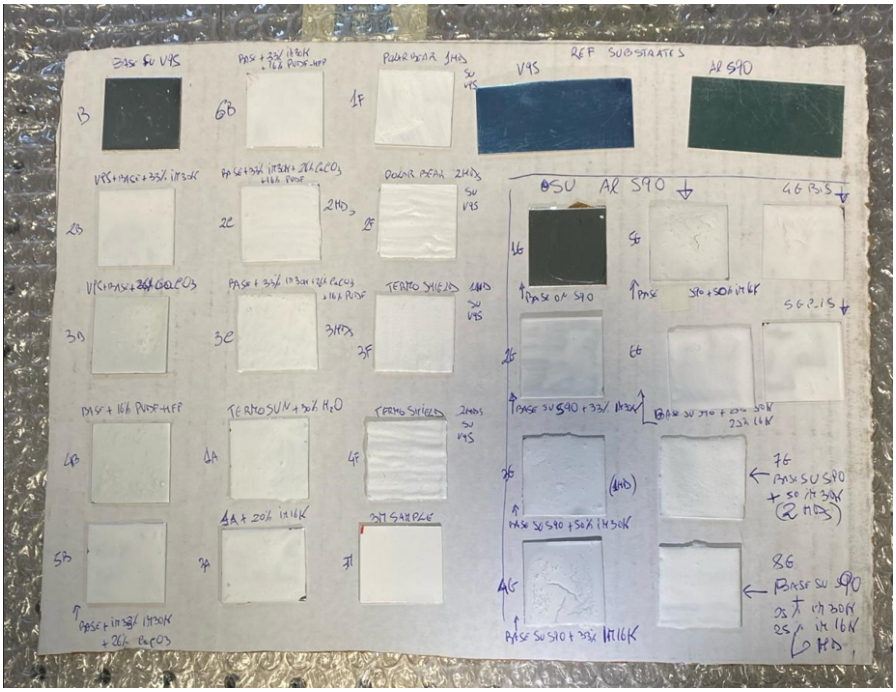

Figure 3.1: V95 and S90 samples of the nanoporous film layers for enhancing PRC performance studies.

The second measurement campaign was carried out on a new set of samples, which were specifically prepared based on the results obtained from the

first campaign. From the initial series, the specimens that exhibited better performance in the UV-Vis and NIR ranges were selected for this second stage of the experimental process. These samples were fabricated using a commercial colorless water-based acrylic paint (ThermoShield, *Exterieur*) with low VOC content ($\leq 3\,\mathrm{g\,L^{-1}}$), containing TiO_2, ZnO, kaolin, $CaCO_3$, silicates, and water; in addition, 25% IM30K SiO_2 microparticles (3M) and 25% water were included. As reported in Table 5.3, the painting procedure was repeated up to four times when required. Before drying, an NPF was incorporated into the samples. This NPF corresponds to Celgard-C210, a microporous trilayer membrane (PP-PE-PP) with a thickness of 16 μm. The thin film was applied over the wet paint using a roller, which smoothed the surface and eliminated the typical brush marks and texture.

Table 3.3: List of samples deposited on substrate V95 and S90 for increasing amount of paint coats.

V95 and S90 substrates samples with different # of coats of paint	
V95-3F	Base+Thermoshield+25% w/v glass bubbles (3M) IM30K type (one coat of paint)
V95-3F-1C	Base+Thermoshield+25% w/v glass bubbles (3M) IM30K type (one coat of paint)+Celgard
V95-3F-2C	Base+Thermoshield+25% w/v glass bubbles (3M) IM30K type (two coat of paint)+Celgard
V95-3F-3C	Base+Thermoshield+25% w/v glass bubbles (3M) IM30K type (three coat of paint)+Celgard
V95-3F-4C	Base+Thermoshield+25% w/v glass bubbles (3M) IM30K type (four coat of paint)+Celgard
S90-3F	Base+Thermoshield+25% w/v glass bubbles (3M) IM30K type (one coat of paint)
S90-3F-1C	Base+Thermoshield+25% w/v glass bubbles (3M) IM30K type (one coat of paint)+Celgard
S90-3F-2C	Base+Thermoshield+25% w/v glass bubbles (3M) IM30K type (two coat of paint)+Celgard
S90-3F-3C	Base+Thermoshield+25% w/v glass bubbles (3M) IM30K type (three coat of paint)+Celgard
S90-3F-4C	Base+Thermoshield+25% w/v glass bubbles (3M) IM30K type (four coat of paint)+Celgard

Figure 3.2: NPF called Celgard-C210.

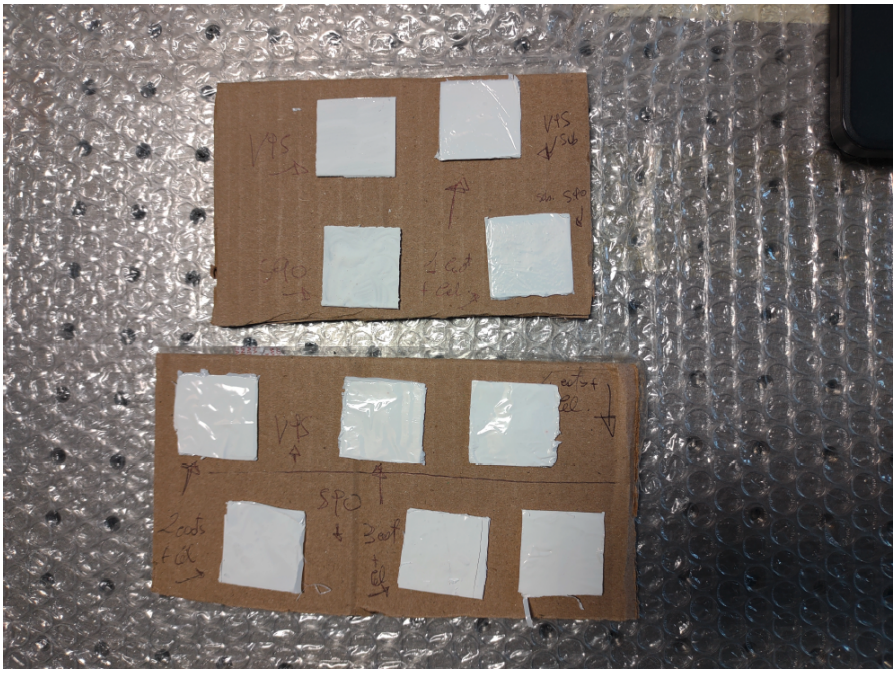

Figure 3.3: Second set of samples.

3.2 Sample Characterization

3.2.1 Optical Characterization

Following the presentation of the surface samples used in the experimental section of the study and the explanation of their detailed optical properties, the analysis, characterization, and interpretation of the results of the relevant coatings were carried out. At this point, three main types of characterization emerge: optical, surface, and thermal characterization. Optical characterization of a surface involves using light to measure and analyze the surface's physical and optical properties without damaging it. This process involves studying how light interacts with the surface by measuring changes in its intensity, phase, energy, or polarization after reflection, transmission, or absorption. Key properties determined through these non-destructive techniques include surface morphology, such as roughness and topography, and optical constants like refractive index, absorption, and reflectance. Surface characterization is the comprehensive analysis of a material's surface properties, including its chemical composition, morphology, topography, crystallography, and other physical attributes, using specialized techniques. Thermal characterization, on the other hand, studies how a material's physical and chemical properties respond to controlled heating and cooling programs. By monitoring the changes in properties like mass, volume, or heat absorption, researchers can understand how a surface will behave under different thermal conditions, which is crucial for designing materials with specific thermal resistance and energy efficiency in industries like polymer manufacturing and electronics [39]. It is clearly seen that these three types of analysis cannot be evaluated independently of each other and contain complementary elements.

3.2.2 Instruments

Cary 5000 UV–VIS–NIR Spectrophotometer

The Varian Cary 5000 spectrophotometer was employed to evaluate the optical response of the nanoporous coatings across the solar spectrum (250–2500 nm). This instrument is based on a dual-beam configuration, which enables high-precision transmittance and reflectance measurements by simultaneously comparing the signal from the sample against a reference [40]. The measurements

were performed using an integrating sphere accessory, which collects both specular and diffuse components of the reflected light, thus ensuring an accurate determination of the total hemispherical reflectance.

The operational principle of the spectrophotometer relies on the dispersion of broadband light through a monochromator, followed by the detection of intensity at specific wavelengths by a photomultiplier tube (UV–Vis region) or InGaAs detector (NIR region) [40]. By scanning over the relevant spectral range, one obtains the reflectance $R(\lambda)$ and transmittance $T(\lambda)$ spectra of the samples.

$$R_{\mathrm{SW}}(\theta, h) = \frac{\sum_{\lambda} R_h(\lambda, \theta, h)\, E_{\lambda}(\lambda)\, \Delta\lambda}{\sum_{\lambda} E_{\lambda}(\lambda)\, \Delta\lambda} \tag{3.1}$$

In the context of passive radiative cooling (PRC), the measured reflectance spectra are used to compute the solar-weighted reflectance, R_{solar}, which quantifies the fraction of incident solar radiation reflected by the surface under the AM1.5 global spectrum. This is achieved by integrating the product of the measured spectral reflectance and the solar irradiance distribution, normalized over the solar band (280–2500 nm). High R_{solar} values are essential to minimize solar absorption and enhance the net cooling power of the coating.

Furthermore, the use of the integrating sphere allows the evaluation of the diffuse scattering contribution, which is critical in nanoporous coatings where multiple scattering enhances broadband solar rejection. These measurements therefore provide the experimental basis for linking the microstructural design of coatings to their macroscopic optical performance.

To evaluate the hemispherical reflectance of the samples (comprising both specular and diffuse components), a DRA (Diffuse Reflectance Accessory), commonly referred to as an integrating sphere, was employed. This instrument is hollow, with its internal walls coated to act as a non-selective diffuse reflector. Thanks to this surface treatment and the sphere's geometry, most of the reflected radiation is redirected toward the detector. The system also allows measurements to be performed either with or without the specular contribution, thereby enabling the distinction between total reflectance and purely diffuse reflectance. The integrating sphere itself exhibits a reflectance of 98% across the investigated spectral range [41]. The detector is placed inside the sphere, positioned at its upper section, with the incident radiation striking at an angle of $3°20'$. For the UV-Vis spectral region, a PMT (Photo Multiplier Tube) is utilized as the detector, while in the NIR domain an InGaAs detector is adopted.

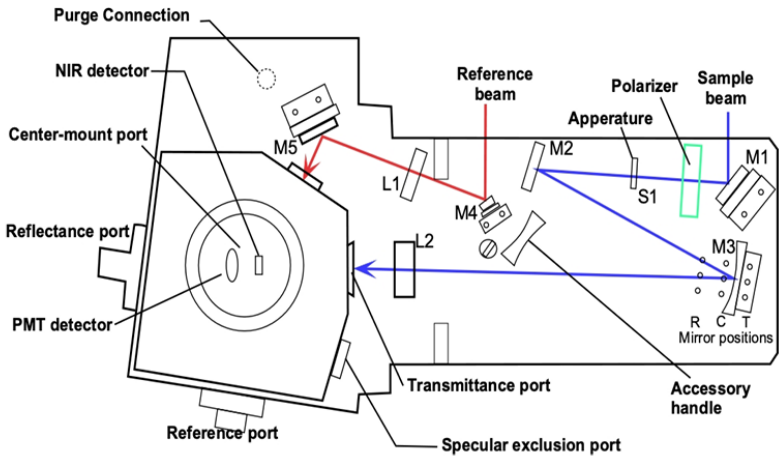

Figure 3.4: Schematic representation of the Varian Cary 5000 UV–Vis–NIR spectrophotometer equipped with an integrating sphere for total reflectance measurements.

To use this device in the laboratory and obtain the relevant results, systematic steps must be followed:

Operation Procedure

The machine has been turned on for over 90 minutes before starting with the preliminary acquisition of the baseline to guarantee stability of the internal light source components. Once the spectrophotometer was ready, the operational steps that were performed are summarized below.

1. **Scan → setup:**
   - Setting the *wavelength range* from 250 nm to 2650 nm and the *Y-mode:* %R
   - *Options* → *slit height:* reduced
   - *Baseline* → baseline correction
   - *Auto store* → storage off
2. **Scan → baseline:**
   Before taking the measurements of the samples, one has to run the 100%R baseline correction. Then after positioning the reference sample, the baseline gets collected.

3. **Scan → Start:**
   Mounting the sample and measuring the spectrum.
   For each sample more than one acquisition was taken, by rotating the sample of more or less 45° for each measurement in order to check the uniformity of the surface. All the reflectance curves taken were saved and finally post-processed with MATLAB.

From the .csv file obtained for each sample, the columns with the reflectance acquisitions get extracted, as well as the wavelength range vector. To ensure statistical reliability and reduce the noise of the acquisitions, the different reflectance curves related to the same sample have been averaged. Then after having removed the reflectance of the reference sample, the absolute reflectance of each of the sample is obtained. Moreover, a further correction has been applied to the reflectance curve: when the machine arrives at 800 nm, the optics changes causing possibly spurious artifacts in the curve.

Hereinafter, after the presentation of each of the samples, the original spectra are depicted in the first graph, one spectrum for each of the rotations, and, in the graph below, their average is shown. The other two plots on the right highlight the visible (380 nm to 750 nm) part of the spectra.

Afterwards, the solar-weighted hemispherical reflectance was calculated by normalizing the absolute reflectivity of each of the samples for the solar spectrum ASTM G173. Let's define $\rho_h(\lambda, \theta, h)$ the average hemispherical reflectance spectrum measured for each of the samples and $E_\lambda(\lambda)$ the solar irradiance spectrum for $\Delta\lambda$ the wavelength intervals, then the solar-weighted hemispherical reflectance was calculated between 280 nm and 2650 nm as

$$\rho_{SS}(\lambda) = \frac{\rho_h(\lambda, \theta, h) \cdot E_\lambda(\lambda) \cdot \Delta\lambda}{\sum_{\lambda=280}^{2650} E_\lambda(\lambda) \cdot \Delta\lambda} \tag{3.2}$$

Where $\theta = 90°$ is the incidence angle and the wavelength interval used for the solar spectrum integration is $\Delta\lambda = 1\ nm$, therefore an interpolation of the provided ASTM G173 standard has been made in order not to discard any of the data that was collected. Besides, the average of the solar-weighted hemispherical reflectance has been calculated as follow, since it can be used for measuring the optical performance of the samples,

$$\rho([SW, Vis], \theta, h) = \frac{\sum_\lambda \rho_h(\lambda, \theta, h) \cdot E_\lambda(\lambda) \cdot \Delta\lambda}{\sum_\lambda E_\lambda(\lambda) \cdot \Delta\lambda} \tag{3.3}$$

Such value has been calculated both for the entire solar spectrum (SW) and for the visible part of the spectrum (Vis).

Furthermore, as an alternative analysis, the ASTM G173 spectrum has been normalized by its maximum, hence in the following pages both normalizations will be reported, as well as the average of the solar-weighted Hemispherical reflectance and the visible part of the solar-weighted hemispherical reflectance calculated.

Where SW stays for the solar-weighted hemispherical reflectance and Vis stays for the solar-weighted hemispherical reflectance calculated for the visible part of the spectrum.

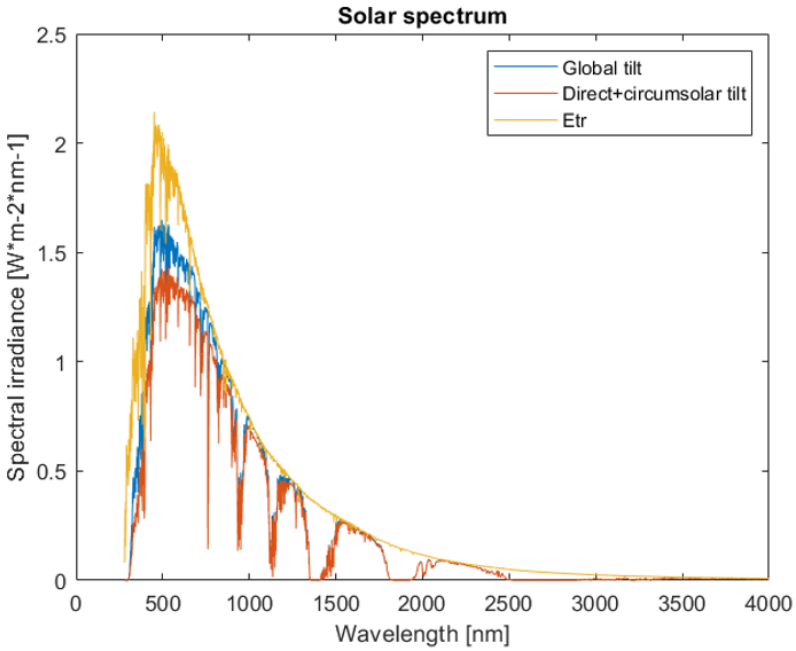

Figure 3.5: ASTM G173 reference spectra. The yellow line is the extraterrestrial solar irradiance, the blue and orange lines are the irradiances of the sun on ground level.

The reflectance spectra acquired with the Cary 5000 allowed the calculation of the solar-weighted reflectance R_{solar} for each sample. On V95 substrates, coatings containing hollow glass bubbles consistently exceeded 94% reflectance across the solar band, placing them among the highest-performing scalable PRC paints reported in our study [38].

The optical analysis of PRC coatings cannot be limited to the solar spectrum alone. While high reflectance in the 250–2500 nm range minimizes solar heating, effective radiative cooling further requires strong emissivity in the long-wave in-

frared (LWIR) region, specifically within the atmospheric transparency window from 8 to 13 μm. To verify that the fabricated paint-based samples fulfill this second criterion, mid-infrared characterization was performed using Fourier-transform infrared spectroscopy (FTIR) in Attenuated Total Reflectance (ATR) configuration. This technique provides direct access to the surface absorption spectrum, from which the emissivity can be derived according to Kirchhoff's law. The following subsections present the instrumentation, measurement principle, and procedures adopted for this analysis.

Cary 630 FTIR with ATR Tool

For completing the optical characterization of the samples in the infrared region, spanning from 2.5 μm up to 15 μm (corresponding to 4000 cm^{-1} to 650 cm^{-1}), a Cary 630 FTIR spectrometer equipped with an ATR (Attenuated Total Reflection) tool was employed (Figure 3.6).

Figure 3.6: Cary 630 FTIR spectrometer with ATR module.

Fourier-transform infrared spectroscopy (FTIR) derives its name from the Fourier transform process required to convert the interferogram into a final spectrum. The interferometer generates an interferogram by varying the optical path difference between two beams; the collected data is then mathematically transformed into an absorption spectrum, which provides the sample's spectral characteristics in the mid-infrared region.

In the ATR technique, total internal reflection occurs at the boundary between the ATR crystal with refractive index n_1 and the sample with refractive index n_2, under the condition that $n_1 > n_2$. At this interface, the incident radiation is completely reflected, while an evanescent field is formed that penetrates only a short distance d_p into the sample [41]. The onset of this effect is determined by the critical angle θ_c, given by:

$$\theta_c = \sin^{-1}\left(\frac{n_2}{n_1}\right), \tag{3.4}$$

where n_1 refers to the ATR crystal (diamond in this work) and n_2 to the investigated sample. The evanescent field decreases exponentially with depth z inside the medium:

$$E = E_0\, e^{-\gamma z}, \tag{3.5}$$

with γ denoting the decay constant. For samples that are weakly absorbing, the reflectivity R and transmittance T can be written as:

$$R = \left|\frac{E}{E_0}\right|^2 \approx 1, \tag{3.6}$$

$$T = e^{-\alpha d}, \tag{3.7}$$

where α is the absorption coefficient and d the effective optical path length. Under this approximation, the reflectivity is related to the absorbance A by:

$$R \approx 1 - A. \tag{3.8}$$

For the present measurements, a single-bounce diamond ATR crystal with refractive index $n_1 = 2.4$ at 1000 cm^{-1} was employed. The sampling area was 1 mm in diameter, and the effective penetration depth at 1700 cm^{-1} was approximately 2 μm [41].

Operation Procedure

The ATR module was operated through the *Agilent MicroLab PC* software, with the acquisition mode configured to "ATR absorbance." Prior to each measurement, a background spectrum was acquired using a gold (Au) reference, chosen due to its stable and well-characterized infrared response. The ATR crystal was thoroughly cleaned with acetone and a soft, lint-free tissue to ensure reproducible sample–crystal contact.

Each sample was then pressed against the diamond crystal by means of a clamping system designed to provide consistent pressure, reducing the likelihood of air gaps that could alter the reflection conditions. For every specimen,

three independent spectra were collected, with the sample rotated by 45° between successive measurements in order to mitigate the effects of surface non-uniformities. The recorded spectra were saved in `.asp` format and subsequently processed in MATLAB. During this step, the absorbance curves were averaged to minimize noise and enhance statistical robustness.

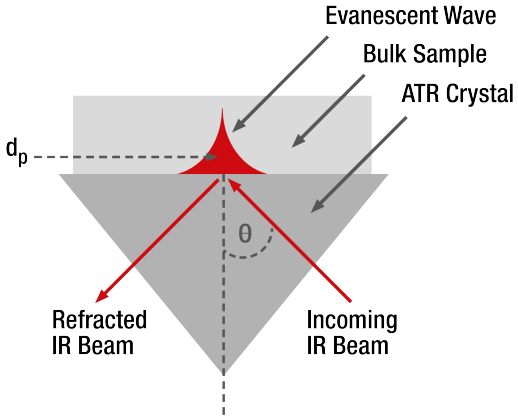

Figure 3.7: ATR principle: formation of an evanescent wave at the interface between crystal and sample. d_p marks the depth at which the electric field decreases to $1/e$ of its initial value.

Furthermore, according to *Kirchhoff's law* which states that, at thermal equilibrium, the emissivity ϵ of a material equals its absorptance at each wavelength, the emissivity of the investigated samples can be determined across the IR FTIR-ATR spectral range (2.5 μm to nearly 15 μm). Of particular interest is the LWIR atmospheric window (8–13 μm). The average emissivity over a given spectral region can be calculated as:

$$\bar{\epsilon}_{bb,[IR,LWIR]} = \frac{\sum_\lambda I_{bb}(\lambda, T) \cdot \epsilon(\lambda, T) \cdot \Delta\lambda}{\sum_\lambda I_{bb}(\lambda, T) \cdot \Delta\lambda} \tag{3.9}$$

where $I_{bb}(\lambda, T)$ is the spectral intensity of a black body at temperature T, $\epsilon(\lambda, T)$ is the spectral emissivity of the sample, and $\Delta\lambda$ denotes the wavelength interval. In this analysis, the sample temperature is assumed equal to the ambient temperature ($T = 300$ K, corresponding to 25°C). Since the wavelength resolution for the integration of the solar spectrum was set to $\Delta\lambda = 1$ nm, interpolation of the acquired spectra was performed to maintain consistency in the calculation.

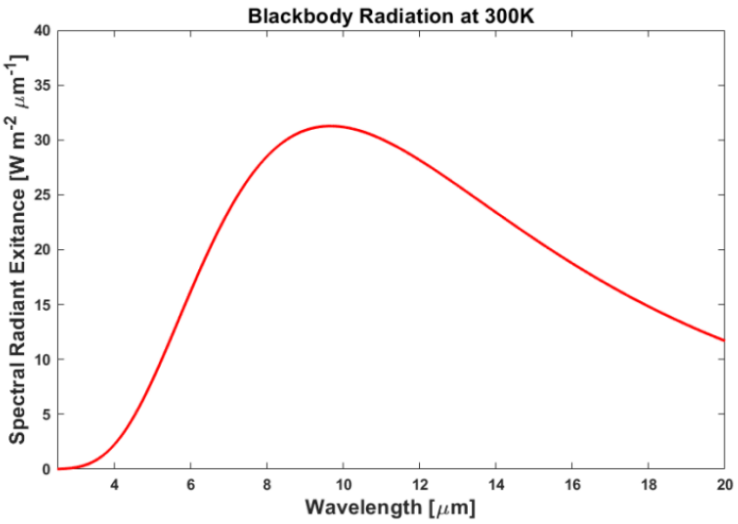

Figure 3.8: Spectral radiant exitance of an ideal black body at room temperature ($T = 300$ K, 25°C), expressed in [$W\ m^{-2}\ nm^{-1}$].

With respect to the spectrophotometer, the operational protocol followed the same procedure as described in the 3.2.2 process flow.

3.2.3 Surface and Morphological Characterization

Optical Microscopy (Zeiss AXIO Lab A1)

Optical microscopy represents one of the most established techniques in the morphological characterization of materials, offering direct visualization of the surface with minimal preparation requirements. Its application spans from biological sciences to materials engineering, where it is widely used for evaluating homogeneity, grain boundaries, micro-cracks, porosity, and defect density in coatings and thin films [42, 43]. In the context of passive radiative cooling (PRC) coatings, optical microscopy serves as a preliminary but essential tool to assess surface uniformity, the presence of scattering centers, and defects that may critically influence the optical performance of the sample [6].

The surface morphology of the samples was examined using a *Zeiss AXIO Lab A1* optical microscope. Two magnifications were used, 50x and 100x, corresponding to numerical apertures (NA) of 0.75 and 0.8, respectively. The microscope is equipped with an adjustable LED illumination system, which ensures uniform and stable lighting over the sample area, enabling the acquisition of high-quality images.

Figure 3.9: Zeiss AXIO Lab A1 Optical microscope.

Operation Procedure

Once the dedicated software *AXIO Vision* was launched, each sample was individually placed on the mounting plate. Using the X–Y mechanical stage, with a travel range of 75 mm × 30 mm, the sample was brought into focus and the most suitable region of interest was selected by adjusting its position. For every specimen, a total of eight images were collected (four at each magnification), with the corresponding focal depths documented [41].

The instrument allowed the observation of the surfaces at different focus depths, highlighting the various features of the samples. By inspecting multiple focus depths, additional information about surface roughness and defects could be extracted, thus providing a first qualitative characterization of the investigated surfaces.

Atomic Force Microscopy (AFM NX-10)

AFM NX10 uses a micro-machined cantilever with a sharp tip to measure a sample's surface [44, 41]. The operating principle of this metrology instrument is based on the balance of attractive and repulsive interactions between the cantilever tip and the sample surface. When the tip is positioned in air, a laser beam is directed onto the center of the quadrant photodetector (Figure 3.11).

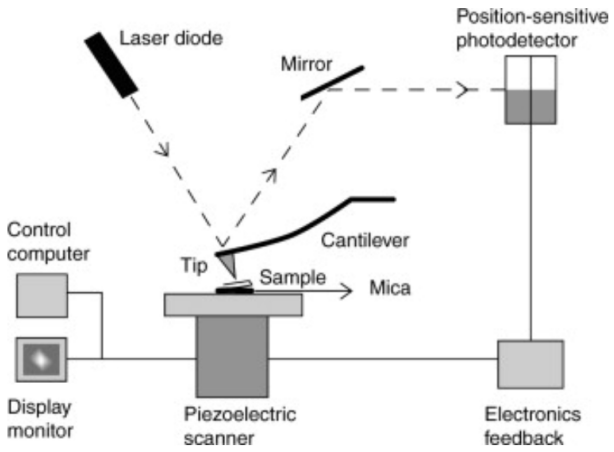

Figure 3.10: Diagram of basic functioning of AFM NX10 scanning [44].

When the tip encounters a surface feature, it undergoes a deflection that causes the laser spot to shift across the photodetector quadrants. A tube-shaped piezoelectric scanner regulates the vertical displacement of the tip, ensuring that the laser remains aligned with the center of the detector. In this way, a constant tip–sample separation is maintained. By monitoring the motion of the scanner, the surface topography can be reconstructed with high precision.

Operation Procedure

The AFM measurements were carried out in *Non-Contact* mode, where the cantilever oscillates at a nanometric distance from the sample surface without making physical contact. In this configuration, the instrument detects weak Van der Waals interactions across a scan area of $70\,\mu\text{m} \times 70\,\mu\text{m}$. The acquired data were subsequently processed using the *Gwyddion* software package. This operational mode was specifically selected to prevent damage to delicate or porous coatings, while ensuring accurate and reproducible mapping of the surface morphology.

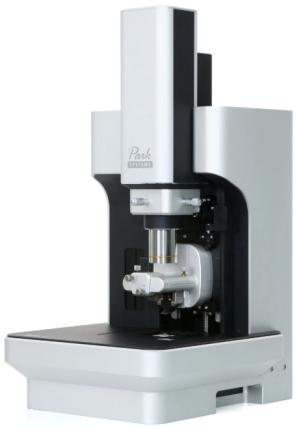

Figure 3.11: Atomic Force Microscope *Park* NX10.

Thickness Measurements (Tesa Digit-Cal)

The thickness of the investigated coatings represents a crucial parameter to correlate the morphological structure with the optical and thermal performance of the samples. In fact, for multilayer and nanoporous coatings designed for passive radiative cooling, the thickness directly affects both the reflectance in the solar spectrum and the emissive properties in the mid-infrared. Therefore, in addition to microscopic imaging and topographical scanning, precise thickness measurements were performed.

The samples selected for this measurement campaign were deposited on two different substrates, referred to as V95 and S90. Specifically, the analyzed cases included:

- The two substrates coated with a single layer of commercial ThermoShield paint (samples 3F and 4F).
- The same substrates additionally coated with IM30K glass bubbles incorporated into ThermoShield (samples V95+3F and S90+3F).
- Further variations of the V95 and S90 substrates, coated with increasing numbers of paint layers (ThermoShield and glass bubbles), as well as configurations including the Celgard porous membrane applied on top.

The measurements were carried out with a digital caliper *Tesa Digit-Cal 05.30080*, which offers a resolution of 0.01 mm and an accuracy of ±0.02 mm. This level of precision ensures that subtle differences in coating thickness, arising from

variations in paint application (single vs. multiple layers) or the addition of lightweight scatterers, can be reliably detected. The use of such a high-accuracy caliper is particularly important in order to distinguish between coatings applied with one, two, or more brush strokes, where differences are typically in the order of tens of micrometers.

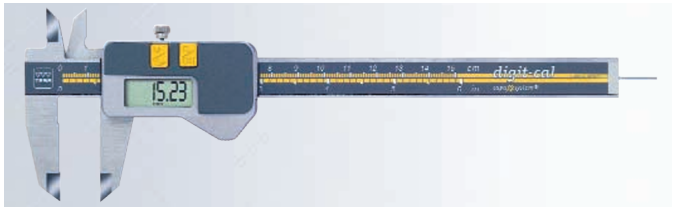

Figure 3.12: Tesa Digit-Cal 05.30080 digital caliper employed for thickness measurements.

3.2.4 Thermal Characterization and Outdoor Testing

It is important to note that under strong solar irradiation conditions, the effect of radiative cooling is partially suppressed. In particular, the sub-ambient regime was consistently observed only when the global horizontal irradiance fell below approximately 600 W/m^2. This threshold highlights the practical limits of daytime operation for PRC coatings under clear-sky summer conditions.

The outdoor measurement setup was entirely assembled by the research team at the University of Florence. The apparatus and its corresponding schematic representation are shown in Figure 3.13.

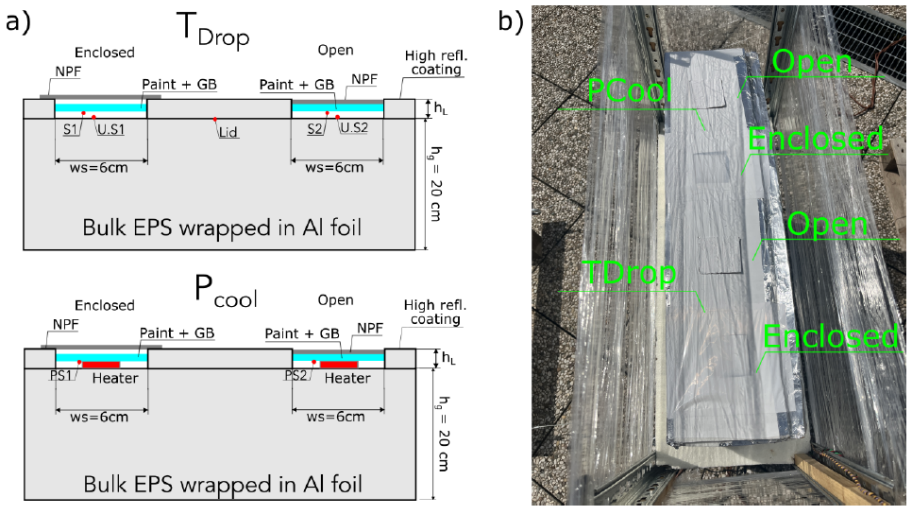

Figure 3.13: a) Outdoor experimental setup identifying the test areas and conditions. b) Schematic of a section of the sample holder. [38]

The FRESCO-board implements a low-cost, open-hardware measurement chain that simultaneously records surface and reference temperatures, solar irradiance and apparent sky temperature, and computes T_{drop} and P_{cool} for multiple samples in parallel; its design couples insulated EPS sample holders, calibrated NTC probes, an IR thermometer for sky temperature, and a PID-controlled heater to provide reproducible comparisons between emitters [45]. The measurement board adopted in this work follows the same principle of integrating thermal, radiative, and environmental channels, while being tailored to the characterization of paint-based nanoporous coatings.

The experimental setup employed a T_{drop} shield designed to measure the temperature of multiple samples using Negative Temperature Coefficient (NTC) thermistors, specifically model 103JT-025 with a nominal resistance of 10 kΩ [46]. In parallel, the ambient temperature T_{amb} and relative humidity were monitored through a DHT22 sensor [47], featuring accuracies of ± 0.5°C and $\pm 2\%$, respectively. Solar irradiance and apparent sky temperature were determined using a BH1750 light sensor [48] and an infrared sensor [49]. In addition, the P_{cool} shield incorporated further NTC probes together with a Proportional–Integral–Derivative (PID) control unit, which regulated the heating of the samples by means of a resistive element to reach the desired setpoint, typically the ambient temperature T_{amb}.

The sensors were installed inside a sample holder whose interior was lined with aluminum foil to minimize radiative heating. The holder itself was con-

structed from expanded polystyrene (EPS) with dimensions of 20 cm × 14 cm × 75 cm (height × width × length), ensuring effective thermal insulation from the surroundings. Four square samples (6 cm × 6 cm) were mounted inside the holder at equal spacing. Their position was secured by a 0.5 cm thick EPS lid, perforated with four openings that allowed exposure to ambient air, and externally covered with a highly diffusive reflective 3M tape.

To further validate the insulation performance, auxiliary NTC thermistors were embedded within the EPS block, confirming that no parasitic heating effects occurred. Two additional sensors were placed in the cavities directly below the sample slots (U.S1 and U.S2), enabling continuous monitoring of the air gaps. These measurements were essential for evaluating potential greenhouse effects arising in the partially enclosed configuration, where convective heat transfer is reduced.

The entire apparatus was further shielded with polyethylene (PE) walls to minimize external radiative heating associated with wind exposure. Finally, ambient air temperature T_{amb} was also independently monitored using one of the NTC sensors placed inside a professional PVC Stevenson Screen (Davis 7714 passive radiation shield [50]).

Figure 3.14: Picture and schematic illustration of a Stevenson screen [50].

The board allows to measure simultaneously T_{drop} and P_{cool} by using a pair of identical samples in parallel, allowing the comparison of the behaviours of the different samples employed for passive radiative cooling [38]. Moreover, for the better accuracy and regulation of the measured quantities related to temperature and solar irradiance, reference data are used. The latter are from the

weather station operated by the LaMMA consortium (Laboratorio di Monitoraggio e Modellistica Ambientale) between the National Research Council of Italy (CNR) and the Tuscany region [51].

A Stevenson screen is a standard meteorological enclosure designed to shield sensors from precipitation, direct solar radiation, and reflected or radiated heat, while still allowing free airflow. In this way, it provides a controlled environment that closely represents the actual atmospheric conditions. Such screens are typically employed to house instruments for temperature and humidity monitoring, thereby improving the accuracy and reliability of the measurements [50].

Outdoor measurements were conducted on coated samples prepared with three paint layers deposited on a V95 substrate, denoted as V95–3F–3C. Two distinct configurations were investigated: in the first case, a PP–PE–PP nanoporous membrane was placed directly on the painted surface, while in the second case, the same Celgard layer was positioned above the coating and served as a detached convection shield. For both T_{drop} and P_{cool} evaluations, two experimental setups were compared. In configuration S1, the Celgard film was mounted as an external shield over the sample slot, limiting exposure to ambient air. In configuration S2, the membrane was directly laminated onto the paint layer, thus leaving the sample fully exposed to air circulation. Temperature monitoring was performed with NTC probes positioned both beneath the substrates and in direct contact with them, whereas for P_{cool} determinations the NTC sensors and resistive heaters were mounted directly onto the sample surfaces.

The comparison between these two approaches demonstrated that integrating the PP–PE–PP film directly onto the paint coating provides the most stable and efficient cooling during daytime operation. Conversely, when the membrane was used as a suspended convection barrier, a slight improvement was observed during nighttime measurements, but this configuration led to significant overheating under solar exposure [41]. These results highlight the necessity of carefully designing outdoor experimental protocols, since semi-enclosed configurations may introduce artificial effects that alter the intrinsic thermal response of passive radiative cooling materials.

3.3 Results and Discussion

3.3.1 Sample Optical Performances

The solar-weighted hemispherical reflectance $\rho(SW, \theta, h)$ and the solar-weighted hemispherical reflectance in the visible part of the spectrum $\rho(Vis, \theta, h)$ are reported in the second and third columns. For the sake of comparison, the average of the weighted reflectance in the visible band obtained by normalizing the solar spectrum by its maximum has also been computed. One can observe that the difference between these two values is, on average, 1.315% for the coatings deposited on V95, whereas for the samples on S90 the average difference is 0.34%. As a result of these stages of measurements and optical characterizations, the measured reflectance ratios of the samples used are shown below:

Table 3.4: Reflectance values (ρ) for V95 and S90 substrate samples.

Sample	$\rho(\mathrm{SW}, \theta, h)$	$\rho(\mathrm{Vis}, \theta, h)$	**Average in the Vis**
V95	91.8073%	95.2568%	94.8873%
B	88.7263%	90.7129%	90.383%
2B	81.2266%	82.3154%	82.1768%
3B	74.6815%	77.467%	76.8289%
4B	75.4298%	77.2613%	76.586%
5B	83.9106%	84.9523%	84.7699%
6B	85.7017%	87.632%	87.164%
2C	86.021%	87.0027%	86.8677%
3C	86.1604%	87.1422%	86.8149%
1A	84.515%	86.003%	85.6131%
3A	87.2518%	88.7362%	86.3237%
1F	84.2273%	86.1202%	85.3256%
2F	85.7179%	89.894%	87.359%
3F	87.8334%	91.3546%	88.7511%
4F	88.4978%	91.8804%	89.2663%
3M	92.0928%	94.353%	91.4646%
S90	88.1817%	89.4624%	88.9081%
1G	86.3761%	85.1805%	85.0273%
2G	80.7549%	79.7749%	79.4779%
3G	85.9439%	86.3386%	85.9292%
4G, 4G_BIS	80.7446%	80.3743%	79.4933%
5G, 5G_BIS	81.369%	81.1023%	79.506%
6G	77.1146%	75.6267%	75.4116%
7G	86.9561%	87.656%	86.2597%
8G	89.5029%	90.7009%	90.2484%

Among all the samples, the ones that have an average hemispherical reflectance above 90%, apart from the bare substrates V95 and S90, are for the majority the ones deposited on V95 substrate.

The best performances in terms of both average absolute reflectance and weighted reflectance are achieved by the samples B, 2F, 3F, 4F and 3M for what concerns the V95 substrate, whereas the 8G for the S90 substrate.

The 3F and 4F samples are coated by respectively one and two coats of Ther-

moshield paint, which is a commercial solvent-based cooling paint. Whilst the 8G sample consists of a double hand of a mix of 3M paints, specifically 25% of IM30K type and 25% of IM16K type.

Optical measurement results of the second set of samples - as it is introduced in the beginning of this chapter - is shown below:

Table 3.5: Solar-weighted hemispherical reflectance $\rho(SW, \theta, h)$ and visible-band hemispherical reflectance $\rho(Vis, \theta, h)$ for V95 and S90 samples with varying Celgard coatings.

Sample	$\rho(SW, \theta, h)$	$\rho(Vis, \theta, h)$
V95	88.2238%	88.9489%
V95+1 Celgard	92.4574%	93.8463%
V95+2 Celgard	93.0595%	94.9707%
V95+3 Celgard	93.7159%	95.8515%
V95+4 Celgard	92.9239%	94.9967%
S90	88.6703%	91.3006%
S90+1 Celgard	86.2295%	87.9609%
S90+2 Celgard	90.885%	93.1715%
S90+3 Celgard	93.6029%	95.7346%
S90+4 Celgard	93.7337%	95.8318%

The plots related to each sample are reported in this order: the first row of graphs represent the measurements taken for each sample rotation, on the left for the whole spectrum and on the right focusing on the visible part of the spectrum. The second row shows the average of all the acquisitions, both on the whole spectrum and in the visible part. Finally on the last row, the first image shows the solar-weighted hemispherical reflectance, representing the amount of solar spectrum that gets reflected at each specific wavelength by the sample, whereas on the right the weighted reflectance obtained by standard normalization of the solar spectrum is shown.

The first part of the samples that performed successfully according to the specified threshold and their result scheme, sample images, and graphs according to the order mentioned above are provided below:

(a) Sample substrate

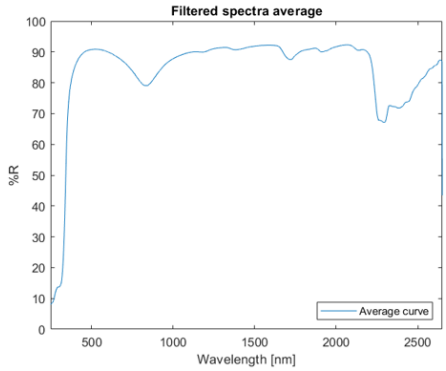

(b) Filtered spectra average

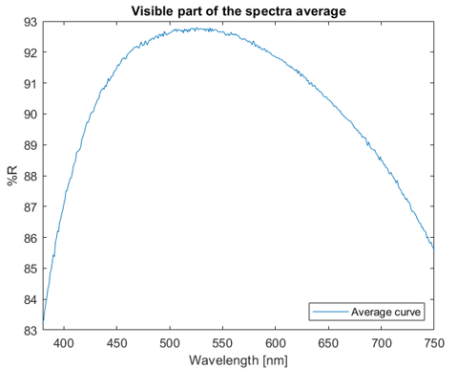

(c) Visible part of the spectra average

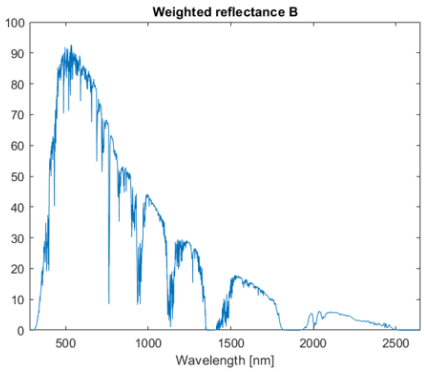

(d) Weighted reflectance of B

Figure 3.15: Reflectance measurements and corresponding spectra of the coated substrate B.

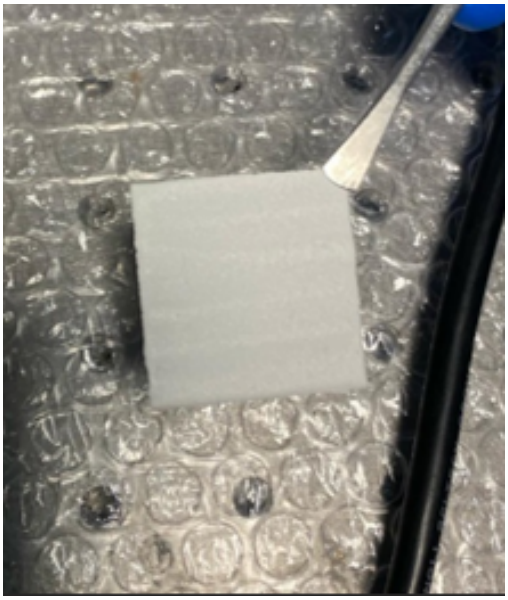

(a) Sample substrate

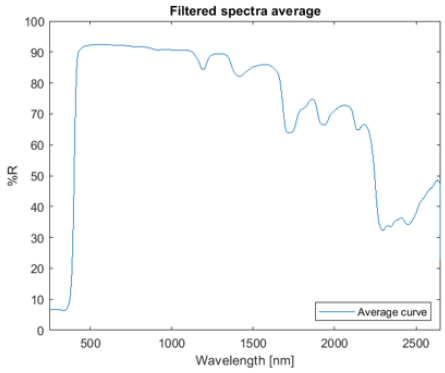

(b) Filtered spectra average

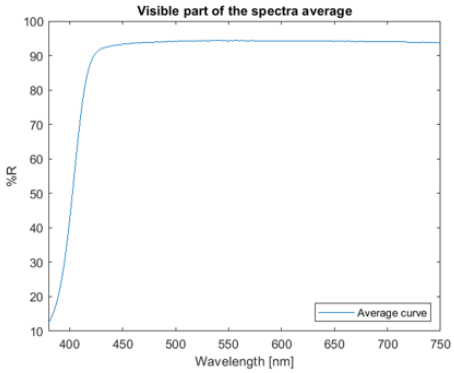

(c) Visible part of the spectra average

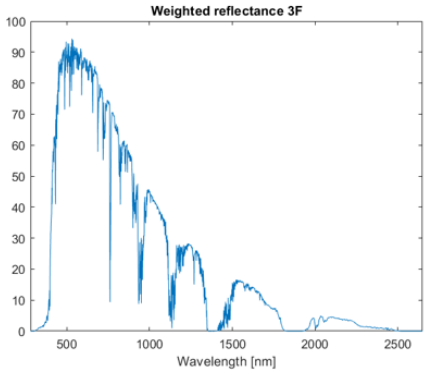

(d) Weighted reflectance of 3F

Figure 3.16: Reflectance measurements and corresponding spectra of the coated substrate 3F.

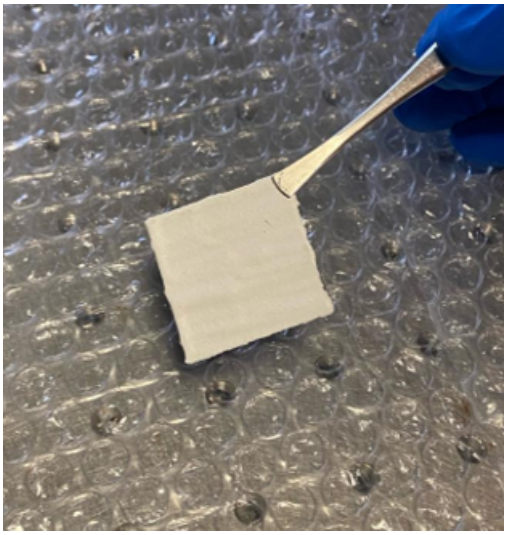

(a) Sample substrate

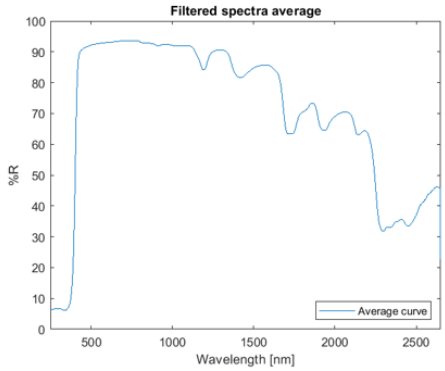

(b) Filtered spectra average

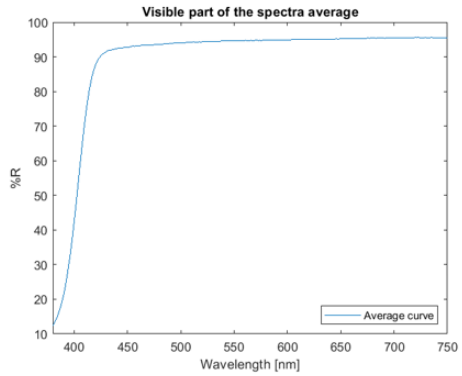

(c) Visible part of the spectra average

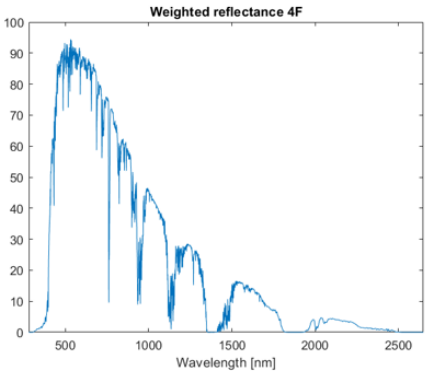

(d) Weighted reflectance of 4F

Figure 3.17: Reflectance measurements and corresponding spectra of the coated substrate 4F.

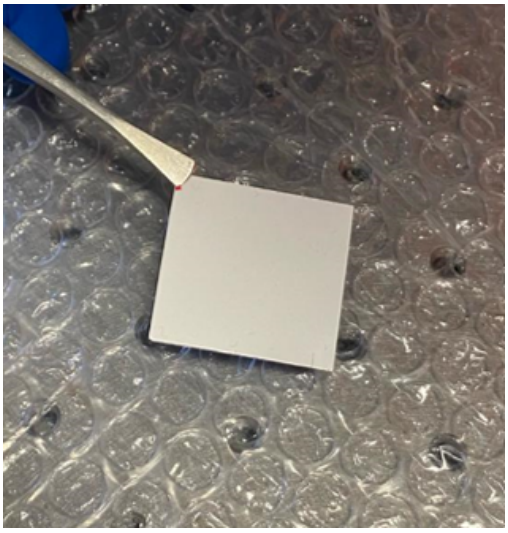

(a) Sample substrate

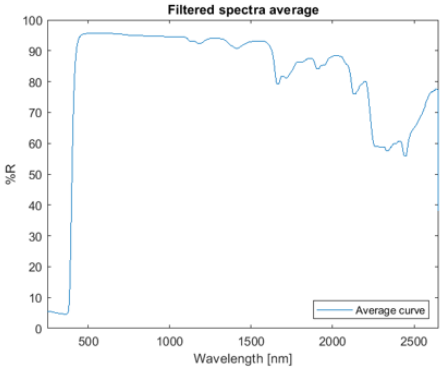

(b) Filtered spectra average

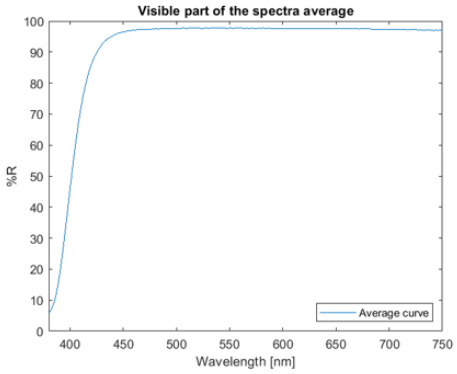

(c) Visible part of the spectra average

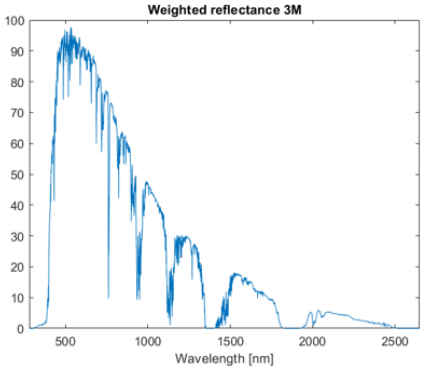

(d) Weighted reflectance of 3M

Figure 3.18: Reflectance measurements and corresponding spectra of the coated substrate 3M.

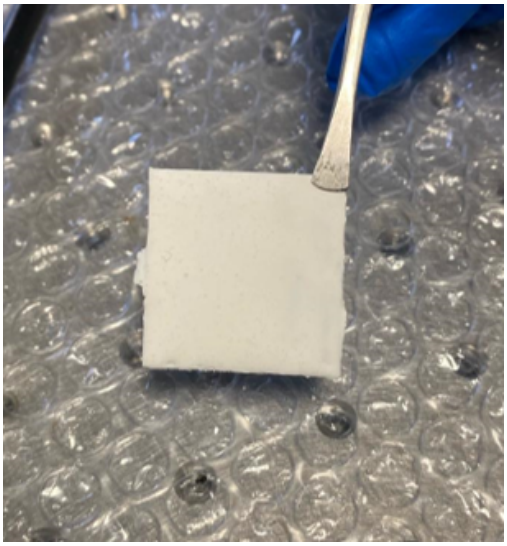

(a) Sample substrate

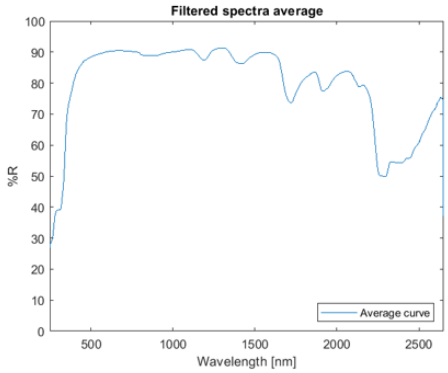

(b) Filtered spectra average

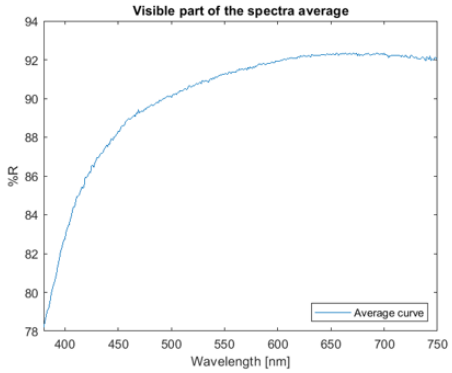

(c) Visible part of the spectra average

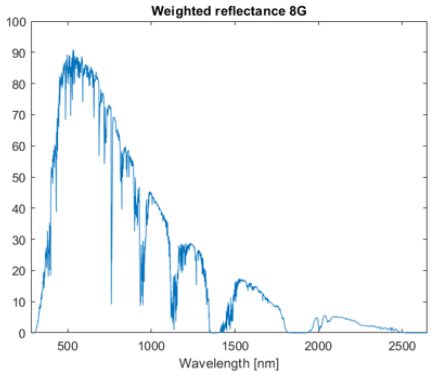

(d) Weighted reflectance of 8G

Figure 3.19: Reflectance measurements and corresponding spectra of the coated substrate 8G.

As of the first process of measuring the optical properties of the samples, the same treatment was applied to the second set of samples, and here are their results:

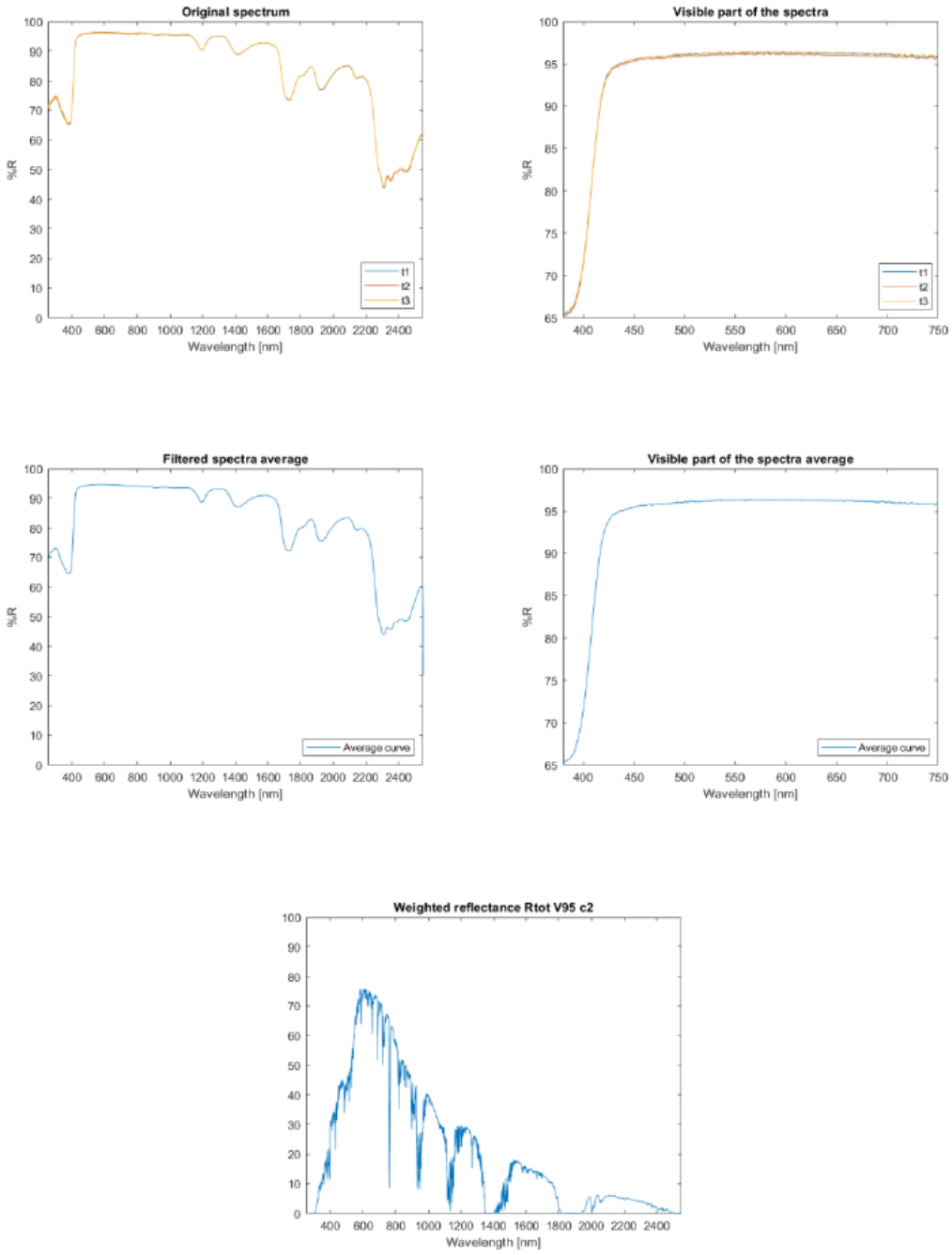

Figure 3.20: Optical characterization results for the V95 sample with no Celgard layers. The figure shows (top row) the original spectrum and visible part of the spectra, (middle row) the averaged filtered spectra and the averaged visible spectrum, and (bottom) the weighted reflectance curve.

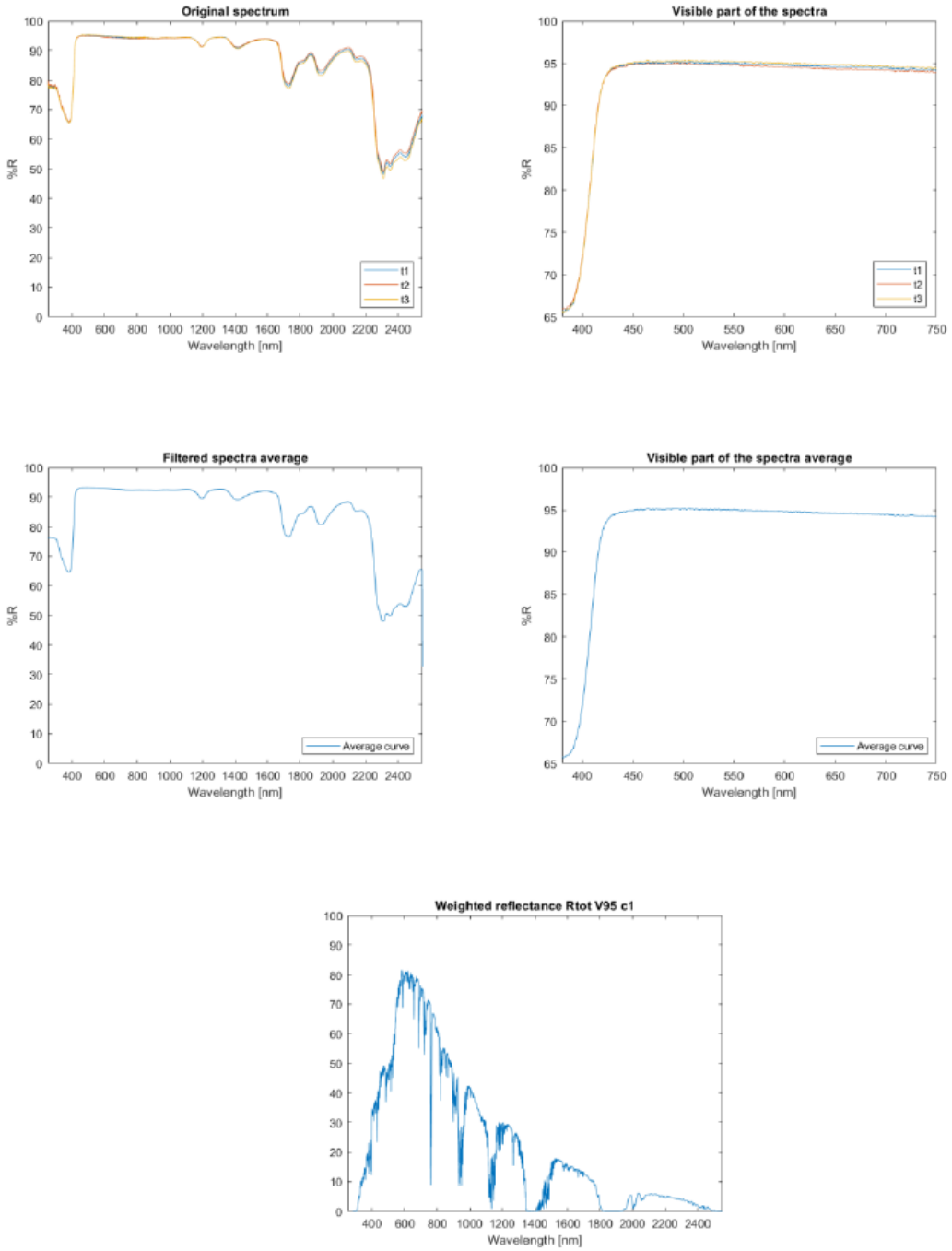

Figure 3.21: Optical characterization results for the V95 sample with 1 Celgard layers. The figure shows (top row) the original spectrum and visible part of the spectra, (middle row) the averaged filtered spectra and the averaged visible spectrum, and (bottom) the weighted reflectance curve.

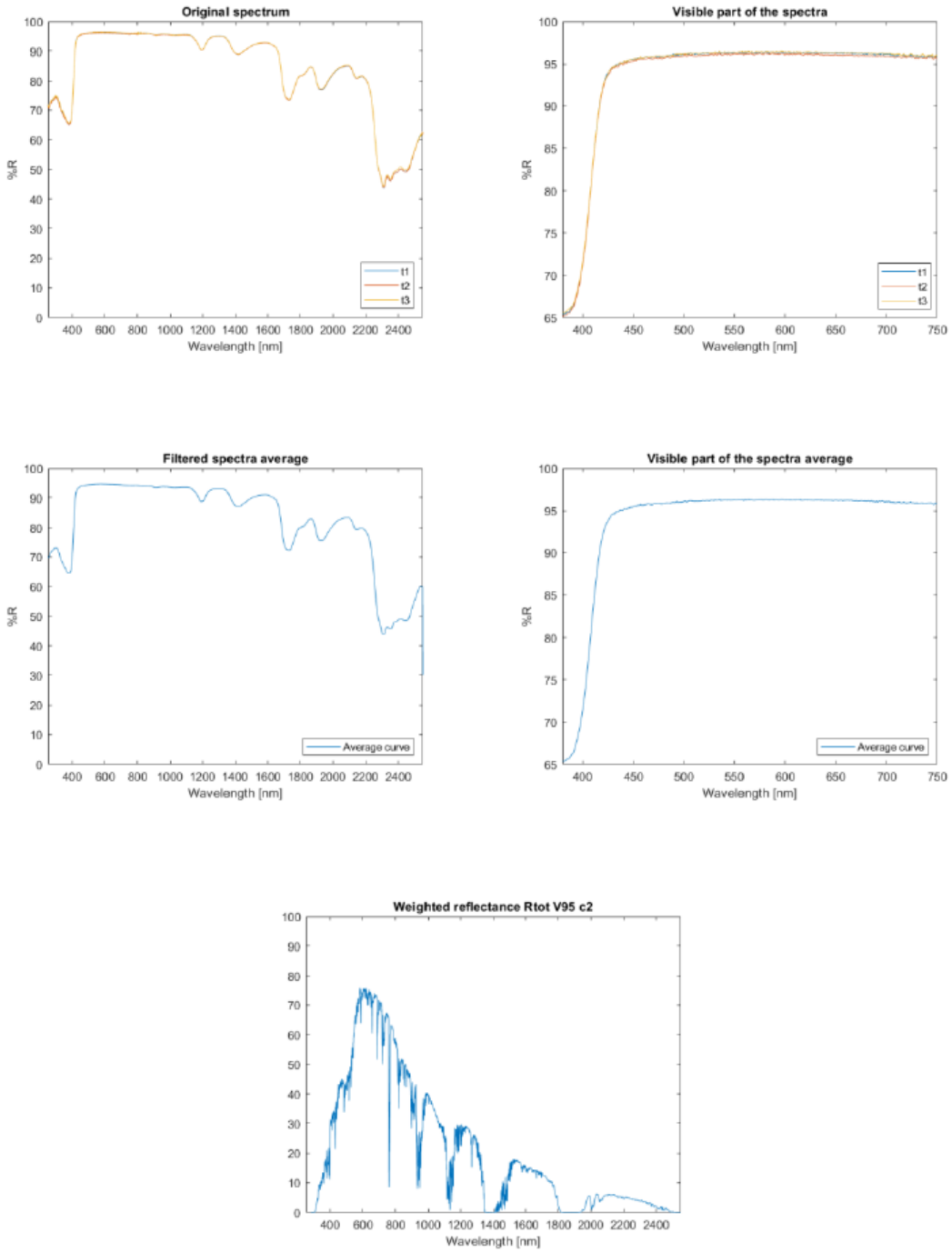

Figure 3.22: Optical characterization results for the V95 sample with 2 Celgard layers. The figure shows (top row) the original spectrum and visible part of the spectra, (middle row) the averaged filtered spectra and the averaged visible spectrum, and (bottom) the weighted reflectance curve.

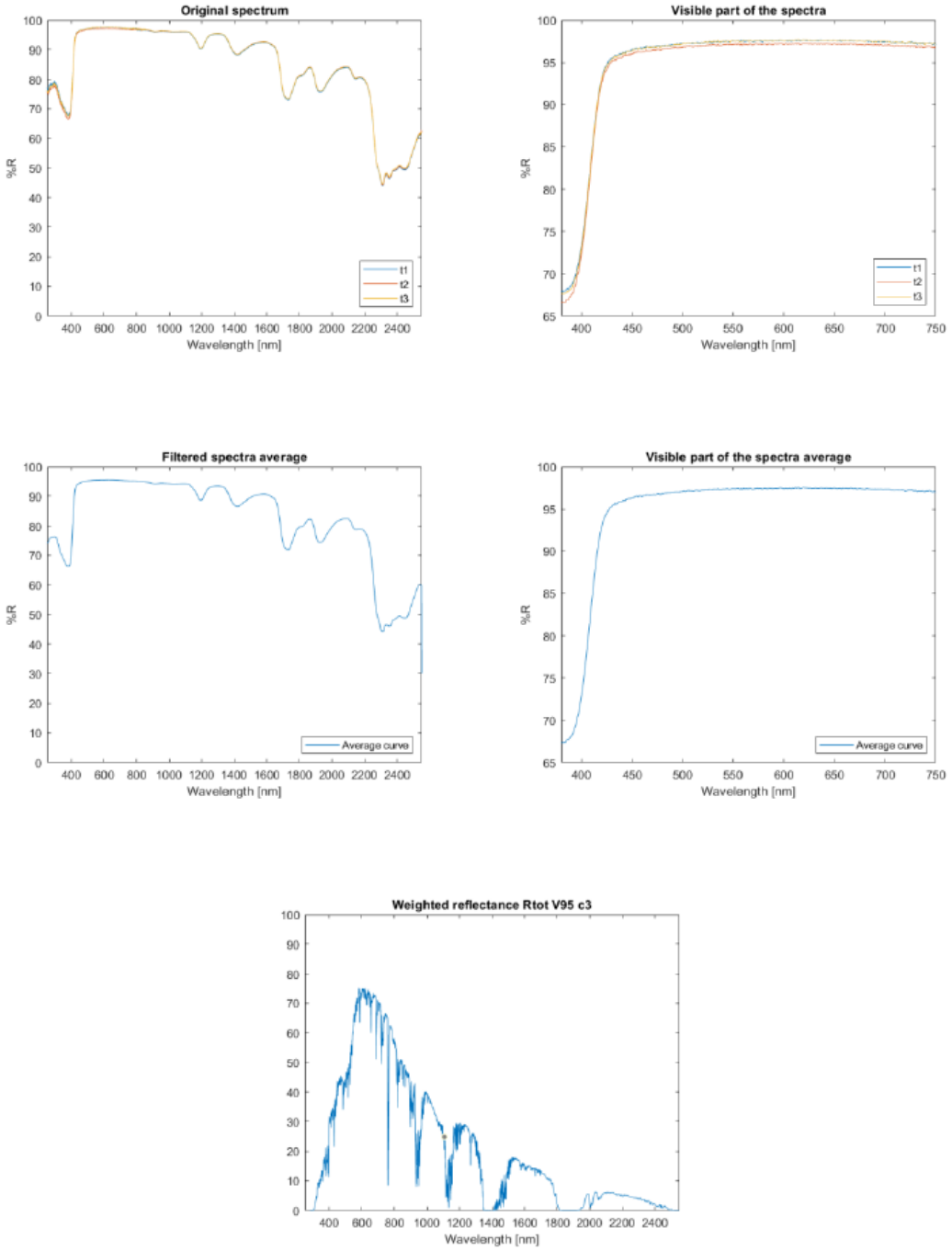

Figure 3.23: Optical characterization results for the V95 sample with 3 Celgard layers. The figure shows (top row) the original spectrum and visible part of the spectra, (middle row) the averaged filtered spectra and the averaged visible spectrum, and (bottom) the weighted reflectance curve.

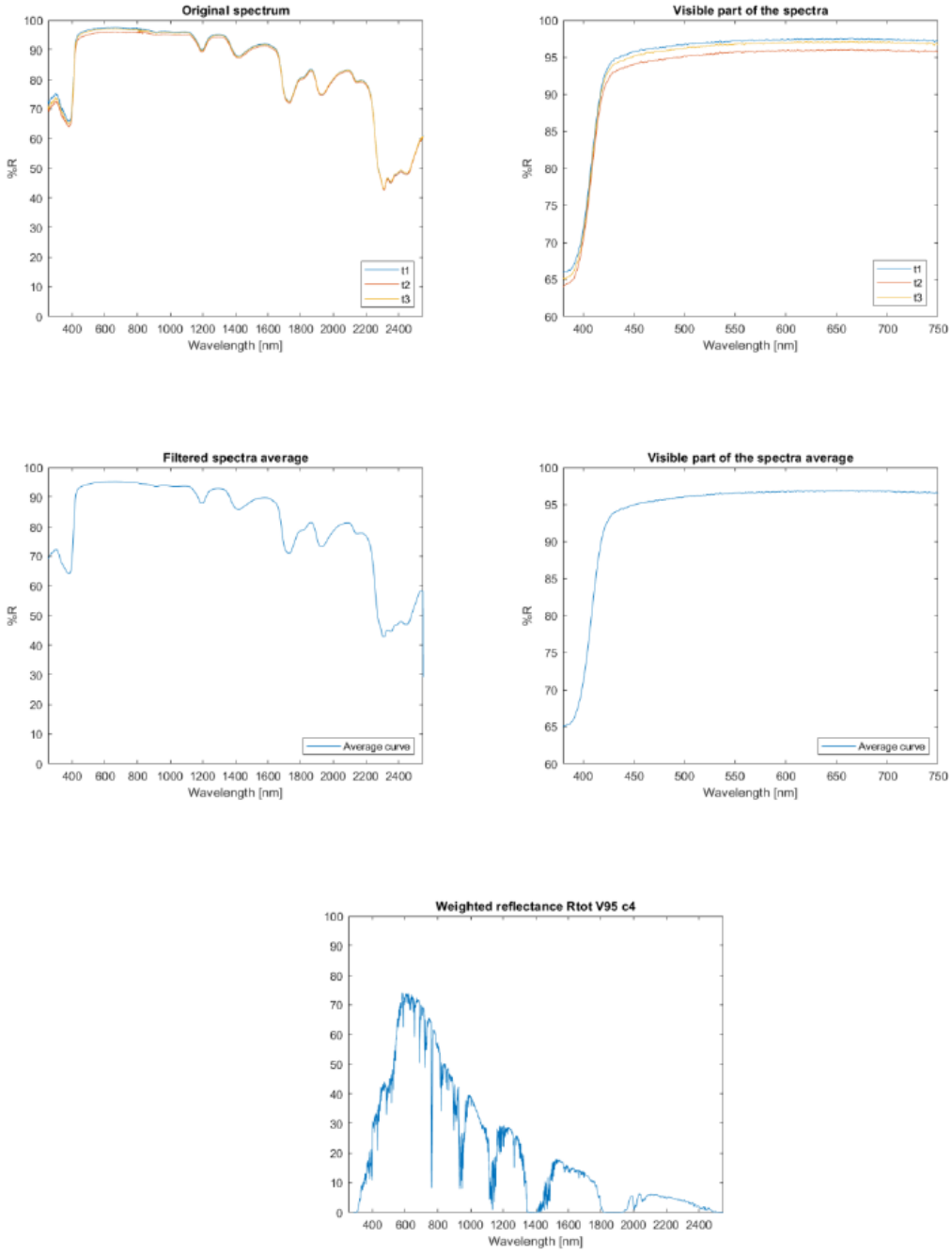

Figure 3.24: Optical characterization results for the V95 sample with 4 Celgard layers. The figure shows (top row) the original spectrum and visible part of the spectra, (middle row) the averaged filtered spectra and the averaged visible spectrum, and (bottom) the weighted reflectance curve.

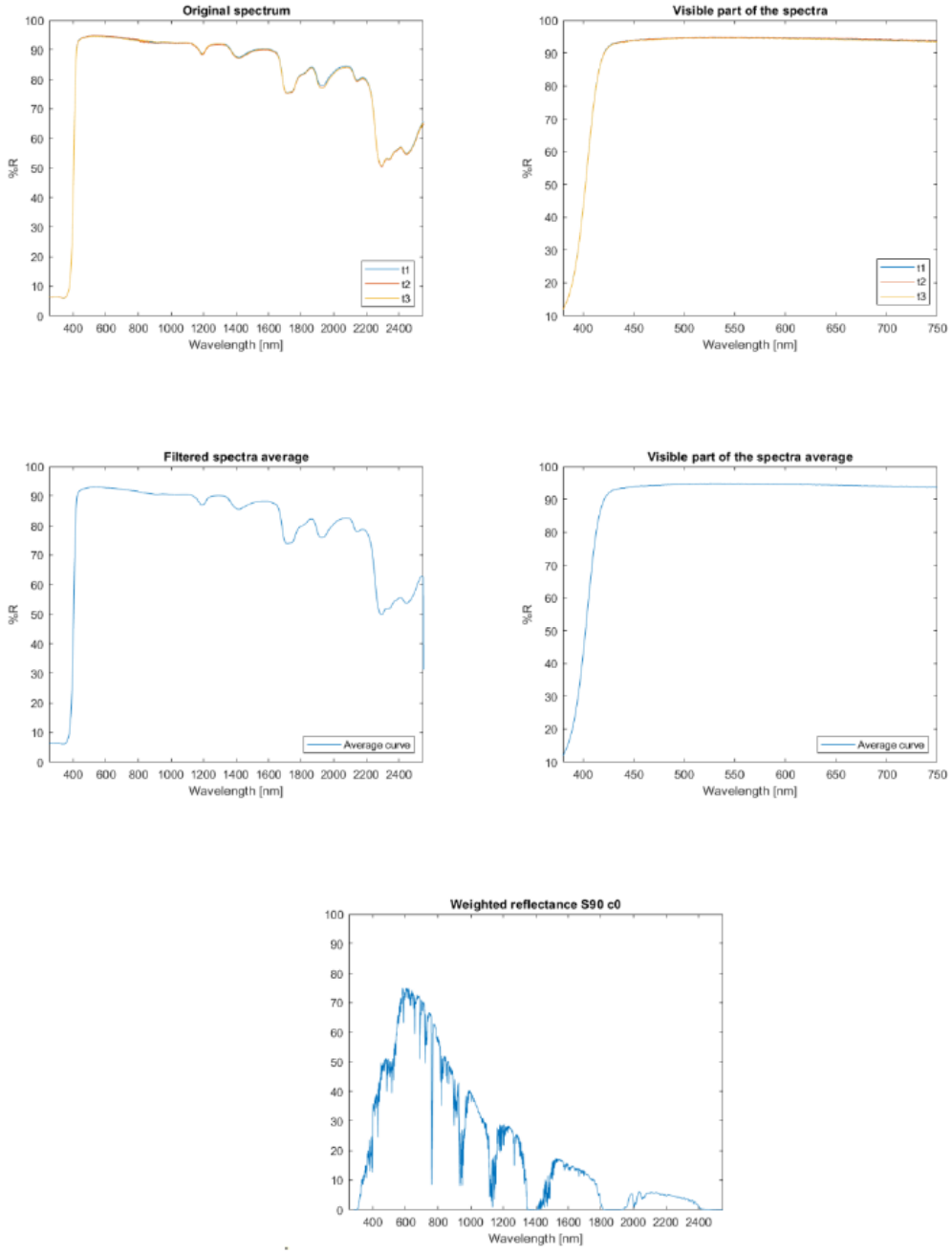

Figure 3.25: Optical characterization results for the S90 sample with no Celgard layers. The figure shows (top row) the original spectrum and visible part of the spectra, (middle row) the averaged filtered spectra and the averaged visible spectrum, and (bottom) the weighted reflectance curve.

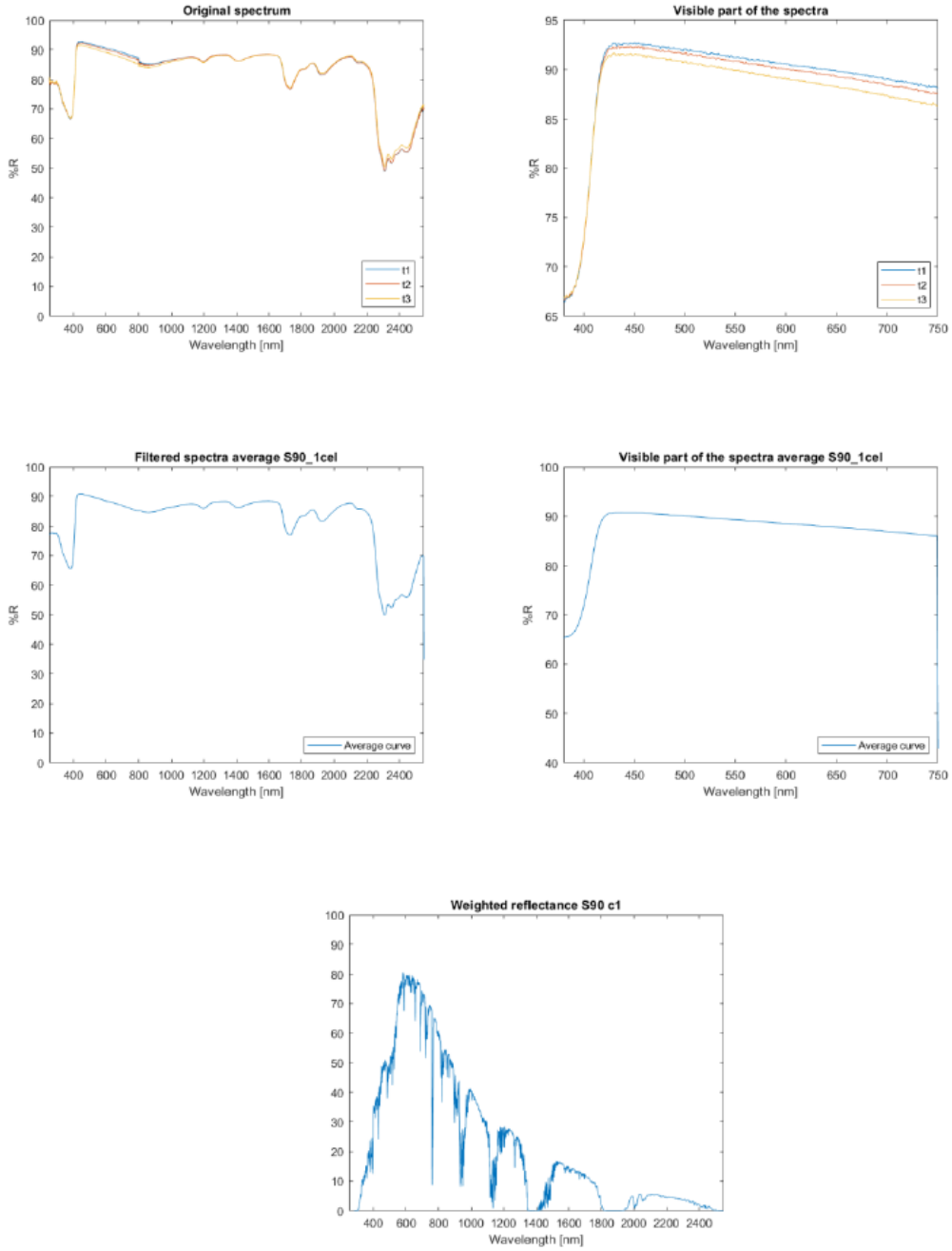

Figure 3.26: Optical characterization results for the S90 sample with 1 Celgard layers. The figure shows (top row) the original spectrum and visible part of the spectra, (middle row) the averaged filtered spectra and the averaged visible spectrum, and (bottom) the weighted reflectance curve.

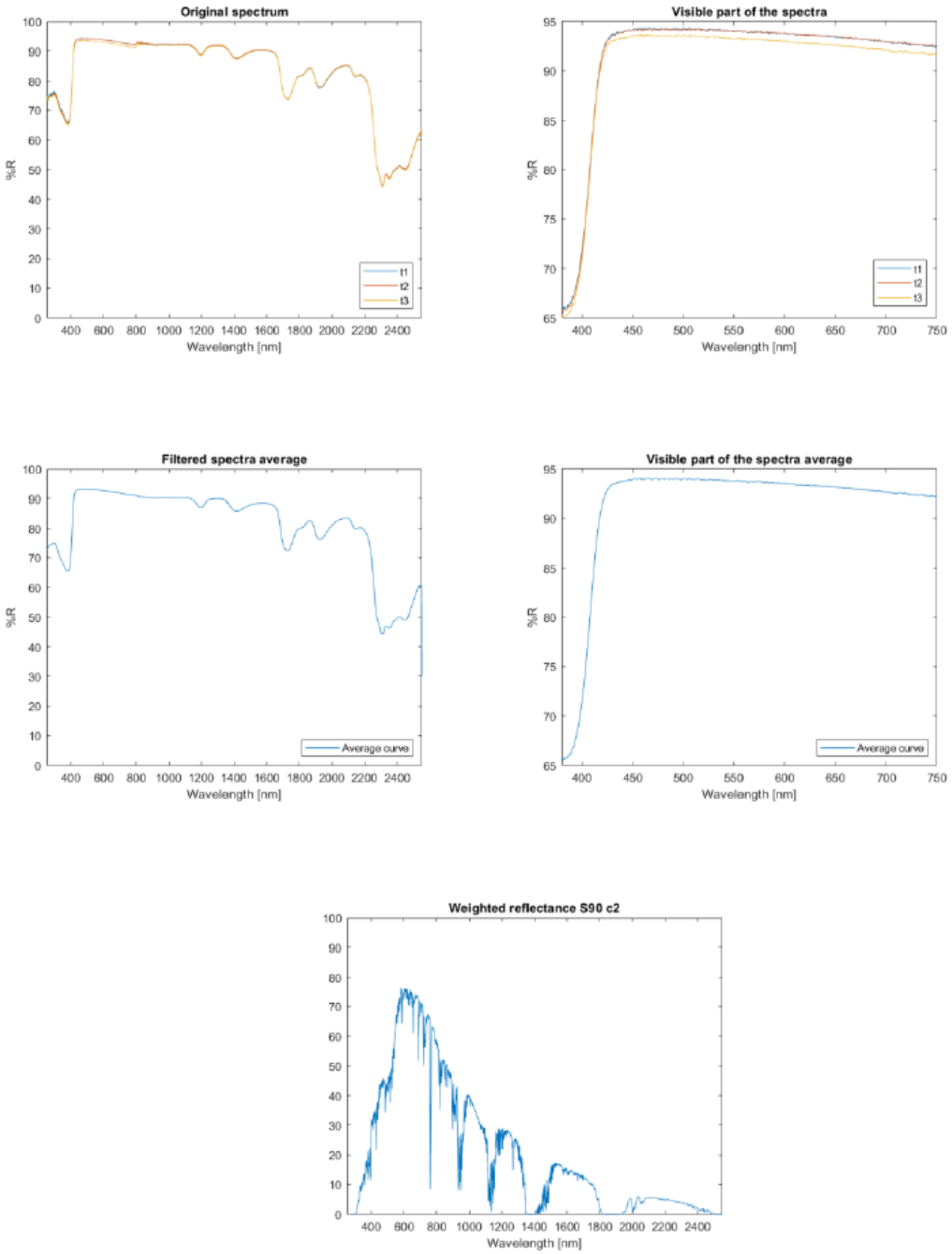

Figure 3.27: Optical characterization results for the S90 sample with 2 Celgard layers. The figure shows (top row) the original spectrum and visible part of the spectra, (middle row) the averaged filtered spectra and the averaged visible spectrum, and (bottom) the weighted reflectance curve.

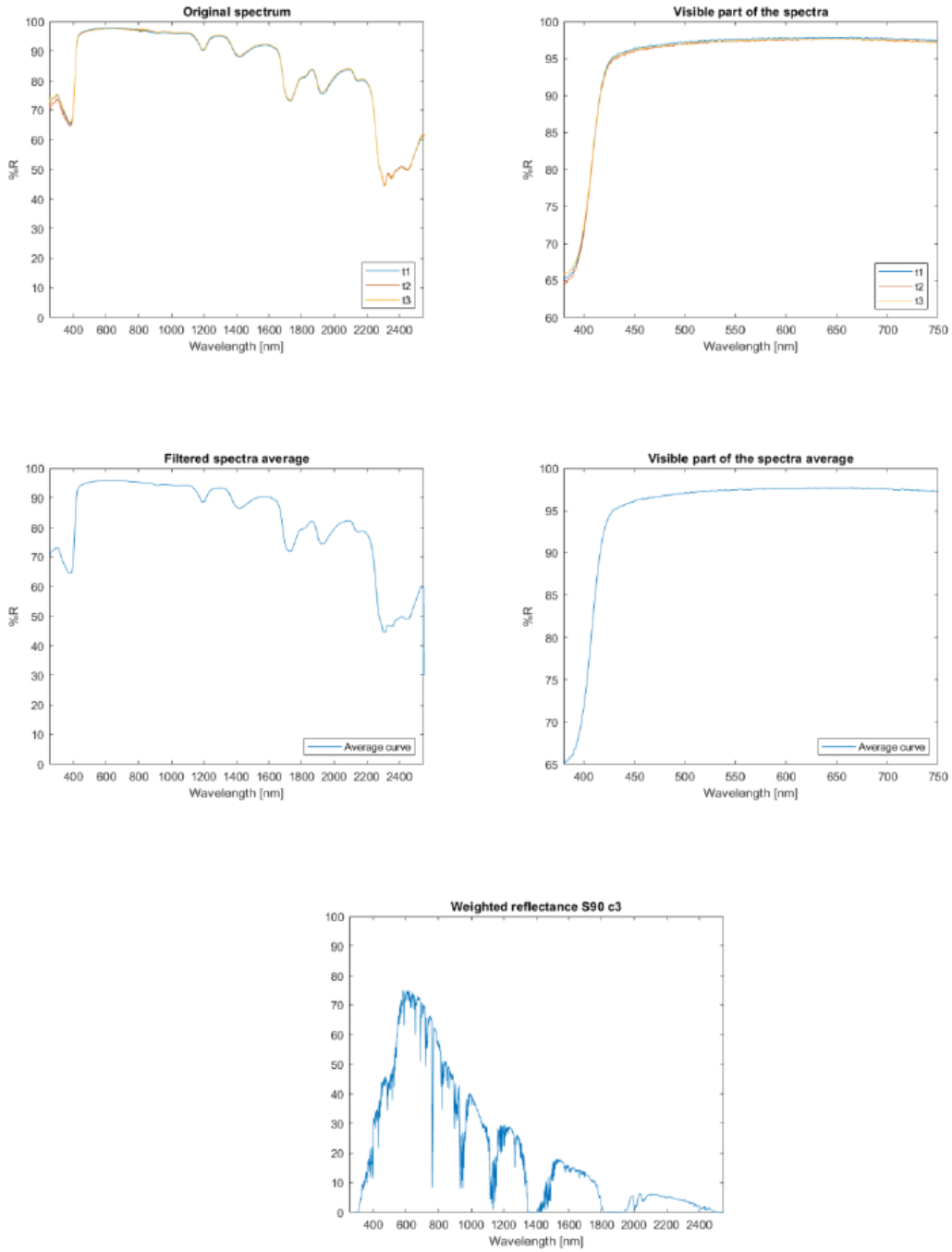

Figure 3.28: Optical characterization results for the S90 sample with 3 Celgard layers. The figure shows (top row) the original spectrum and visible part of the spectra, (middle row) the averaged filtered spectra and the averaged visible spectrum, and (bottom) the weighted reflectance curve.

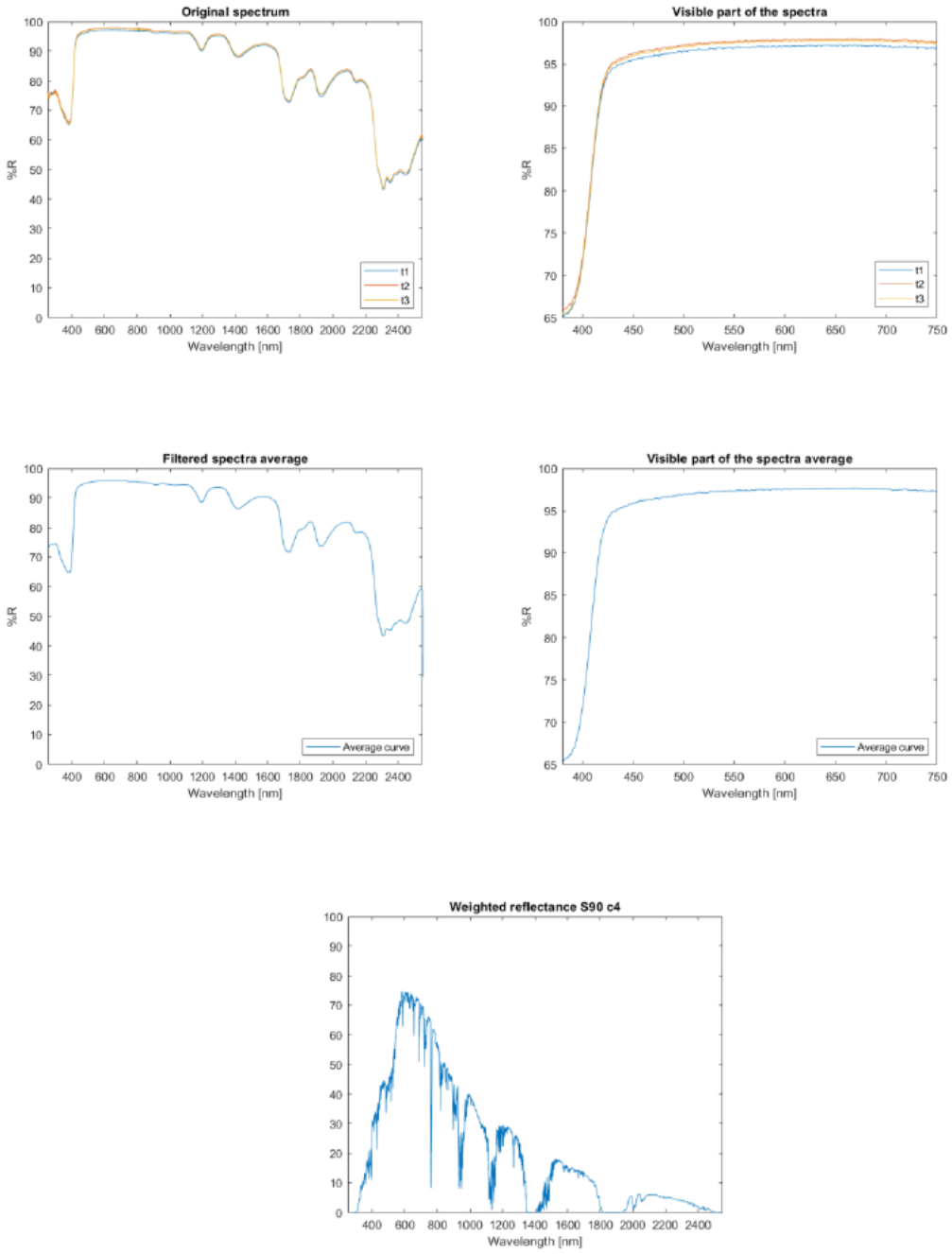

Figure 3.29: Optical characterization results for the S90 sample with 4 Celgard layers. The figure shows (top row) the original spectrum and visible part of the spectra, (middle row) the averaged filtered spectra and the averaged visible spectrum, and (bottom) the weighted reflectance curve.

MID-IR Emissivity Performance of the Samples

The emittance measurements are reported, both for the whole FTIR spectrum (first column) and also for just the atmospheric transmittance one (second

column).

Table 3.6: Emittance measurements of the samples at T=300K, reported both over the whole FTIR spectrum and restricted to the LWIR atmospheric transmittance window.

Sample	$\epsilon_{bb,IR}$ at T=300K	$\epsilon_{bb,LWIR}$ at T=300K
V95	0.1889	0.2478
V95+1 Celgard	~ 0	~ 0
V95+2 Celgard	~ 0	~ 0
V95+3 Celgard	~ 0	~ 0
V95+4 Celgard	0.0003	0.0008
S90+1 Celgard	0.0057	0.0056
S90+2 Celgard	0.0066	0.0064
S90+3 Celgard	0.0093	0.0092
S90+4 Celgard	0.0062	0.0061

The emittance measurements of the old set of samples have also been reported.

Table 3.7: Emittance measurements of the old set of samples at T=300K, reported for both the full FTIR spectrum and the LWIR window.

Sample	$\epsilon_{bb,IR}$ at T=300K	$\epsilon_{bb,LWIR}$ at T=300K
V95	0.0437	0.0616
B	0.0889	0.1249
2B	0.1182	0.1790
3B	0.1552	0.1901
4B	0.1031	0.1438
5B	0.0683	0.0980
6B	0.1059	0.1545
2C	0.0842	0.1141
3C	0.1003	0.1358
1A	0.1198	0.1409
3A	0.0496	0.0672
1F	0.2110	0.1864
2F	0.1558	0.1374
3F	0.1862	0.1715
4F	0.1776	0.1628
3M	0.1394	0.1917
S90	0.0944	0.1321
1G	0.0351	0.0515
2G	0.1070	0.1560
3G	0.1041	0.1533
4G, 4G_BIS	0.1455, 0.1652	0.2119, 0.2387
5G, 5G_BIS	0.1372, 0.1646	0.1971, 0.2379
6G	0.1455	0.2229
7G	0.0941	0.1376
8G	0.0438	0.0663
Celgard layer	0.0041	0.0042

Additionally, the emittance curves of the analyzed samples are shown below:

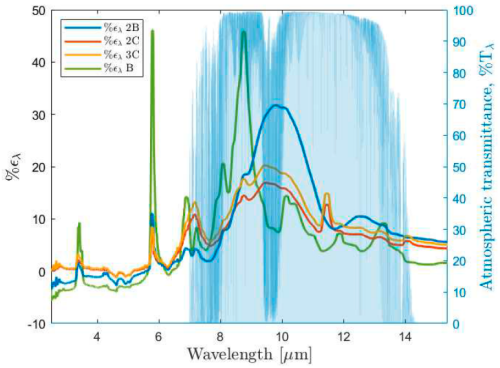

(a) Emittance curves of the samples B, 2B, 2C and 3C.

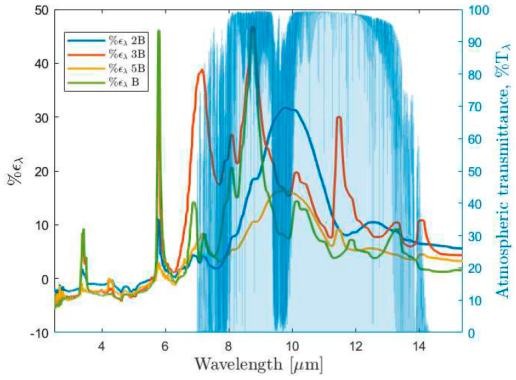

(b) Emittance curves of the samples B, 2B, 3B and 5B.

Figure 3.30: Emittance curves of the samples of the relevant sample sets [41].

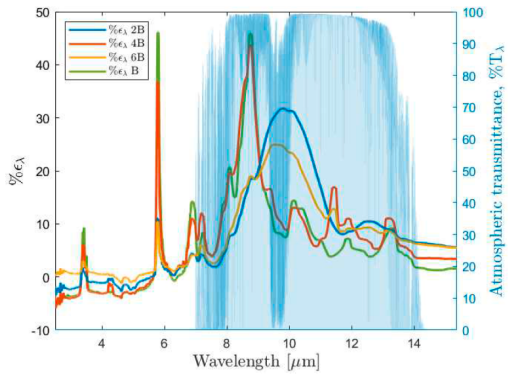

(a) Emittance curves of the samples B, 2B, 4B and 6B.

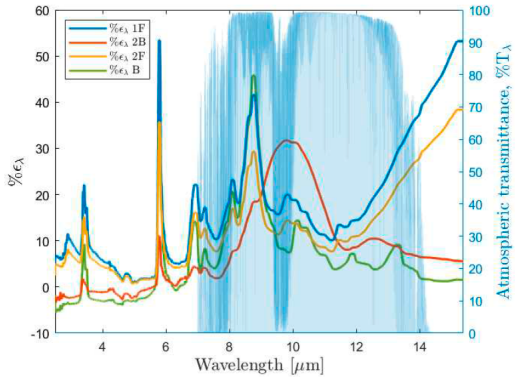

(b) Emittance curves of the samples B, 2B, 1F and 2F.

Figure 3.31: Emittance curves of the samples of the relevant sample sets [41].

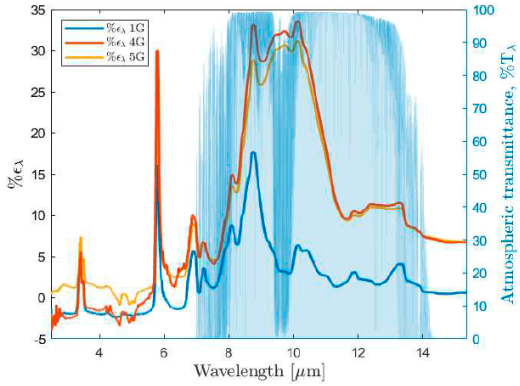

(a) Emittance curves of the samples 1G, 4G, and 5G.

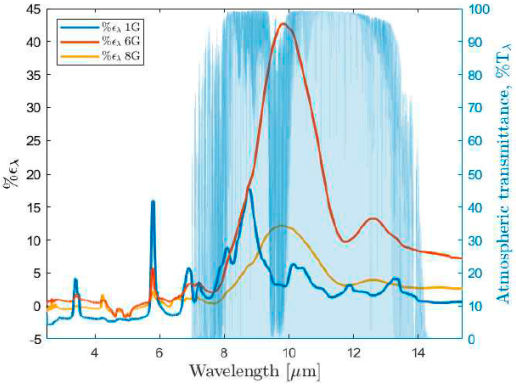

(b) Emittance curves of the samples 1G, 6G, and 8G.

Figure 3.34: Emittance curves of the samples of the relevant sample sets [41].

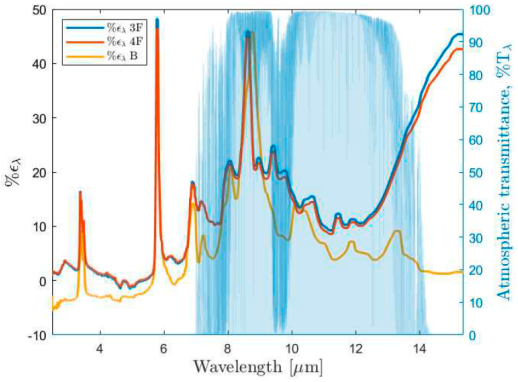

(a) Emittance curves of the samples B, 3B, and 4F.

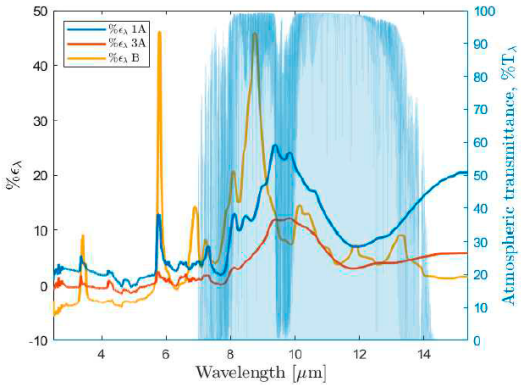

(b) Emittance curves of the samples B, 1A, and 3A.

Figure 3.32: Emittance curves of the samples of the relevant sample sets [41].

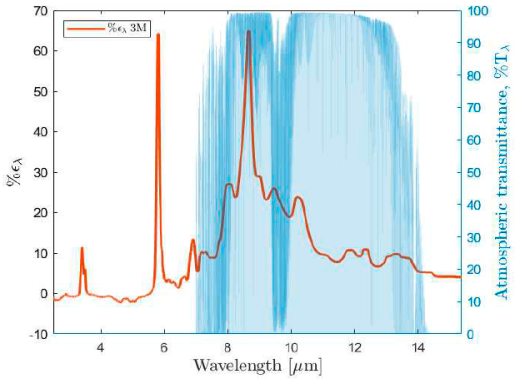

(a) Emittance curves of the sample 3M.

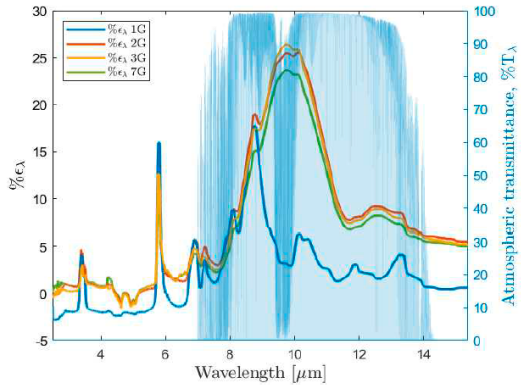

(b) Emittance curves of the samples 1G, 2G, 3G and 7G.

Figure 3.33: Emittance curves of the samples of the relevant sample sets [41].

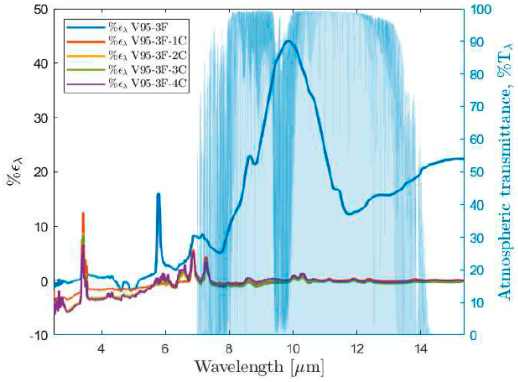

(a) Emittance curves of the samples V95-3F, V95-3F-1C, V95-3F-2C, V95-3F-3C, V95-3F-4C.

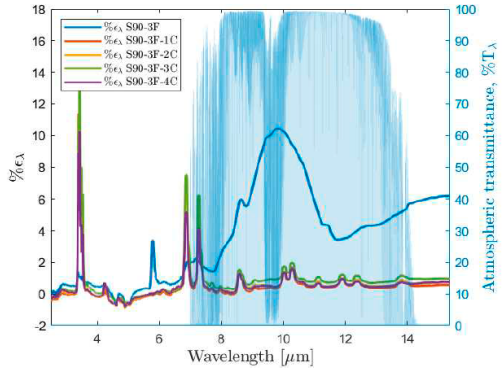

(b) Emittance curves of the samples S90-3F, S90-3F-1C, S90-3F-2C, S90-3F-3C, S90-3F-4C.

Figure 3.35: Emittance curves of the samples of the V95 and S90 sample set [41].

3.3.2 Thermal Performance: Temperature Drop and Cooling Power

Outdoor tests over three consecutive days showed that both the enclosed (S1) and open (S2) configurations reached sub-ambient temperatures when solar irradiance was below 600 Wm^{-2}, while for the regions beneath the samples and the EPS lid, the threshold was about 430 Wm^{-2}. Under peak irradiance, the enclosed sample (S1) exhibited higher temperatures due to the stagnant air layer, whereas the open sample (S2) remained cooler. Cooling power measurements indicated that despite slightly lower nighttime values for S1, both setups could exceed 100 Wm^{-2} when the sky temperature dropped below 5°C. Net cooling, evidenced by negative ΔT, was consistently linked to irradiance levels below 600 Wm^{-2} [38].

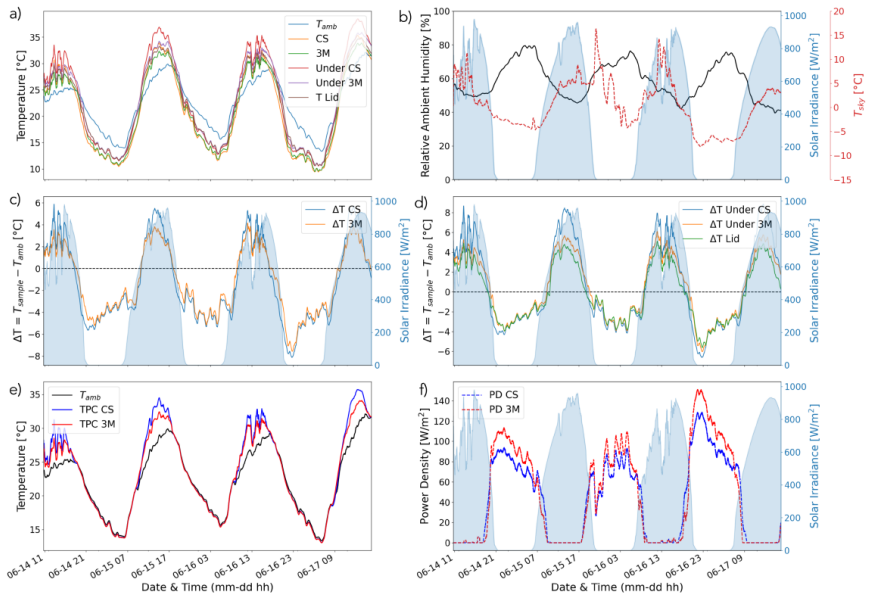

Figure 3.36: a) Ambient temperature and sample temperatures for the enclosed (S1) and open (S2) conditions, including temperatures under both samples and the lid that covers the EPS sample holder. b) Relative ambient humidity, solar irradiance, and sky temperature as a proxy to the presence of clouds. c) Temperature difference ΔT calculated as the difference between the S1 and S2 temperature and ambient. d) Temperature difference ΔT calculated as the difference between the temperature under S1, S2 and lid and ambient. e) Sample temperature for enclosed and open conditions monitored during the P_{cool} measurement, using ambient temperature as the set point. f) Net cooling power measured for both configurations [38].

The ΔT of the enclosed and open configurations are represented and compared in Figure 3.36, with reference to morning (5–11), midday (11–17), afternoon (17–23), and night (23–5) hours. In all periods except midday, both configurations show similar behavior, with a larger spread of ΔT observed during the afternoon. At midday, the most significant ΔT occurs, with the enclosed sample showing overheating peaks up to 6°C above ambient temperature, more than 2°C higher than the open configuration. From the measurements below the samples, similar results are obtained: Figure 3.36b shows that a ΔT peak exceeding 8°C is recorded at midday for U.S1 (enclosed), which is more than 3°C higher than the maximum U.S2 (open) reading [38].

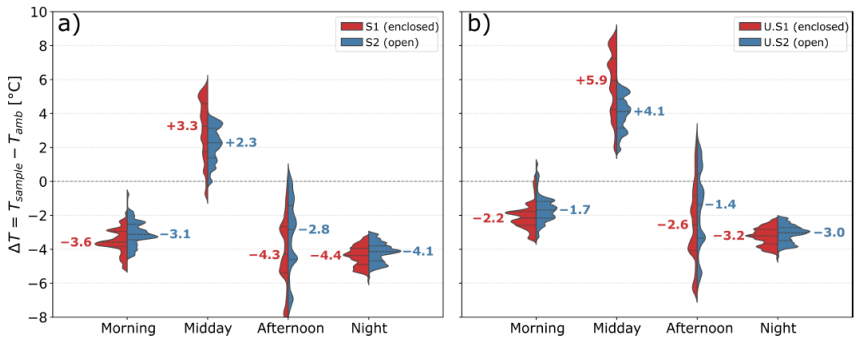

Figure 3.37: Split violin plot comparing the temperature difference ΔT for the following conditions: a) enclosed (S1) versus open (S2) sample and b) under the S1 and S2 samples. The values reported next to each distribution represent the median calculated for each time window over the three-day observation period [38].

3.3.3 Surface and Morphology: Optical Microscopy and AFM

The thicknesses of the PDRC samples were measured with the caliper and the results are shown below:

Table 3.8: Thicknesses of the optimized samples.

Samples thicknesses				
Sample	d_1 **[mm]**	d_2 **[mm]**	d_3 **[mm]**	$d_{\mathbf{avg}}$ **[mm]**
V95	0.56	0.50	0.54	0.53
3F	0.77	0.84	0.79	0.80
4F	0.88	0.95	0.93	0.92
V95-3F	0.71	0.68	0.68	0.69
V95-3F-1C	0.66	0.67	0.68	0.67
V95-3F-2C	0.87	0.89	0.79	0.85
V95-3F-3C	1.13	0.93	0.95	1.00
V95-3F-4C	1.27	1.18	1.35	1.27
S90	0.47	0.43	0.44	0.45
S90-3F	0.68	0.63	0.67	0.66
S90-3F-1C	0.65	0.61	0.64	0.63
S90-3F-2C	0.95	0.94	0.96	0.95
S90-3F-3C	1.21	1.06	1.07	1.11
S90-3F-4C	1.40	1.38	1.46	1.41

Morphological investigations were carried out using both the AFM NX-10 and the *Zeiss* optical microscope. An initial assessment of the coating surface was performed with the atomic force microscope (AFM), and the corresponding topographical image is presented in Figure 3.38. Post-processing of the acquired data revealed the pronounced roughness and irregularity of the surface, with a root mean square (RMS) value of approximately 1.31 μm.

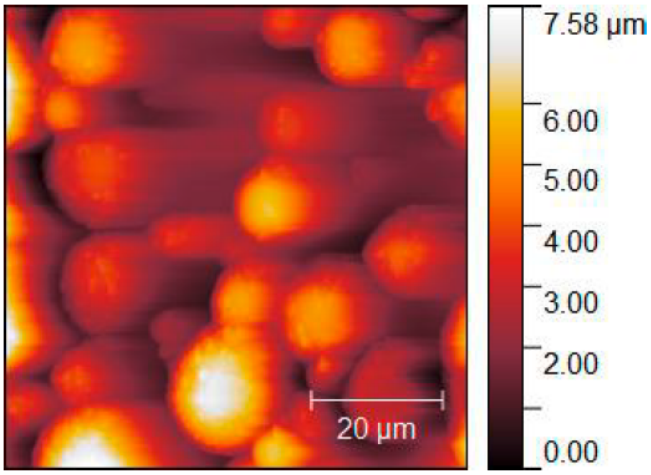

Figure 3.38: Surface topography measured by AFM [41].

An optical image of the V95-3F-1C sample was acquired and is presented in Figure 3.39. The image reveals that distinct surface features come into focus at varying depth levels. This behavior can be attributed to the size distribution of the silica microparticles and to the intrinsic non-uniformity of the coating, which is likely associated with the deposition technique employed during its application.

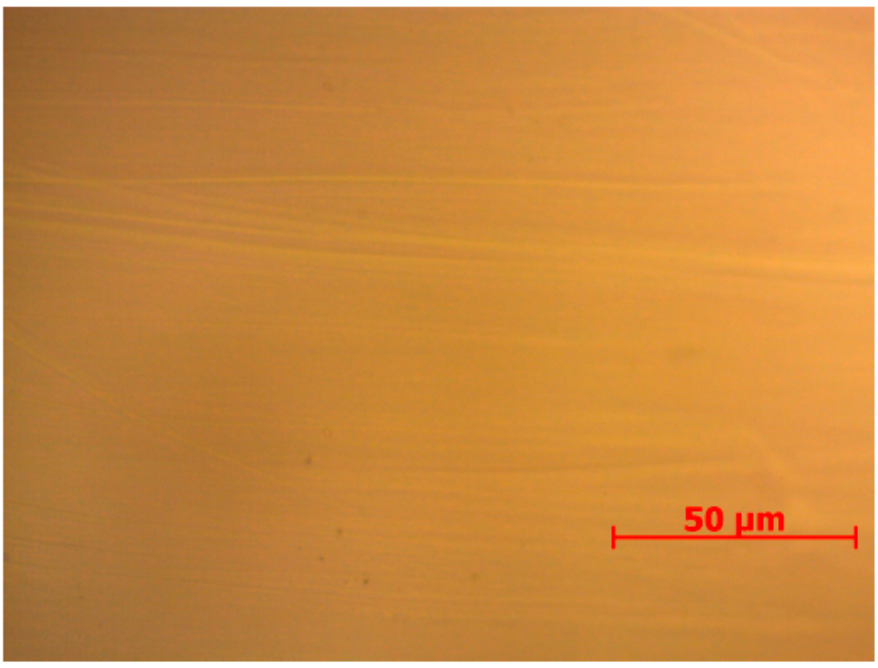

Figure 3.39: Morphology of sample V95-3F-1C acquired with Zeiss optical microscope at focus depth of 50x/0.75 [41].

Below, the results of the analyzed morphologic characterization of the V95-3F and S90-3F samples are shown.

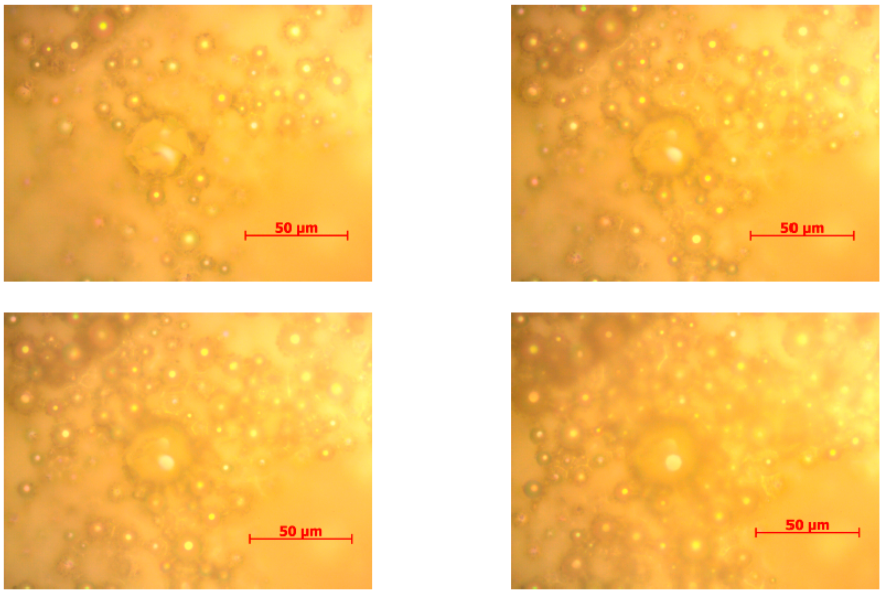

Figure 3.40: Morphology of sample V95-3F acquired with Zeiss optical microscope at focus depth of 50x/0.75 [41].

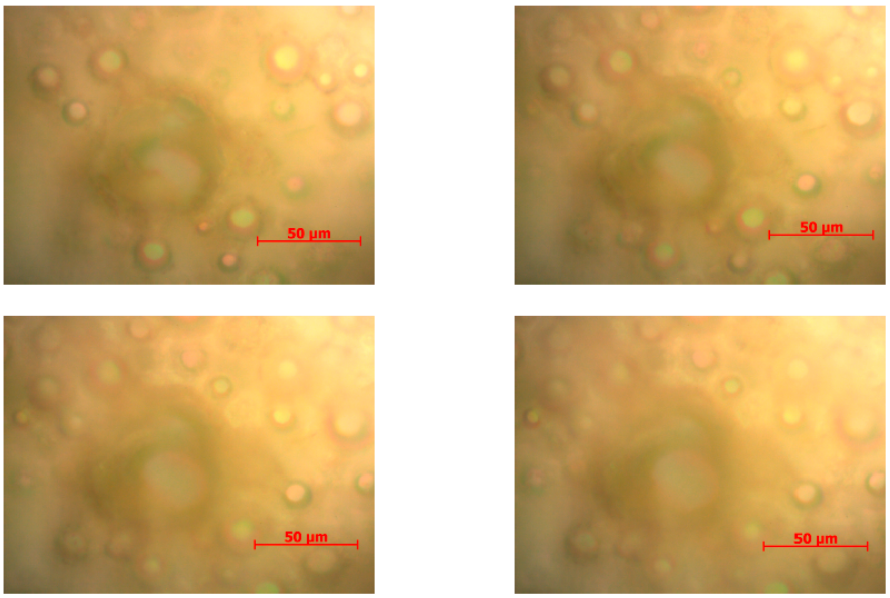

Figure 3.41: Morphology of sample V95-3F acquired with Zeiss optical microscope at focus depth of 100x/0.8 [41].

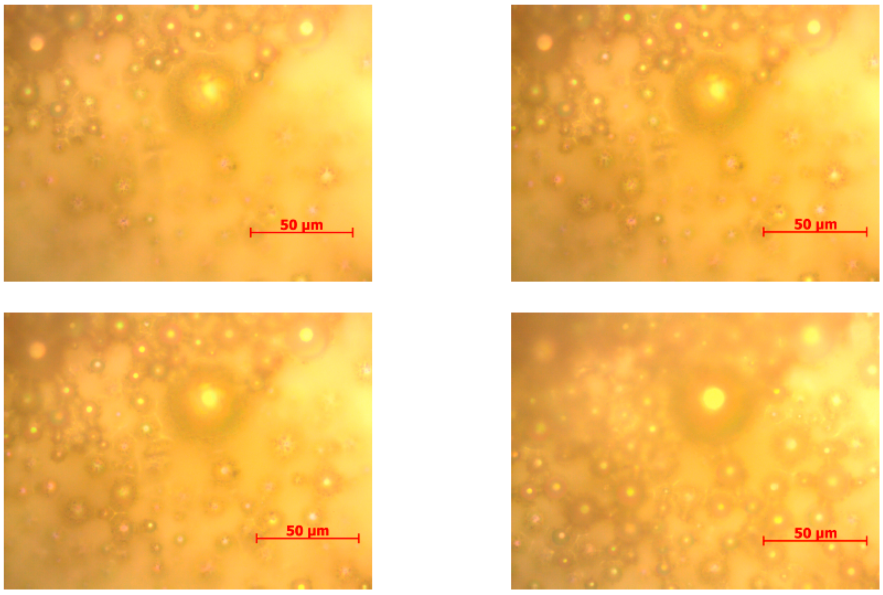

Figure 3.42: Morphology of sample S90-3F acquired with Zeiss optical microscope at focus depth of 50x/0.75 [41].

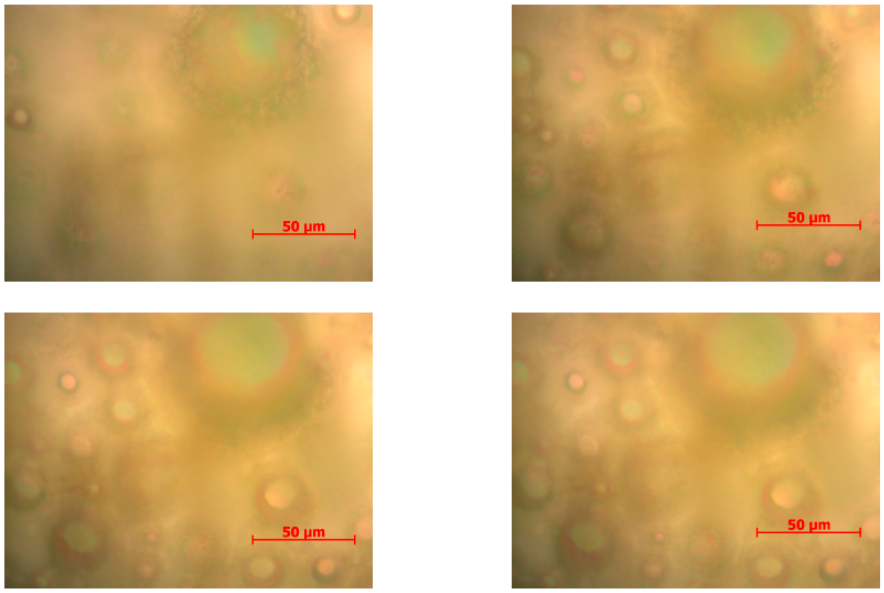

Figure 3.43: Morphology of sample S90-3F acquired with Zeiss optical microscope at focus depth of 100x/0.8 [41].

Although paint-based and nanoporous film coatings achieved very high solar reflectance (above 94%) and strong infrared emissivity within the 8–13 µm window, near-infrared (NIR) spectral dips arising from the nanoporous membrane reduced spectral smoothness, and the long-term mechanical durability of

the paint–film assembly remained uncertain.

For this reason, the research was redirected toward the development of intrinsically engineered disordered multilayer structures, designed to achieve both high solar reflectance and selective infrared emissivity without relying on external membranes. In our next study, proposed boron nitride (BN) nanofibers embedded in a polymer matrix are employed to construct gradient and multilayered architectures that enhance optical control, providing a more robust and stable pathway toward efficient daytime radiative cooling.

4

Design and Numerical Modeling of High Reflective Paints

Optical disorder disrupts long-range periodicity (which allows us to mimic realistic spectrum under sunlight) and causes complex scattering paths. Materials that use the PRC methodology suppress spectral resonances by leveraging the scattering arising from this disorder, achieve better reflection performance in the solar spectrum by utilizing polarization, and provide a robust pathway for scalable coatings.

In this chapter, we outline a numerical approach to analyze how optical disorder in PRC coatings governs scattering, reflection, and emission properties. To overcome the limitations of our experimental PRC coatings, we developed a full-wave electromagnetic simulation framework based on the Finite Element Method (FEM) using COMSOL Multiphysics. We carried out numerical analysis during our study while developing a model that consists of a semi-infinite air, a disordered scattering layer of high-index dielectric particles ($n = 2.3$) embedded in a low-index polymer matrix ($n = 1.3$), a thin silver reflector, and a bulk substrate of Al modeled with complex permittivity. Two geometries were investigated: a five-layer stacked structure (5LS) with particle sizes increasing from 100 nm to 600 nm to maximize broadband scattering, and a single-layer dense-to-coarse gradient structure (DtC) with decreasing packing density to promote diffuse solar rejection [52]. In the following sections, the methodology of the modeled structures and simulations will be examined, and their optical performance will be demonstrated.

4.1 Design and Methodology

Metasurfaces, consisting of subwavelength nanostructures or scatterers, offer a powerful method for tuning spectral properties at targeted wavelengths. Previous studies have demonstrated that disordered photonic structures can be engineered to control optical scattering and wave interference, enhancing radiative cooling performance in high-refractive-index inclusions within a low-refractive-index polymer matrix, light-matter interactions can be manipulated, leading to tailored scattering behaviors.

One of the key challenges in designing high-performance radiative cooling surfaces is achieving an optimized spectral response, ensuring high reflectivity in the solar spectrum (0.3–2.5 μm) while maintaining strong emissivity in the mid-infrared range. Metasurfaces, composed of subwavelength structures, provide a novel approach to precisely control optical scattering and emissive properties. By embedding dielectric or metallic scatterers within a polymer matrix, we can enhance light scattering and modify the effective refractive index distribution, optimizing the cooling efficiency of the surface.

Recent research has demonstrated that disordered photonic structures, such as randomly arranged dielectric or metallic scatterers, can be used to optimize reflectance and emissivity. Such structures leverage wavefront shaping to extend optical path lengths, thus increasing the effective interaction between light and the medium.

This study builds upon these principles by investigating how varying scatterer density gradients and the variations in the size of the scatterers in each scattering gradient density section influence passive radiative cooling efficiency.

In this section, a detailed description of the computational approach used in COMSOL Multiphysics is presented. The primary objective is to maximize the reflectance of the scatterer matrix in the absence of the mirror and to use the computed reflectance values as input for the PRC model. The methodology involves defining an appropriate geometrical structure, material properties, boundary conditions, meshing strategy, and solver configurations to ensure accurate simulation of electromagnetic wave interactions. The study follows best practices for numerical modeling, considering periodic conditions and a detailed parametric sweep to evaluate the spectral response.

4.1.1 Definition of the Optical Architecture and Material System

The optical system investigated in this study is designed to maximize solar reflectance in the 280–2500 nm wavelength range while simultaneously providing strong, selective thermal emissivity in the mid-infrared atmospheric transparency window (8–13 µm). Achieving this balance is the cornerstone of effective passive radiative cooling (PRC). The guiding principle is that broadband scattering from disordered dielectric structures must be combined with material dispersion engineering and reflective backing layers to fully optimize the spectral response.

Scattering Phase – BN Nanofibers

The scattering medium is composed of boron nitride (BN) nanofibers, chosen for their high refractive index ($n \approx 2.3$) and low optical losses across the visible and near-infrared. Their elongated morphology and random orientation significantly enlarge the effective scattering cross-section, leading to both volumetric and backscattering enhancement. This ensures that photons entering the coating are multiply scattered until they are reflected back to the environment or selectively absorbed in the thermal infrared. As confirmed by earlier scattering studies, tuning the scatterer diameter to the sub-wavelength and micron regime (200–600 nm) is key to matching solar wavelengths and producing broadband reflectivity [53, 54].

Matrix Phase – Low-Index Polymer

The BN nanofibers are embedded in a fluorinated polymer host, with refractive index $n \approx 1.3$ (PVDF-class). The polymer plays both mechanical and optical roles: it ensures homogenous dispersion of nanofibers to prevent agglomeration, while its intrinsic absorption bands in the 8–13 µm window promote selective thermal emission. This refractive index contrast between BN and the polymer matrix underpins strong Mie scattering in the solar spectrum while preserving high emissivity in the infrared. Moreover, the polymer matrix is compatible with large-scale electrospinning fabrication, enabling cost-effective scalability [25, 6].

Reflective Backing – Ag/Al Bilayer

To suppress transmission and recycle forward-scattered light, a reflective sub-

strate consisting of a thin silver (Ag) film (100 nm) deposited on bulk aluminum (Al) is incorporated beneath the nanofiber–polymer composite. The Ag/Al bilayer ensures high broadband reflectivity in the solar range and prevents radiative leakage into the substrate. Optical constants for Ag and Al are taken from the Johnson–Christy and Rakic datasets to ensure accuracy. This reflective base not only increases constructive interference in the visible range but also stabilizes mid-infrared emissivity by minimizing substrate absorption, a mechanism consistent with theoretical back-reflector models in metasurface PRC research [55, 56].

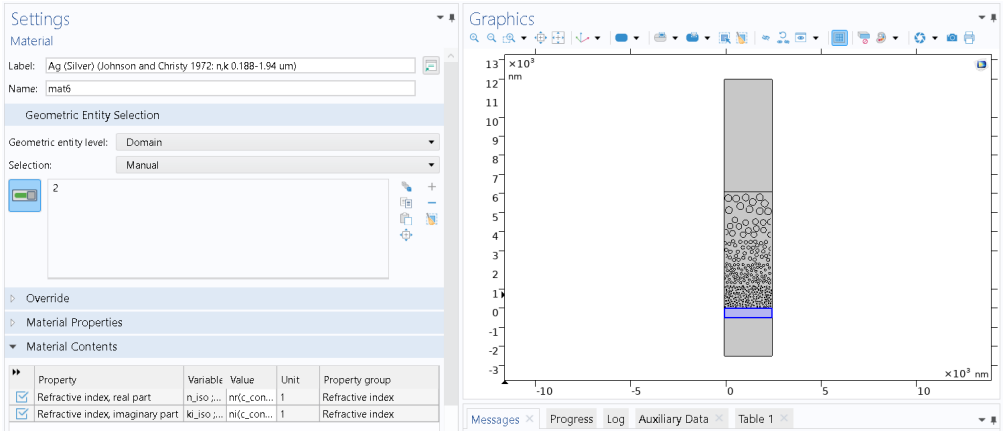

Figure 4.1: Configuration base of the reflective backing - mirror (Ag) structure into COMSOL MUltiphysics 6.2

Two primary design strategies are implemented, each exploring different gradient-disorder paradigms:

1. **Five-Layer Stacked (5LS) Architecture:** Five vertically stacked sublayers with BN fiber diameters of 100, 200, 300, 500, and 600 nm, arranged with a decreasing packing fraction from bottom to top. This multi-layer stratification is introduced to suppress modal dips, enhance inter-layer scattering, and smooth the overall reflectance spectrum. The graded sequence mimics a discrete gradient-index medium, enabling both spectral selectivity and angular robustness.

2. **Dense-to-Coarse (DtC) Architecture:** A single thick layer with a vertical density gradient, where fibers transition from a densely packed base to a sparse upper region. This arrangement imitates natural gradient-porous systems (e.g., biological tissues) where gradual density changes re-

duce reflection losses and maximize omnidirectional backscattering. Unlike multilayer 5LS, the DtC design prioritizes manufacturability and scalability, offering a simpler route for practical implementation while retaining strong optical performance.

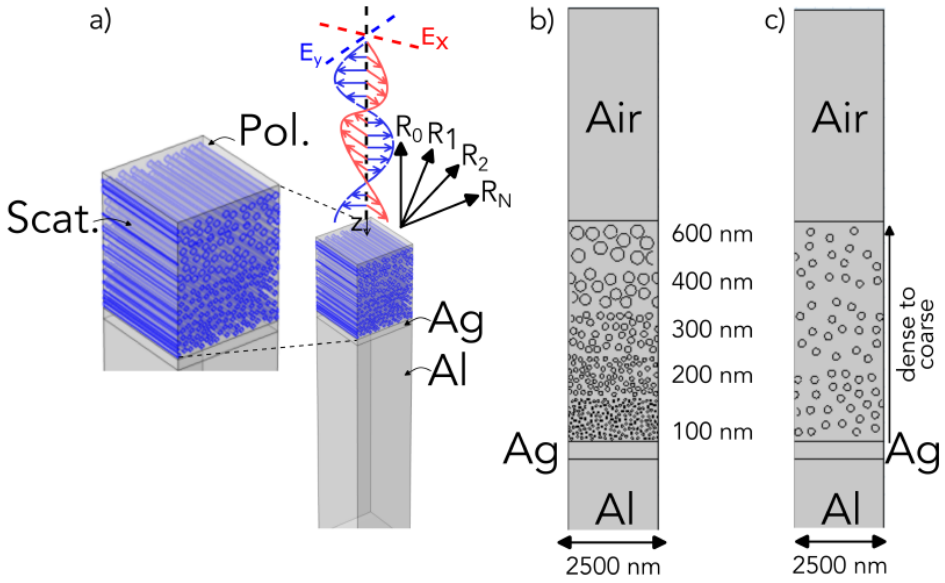

Figure 4.2: A structure of the simulated structure made by five-layer stacked (5LS) structure with 100–600 nm scatterers size a) and single-layer with vertical dense-to-coarse (DtC) scatterers size gradient b).

These architectural decisions directly link to the theoretical principles of gradient-index metasurfaces and scattering-based PRC. By varying scatterer size, density, and refractive index contrast, one tunes Mie scattering resonances, multiple scattering paths, and effective refractive index gradients [57]. When combined with reflective substrates, these disordered nanostructures behave as graded metasurfaces: they reject solar radiation by exploiting broadband scattering while emitting efficiently in the mid-infrared. The 5LS and DtC models thus represent two complementary approaches: one emphasizes spectral smoothness through discrete stratification, the other emphasizes scalability through continuous disorder, both with the aim of high R_{solar} and strong $\varepsilon_{(8-13\ \mu m)}$ under realistic outdoor conditions.

4.1.2 Electromagnetic (EM) numerical model

A COMSOL Multiphysics model (Electromagnetic Waves, Frequency Domain; EWFD) was built to study, characterize, and optimize the optical response of BN–nanofiber based PRC coatings. The geometry is treated as a 2D cross–section extruded out of plane, which captures the in–plane disorder while remaining computationally tractable. To control the computational domain and emulate an infinitely repeating structure, the lateral extent was set to 2500nm and periodic boundary conditions were imposed on the vertical sides. The upper region is semi–infinite air and the stack below is Ag/Al reflector. Perfectly matched layers (PMLs) were placed on the top and bottom to suppress spurious reflections.

Ports, polarizations, and diffraction orders

Input and output ports were defined at the top and bottom boundaries, respectively. The optical response was computed separately for transverse–electric (TE) and transverse–magnetic (TM) polarizations. Diffraction orders at the input and output ports were truncated after 12 (TE) and 18 (TM) orders, which we found sufficient for convergence across the solar band. To mimic unpolarized sunlight and to smooth modal anisotropies, the two reflectances were averaged

$$R_{\mathrm{unpol}}(\lambda) = \frac{R_{\mathrm{TE}}(\lambda) + R_{\mathrm{TM}}(\lambda)}{2}. \tag{4.1}$$

Disorder, meshing, and near–boundary treatment

Scatterer size and position randomness were sampled systematically to ensure spectral flattening and angle–polarization insensitivity. Local mesh refinement was applied near dielectric–metal interfaces and around nanofibers to resolve strong field gradients, while keeping a coarser mesh in the far field and inside PMLs for efficiency.

From the S–parameters at the ports we extract spectral reflectance, transmittance, and absorptance, $R(\lambda)$, $T(\lambda)$, $A(\lambda)$. Overall solar performance is reported

as AM1.5G–weighted solar reflectance (SWR)

$$\mathrm{SWR} = \frac{\displaystyle\int_{280\,\mathrm{nm}}^{2500\,\mathrm{nm}} R_{\mathrm{unpol}}(\lambda)\, I_{\mathrm{solar}}(\lambda)\, \mathrm{d}\lambda}{\displaystyle\int_{280\,\mathrm{nm}}^{2500\,\mathrm{nm}} I_{\mathrm{solar}}(\lambda)\, \mathrm{d}\lambda}. \tag{4.2}$$

The TE/TM decomposition with finite diffraction–order truncation yields a physically realistic unpolarized spectrum and suppresses artificial ripples in the 400–1100nm window. The lateral periodicity of 2500nm provides a good compromise between capturing near–field gradients and controlling runtime. The Ag/Al backing eliminates transmission and recycles forward–propagating photons, which is critical for achieving high R_{solar}. In contrast, thin Al without bulk backing or glass substrates lead to a marked SWR drop, confirming the necessity of a high–quality metal reflector.

- Physics: EWFD, frequency–domain sweep across the solar band.
- Lateral width: 2500nm; side boundaries periodic. Top air half–space; bottom Ag (100nm) on bulk Al.
- Top and bottom: PMLs plus wave ports for in/out coupling.
- Polarizations: solve TE and TM independently; average to obtain R_{unpol}.
- Diffraction orders: 12 (TE), 18 (TM) at input and output ports.
- Meshing: refined around nanofibers and metal interface; coarser in PMLs.
- Post–processing: $R(\lambda), T(\lambda), A(\lambda)$, AM1.5G–weighted SWR via the integral above.

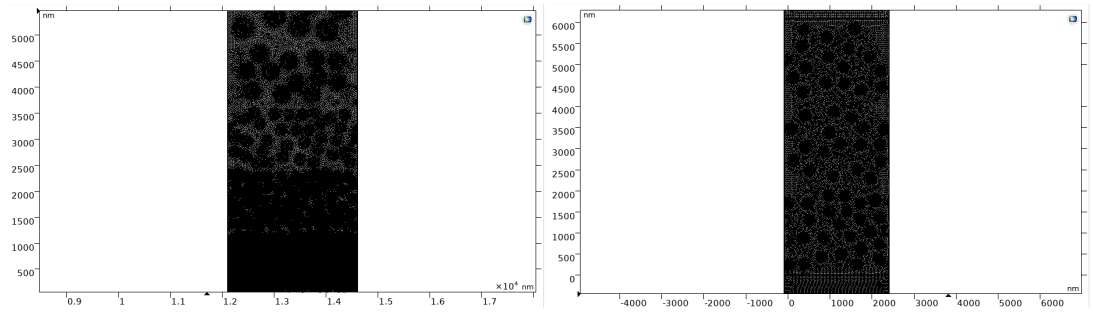

(a) (b)

Figure 4.3: A mesh configuration of simulated structure made by five-layer stacked (5LS) structure with 100–600 nm scatterers size a) and single-layer with vertical dense-to-coarse (DtC) scatterers size gradient b).

4.1.3 Thermal Modeling

To translate the spectrally resolved optics into temperature and cooling power, the computed $R(\lambda), T(\lambda), A(\lambda)$ are embedded in a COMSOL Multiphysics thermal framework combining *Heat Transfer in Solids* and *Surface–to–Surface Radiation*. The numerical experiment models a concrete block under ambient and solar radiation, with its top surface coated by different PRC candidates (black paint, ideal PRC, prior nanoporous PRC, DtC, 5LS), while retaining the wavelength dependence of irradiation, surface and sky emissivity through band discretization and direct import of EM spectra.

A 3D slab (concrete substrate) is capped by a thin surface coating whose optical properties are provided as spectral inputs. Heat exchange includes conduction in the solid, mixed convection to air through a film coefficient, and radiative exchange with the sky and surroundings via view factors (surface–to–surface radiation). The upper boundary is the radiating surface exposed to the hemisphere; lateral and bottom boundaries are thermally insulated to emulate a semi–infinite substrate over the time window considered.

Spectral inputs from EM model

From the EM model we import: (i) the AM1.5G solar absorptance $\alpha_\odot$ defined by

$$\alpha_\odot = \frac{\displaystyle\int_{280\,\mathrm{nm}}^{2500\,\mathrm{nm}} A(\lambda)\, I_\odot(\lambda)\, \mathrm{d}\lambda}{\displaystyle\int_{280\,\mathrm{nm}}^{2500\,\mathrm{nm}} I_\odot(\lambda)\, \mathrm{d}\lambda}, \tag{4.3}$$

and (ii) the emissivity curve $\varepsilon(\lambda)$, with emphasis on the atmospheric window (AW).

Simulation scenarios
The five coating cases investigated are:

1. **Black coating:** $\alpha \simeq 1$.
2. **Ideal PRC:** $\alpha \simeq 0.1$ with strong, selective AW emissivity.
3. **Prior nanoporous PRC:** $\alpha \simeq 0.05$ (selective AW emissivity).
4. **DtC (Ag/Al):** $\alpha \simeq 0.0267$, spectrum from the dense-to-coarse architecture.
5. **5LS (Ag/Al):** $\alpha \simeq 0.019$, spectrum from the five-layer stacked architecture.

For DtC and 5LS, the full $R(\lambda)$ and $\varepsilon(\lambda)$ curves computed in Section 4.2.1 are passed to the thermal model; for the benchmarks (ideal PRC and prior nanoporous PRC) selective emissive templates from the literature are adopted.

Spectral bands and sky model
Four bands are used to map the wavelength dependence of irradiation and emissivity: UV–VIS, NIR, and MIR split at 8–13 μm to explicitly represent the atmospheric window (AW). Irradiation from the ambient surroundings is modeled as blackbody radiation at the ambient temperature,

$$e_b(T_{\text{amb}}) = \sigma T_{\text{amb}}^4, \tag{4.4}$$

while the long–wave input from the sky adopts a gray–sky model,

$$e_b(T_{\text{amb}}) = \varepsilon_{\text{sky}}\, \sigma T_{\text{amb}}^4, \tag{4.5}$$

with ε_{sky} set by the dew–point (clear–sky) proxy and fixed to a low value within the 8–13 μm band ("ambient emissivity" ≈ 0.2 for a clear sky), reflecting the high transparency of the AW. This choice is consistent with our optical selectivity targets and with the literature PRC modeling practice used in the paper's thermal section.

Meteorological forcing and wind correction
Meteorological data are taken from the ASHRAE 2021 database for *Venice Airport (IT)*, day–time window *1–3 June* (48 h). Following the COMSOL guide, the

effect of wind on convective heat removal is accounted for by using a corrected ambient temperature,

$$T_{\mathrm{amb}} = \langle T_{\mathrm{Station}} \rangle - \Delta T_{\mathrm{wind}}, \tag{4.6}$$

where the reduction ΔT_{wind} depends on the recorded wind speed. The correction preserves daytime cooling while preventing an overestimation of nocturnal over-cooling.

Post-processing and figures of merit

The temperature field is advanced over 48 h using the measured diurnal forcing. The figures of merit extracted are: (i) surface temperature offset $\Delta T = T_{\mathrm{coat}} - T_{\mathrm{amb}}$, (ii) net cooling power $P_{\mathrm{cool}} = P_{\mathrm{rad}} - P_{\mathrm{sun}} - P_{\mathrm{atm}} - P_{\mathrm{conv}}$, and (iii) daytime peak sub-ambient performance. These indicators enable direct comparison among coating configurations in realistic boundary conditions.

4.2 Results and Discussion

4.2.1 Reflectance Performance and SWR Analysis

This section presents an extensive analysis of the results of the COMSOL Multiphysics simulation. The primary aim of these simulations is to optimize the reflectance of the designed scatterer matrices for efficient solar spectrum manipulation.

Here are the reflectance performances of the 2 proposed samples in solar spectra based on the COMSOL Multiphysics simulation environment.

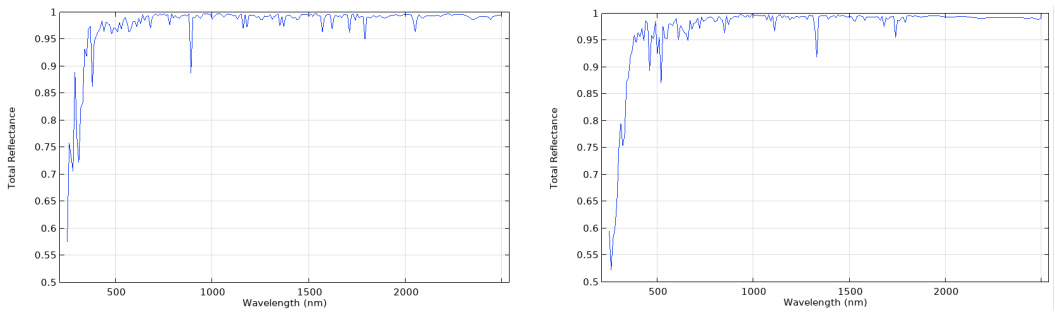

(a) (b)

Figure 4.4: Reflection Performance Output based on the COMSOL Multiphysics simulations. a) represents the 5LS coating design with scatterers on Al substrate using reflective Ag layer as mirror. b) shows the same design for DtC structure.

The raw reflection curves obtained from COMSOL in the solar spectrum for the 6 different material combinations examined were processed using a moving-mean filter in MATLAB. The normalized and weighted SWR results obtained and the mid-IR emissivity performance of the structures studied are presented below.

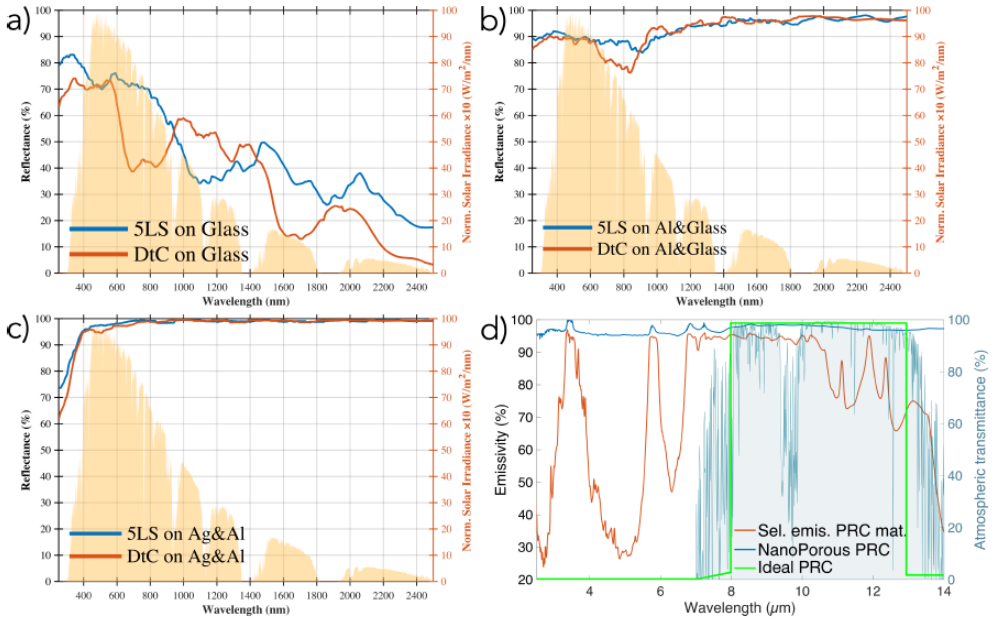

Figure 4.5: Reflectances calculated in the solar spectrum for 5LS (blue solid line) and the DtC (orange solid line) in the following configurations: (a) on glass substrate, (b) on a thin layer of Al on Glass substrate, and (c) on a thin layer of Ag on Al bulk substrate. In all cases, the second y-axis reports the normalized AM1.5G solar irradiance profile. (d) Reports the hemispherical emittance for the Nanoporous PRC material (blue solid line), the selective emissive one [38] used in these calculations (orange solid line), and the green solid line indicates the ideal PRC emittance. The second y-axis reports the normalized atmospheric transmittance (bluish area) [38].

To evaluate the solar reflectance potential of the proposed PRC designs, we computed the Solar-Weighted Reflectance (SWR) by integrating the reflectance spectra over the AM1.5G solar irradiance profile as in formula 4.2.

(a) 5LS Geometry: The five-layer stacked structure achieves an SWR of 98.10% when supported by a reflective silver/aluminium substrate. This value overpass the 95% threshold often cited in the PRC literature as a benchmark for effective passive daytime radiative coolers. In case the coating is directly applied on a thin Al layer deposited on glass the SWR results 89.98%, while in absence of

any metallic backing, the SWR drops significantly to 61.98%. This highlights the critical role of the bottom reflective layer in redirecting forward-scattered light and enhancing the net upward reflectance. The multilayer arrangement, with its graded particle sizes, further promotes inter-layer scattering and suppresses spectral dips, resulting in a more uniform and stable reflectance spectrum.

(b) DtC Gradient Geometry: For the single-layer dense-to-coarse configuration, the SWR reaches 97.33% with the reflective Ag/Al substrate in place, which is slightly lower than its multilayer counterpart. The lack of discrete interfacial transitions may reduce scattering efficiency in the longer wavelengths. When the coating is applied on a thinn Al layer on glass the SWR drops to 87.82% and if it is directly applied on glass substrate the SWR decreases dramatically to 52.50%, again underscoring the importance of reflective support. The gradient-based design, while simpler and potentially easier to fabricate, is more susceptible to spectral irregularities and losses, especially in the near-infrared region.

Table 4.1: SWR Performance of surfaces coated with different scatterer configurations (5LS or DtC) and different substrates, namely glass without Al layer, glass with the Al layer and thin Ag layer on Al substrate.

Coating composition	Coating with the scatterers on glass (without reflective Al layer)	Coating with the scatterers on glass (with reflective Al layer)	Coating with the scatterers on Al substrate (with reflective Ag layer)
5LS	61.98%	89.98%	98.10%
DtC	52.59%	87.82%	97.33%

In summary, both 5LS and DtC architectures exhibit broadband reflectance suitable for PRC, with a metallic back-reflector being essential for high solar-weighted reflectance. The five-layer geometry, combining optical disorder with hierarchical structuring, provides superior spectral uniformity and robustness, achieving $> 98\%$ SWR on Ag/Al substrates compared to $\sim 97\%$ for DtC. Multi-polarization resolved simulations (s- and p-) proved crucial for reliable estimates, eliminating artificial jaggedness from modal interference in the 400–1100 nm range and yielding smoother, more uniform reflectance profiles with average efficiencies of 97–98%, depending on geometry.

4.2.2 Thermal Modeling of PRC Materials Under Realistic Conditions

The thermal simulations demonstrate the temperature evolution inside a hollow concrete block when its upper surface is coated with different PRC candi-

dates under realistic outdoor conditions. Meteorological data from Venice were used as input, and the numerical framework enables direct comparison of how optical selectivity and reflectance translate into measurable temperature differences.

The results show that the black reference surface leads to the highest internal air-gap temperature, exceeding 45 °C at peak insolation. In contrast, the ideal PRC material maintains the cavity near 16.5 °C, while the nanoporous PRC stabilizes around 18.6 °C. The optimized DtC and 5LS architectures perform very close to the ideal benchmark, with values of 16.9 °C and 16.7 °C respectively, demonstrating that scattering-based designs combined with metallic reflectors can approach the theoretical cooling limit [52].

A further analysis including wind correction confirms that all PRC coatings retain significant sub-ambient cooling capabilities under dynamic forcing. The DtC and 5LS designs provide a temperature reduction of about 6 °C relative to ambient and up to 18 °C compared to the black surface, consistent with prior nanoporous experiments. Incorporating measured wind profiles reduces the apparent night-time overcooling while maintaining daytime performance. Overall, the study validates that engineered disordered coatings supported by metallic back-reflectors can robustly achieve sustained cooling under realistic environmental conditions[52].

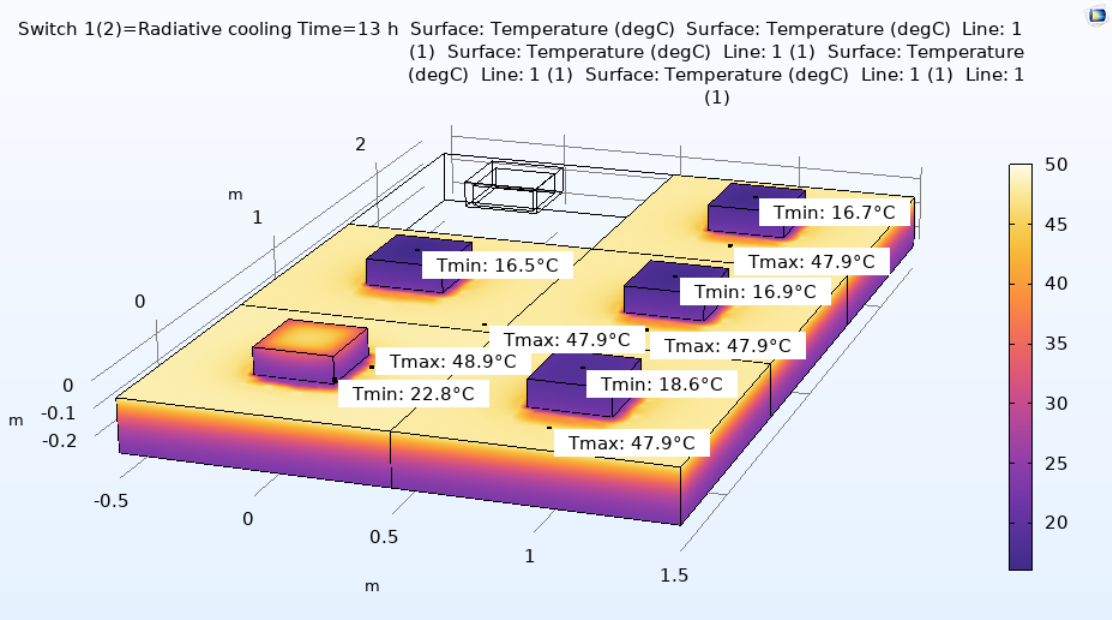

Figure 4.6: Thermal modeling considering a concrete box coated with a black coating, an ideal PRC material, the material experimentally tested on [38], the optimized DtC, and 5LS applied on the Ag/Al substrates [52].

Post-processing and figures of merit

Under Venice-June forcing, both DtC (Ag/Al) and 5LS (Ag/Al) reach midday subambient values of approximately **6 °C** and remain markedly cooler than a black reference by ~**18 °C** at peak insolation [38]. Wind correction reduces apparent overcooling at night while preserving the daytime gap among the cases; ideal PRC, DtC and 5LS track closely, whereas the previous nanoporous PRC sits slightly warmer due to higher α. These results corroborate the optical–thermal co-design rationale: a high solar-weighted reflectance combined with strong AW emissivity translates into sustained net cooling in realistic outdoor conditions.

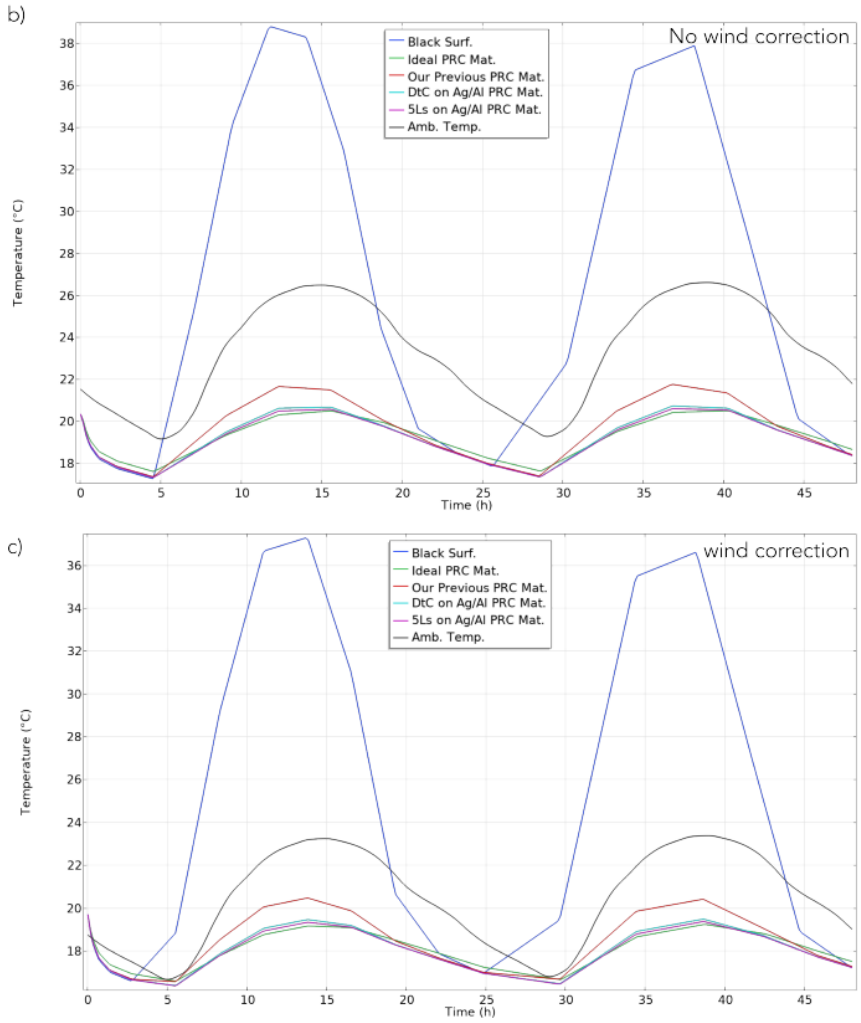

Figure 4.7: The corresponding temperatures without and with wind correction of the proposed thermal modeling as shown in 4.6 [52].

All runs use the same concrete substrate and view-factor setting; only the spectral inputs change across cases. A sensitivity sweep of $\varepsilon_{\mathrm{sky}}$ (clear to humid sky) is provided in the SI; the relative ranking of the coatings is robust, with absolute ΔT decreasing as humidity increases, consistent with AW closure.

Substrate/back–reflector effect

In a stepwise manner, the use of glass, Al, and Ag, and combinations thereof, has made it possible to address the scattering properties of disordered materials in a more comprehensive manner.

- A high quality metal back-reflector (Ag 100nm in bulk Al) eliminates transmission and recycles forward–propagating photons back into the scatter-

ing medium, which is essential to sustain the $>95\%$ reflectance level reported for the BN–nanofiber coatings.

- This observation is consistent across architectures (5LS and DtC) and is reproduced in all mesh/order-convergent runs.

Randomness sweeps and angular/polarization robustness
The optimized coatings also demonstrate robustness against variations in structural disorder and illumination conditions.

- Varying the number density, size distribution and spatial randomness of the nanofibers preserves the broadband character of $R_{\mathrm{unpol}}(\lambda)$, while moderate disorder further smooths the spectral features.

- Angular and polarization robustness is confirmed by computing $R(\lambda, \theta)$ for TE/TM, showing that the unpolarized reflectance remains weakly dependent on incidence angle across the solar band for both 5LS and DtC designs.

As a future step, the numerical designs presented here could be translated into practical coatings by developing scalable deposition routes for BN–polymer composites, introducing controlled gradients in particle size and density, and integrating reflective metallic substrates. Emphasis will be placed on ensuring homogeneous dispersion, structural stability, and reproducibility of the disordered architectures, while also assessing durability under environmental stresses. These fabrication efforts would provide the critical link between simulation and real-world implementation of high-performance PRC coatings.

5

Discussion and Conclusion

This thesis describes the systematic development and test results of nanoporous paint coatings on two aluminum substrates with different optical bases. The V95 multilayer stack ($Al/SiO_2/TiO_2$) provided over 95% visible reflectance, while the S90 Al/Al_2O_3 layer provided a 90% reference. Hollow glass microspheres (IM30K/IM16K) added to a low-VOC acrylic matrix increased broadband scattering and reduced density; $CaCO_3$ enhanced visible/NIR reflectivity; PVDF-HFP powders provided selective emission in the 8–13 µm range without solvents. A 16 µm thick, 40 nm porous Celgard C210 film, either placed directly on the paint or positioned 1.5 cm above it, separated both optical effects and convection artifacts. Single/multi-layer coatings on V95 and S90 were tested with commercial cooling paints and microsphere mixtures at thicknesses ranging from 0.14–1.4 mm.

Reflection measurements were performed in the 250–2650 nm range using the Cary 5000 UV-Vis-NIR Spectrophotometer device's integration sphere, and solar-weighted values were calculated according to ASTM G173. Some coatings on V95 achieved over 94% solar band reflectance, and 8G on S90 exceeded 90%. Celgard lamination provided additional gain with increasing layers; S90 provided 93.6–93.7% solar and 95.7–95.8% visible reflectance at three to four layers. Data measured in the 2.5–15 µm range with FTIR-ATR was converted to emission at 300 K using Kirchhoff's law. While the old set of paints showed 0.13–0.24 emission in LWIR, the free Celgard layer dropped to 0.004, highlighting the successful results obtained. Surface ATR measurements on multi-layer Celgard laminates yielded nearly zero emission, reflecting the membrane's low-

loss structure. Consequently, a balance region between high solar reflectivity and controlled thermal emission was defined.

Surface and morphology studies tied structure to performance. Caliper measurements confirmed the thickness ladder for each stacking strategy, for example V95-3F progressing from about 0.69 mm to about 1.27 mm as coats increased from one to four, and S90-3F moving from about 0.66 mm to about 1.41 mm. AFM in non-contact mode over 70 μm $\times$ 70 μm fields revealed a rough, highly irregular topography with about 1.31 μm RMS that is consistent with a porous, strongly scattering paint microstructure. Zeiss AXIO optical microscopy at 50$\times$ and 100$\times$ captured multi-depth focal planes where different silica spheres and binder features come into focus at different levels, highlighting the non-uniform, hierarchical surface that drives diffuse backscattering in the solar band.

The system measured the temperature difference and cooling power using NTC probes and a PID-controlled heater by monitoring the sample, environment, humidity, sky temperature, and radiation. Sub-ambient operation below 600 W/m^2 and sub-sample regions below 430 W/m^2 were confirmed. Suspended Celgard (S1) restricted convection and caused excessive heating up to 6°C at midday, whereas the direct laminated film (S2) was more stable. At night, cooling power of >100 W/m^2 was measured in both cases. However, PRC sample–related drops in NIR region concerns led us to adopt a strategy of designing BN-nanofiber-reinforced dispersed polymer structures.

Based on the previous experimental results, our study relies on designing PRC coating that preserves the benefits of paint system while addressing their weaknesses such as broad emissivity in the NIR-mid-IR. The framework shows broadband scattering must be co-designed with material dispersion and a high-quality back reflector to avoid suppressed-scattering windows. Boron nitride nanofibers in a low-index fluorinated matrix were validated as high-contrast, low-loss scatterers, with two morphologies compared: a five-layer stack (100–600 nm fibers) achieving the smoothest spectrum and highest SWR, and a dense-to-coarse gradient trading slight optical headroom for simpler fabrication while retaining controlled disorder.

The electromagnetic results define design rules that generalize lab outcomes. An Ag on Al back reflector is essential, raising SWR from 61.98% on glass to 98.10% on Ag/Al for 5LS. Unpolarized performance must average TE and TM to remove artificial ripples and represent sunlight realistically. Moderate positional/size disorder flattens modal features without loss of amplitude.

Then, a thermal model that consider PRC samples during a realistic daytime has been used to validate the proposed coatings. Both 5LS and DtC deliver daytime sub-ambient cooling, ~18°C cooler than black references at peak insolation, with 6°C daytime drops when the sky window is open. Sensitivity sweeps show higher humidity reduces absolute performance but not ranking. This reconciles outdoor tests where sub-ambient cooling occurred below 600 W m^{-2} and suspended films caused overheating. Thus, reliable PRC requires low solar absorptance with metal back reflectors, high 8–13 μm emissivity, and avoidance of convection-distorting shields.

Our experiments demonstrated the scalability of BN–nanofiber coatings, but also pointed to limitations in spectral control that motivate further design optimization. Simulations provide an upgrade route in which disorder for scalability, with selectivity and robustness embedded in design. Near term, DtC gradients can be implemented via roll-to-roll BN nanofibers on Ag/Al foils, validated optically and tested outdoors without enclosure artifacts. Mid term, durability and humidity-controlled trials should guide climate-specific deployment. Long term, adaptive infrared emission can address over-cooling. These BN-nanofiber architectures thus offer a manufacturable route from proof-of-concept to deployable PRC coatings.

In conclusion, this thesis reports experiments and numerical improvement on PRC materials to pave the way for relevant technologies in spontaneous cooling. It also pave the way for its use in real-world applications, highlighting its existing and promised benefits, and its importance within global consumption transformation chains, thereby contributing to a greener future.

Appendix

The raw COMSOL reflection curves for the 5LS and DtC structures (Fig. 4.4) exhibited sawtooth-like dips, which were smoothed into more physically meaningful trends using a moving average filter in the MATLAB listing 1.

Code 1: Implementation of moving-mean smoothing for reflectance data.

```
% Read and filter data (ignore comment lines starting with %)
data = readmatrix('total_reflection_data.txt');
data = data(~startsWith(string(data(:,1)), '%'), :);

% Wavelength (nm) and Reflectance
lambda = data(:,1);
R = data(:,2);

% Apply Moving Average (odd window = 11 gave better results)
R_smooth = movmean(R, 11, 'Endpoints', 'shrink');

% Plot Original vs Smoothed Curve
figure('Color','w'); hold on; grid on;
plot(lambda,R,'b-','LineWidth',1,'DisplayName','Original');
plot(lambda,R_smooth,'r-','LineWidth',2,'DisplayName','Moving Average
↪  (Smoothed)');
xlabel('Wavelength (nm)', 'FontSize',12);
ylabel('Reflectance', 'FontSize',12);
title('Reflectance Curve - Original vs
↪  Smoothed','FontWeight','bold','FontSize',13);
legend('Location','SouthEast'); xlim([250 2500]); ylim([0 1]);

% Export Smoothed Data
smoothedData = [lambda R_smooth];
writematrix(smoothedData,'Reflectance_Smoothed.csv');
save('Reflectance_Smoothed.mat','smoothedData');
```

References

[1] Avenston LLC. Low Energy Transition. 2019. URL: https://avenston.com/en/articles/low-energy-transition.

[2] Aaswath P Raman et al. "Passive radiative cooling below ambient air temperature under direct sunlight". In: Nature 515.7528 (2014), pp. 540–544.

[3] Eden Rephaeli, Aaswath Raman, and Shanhui Fan. "Ultrabroadband photonic structures to achieve high-performance daytime radiative cooling". In: Nano letters 13.4 (2013), pp. 1457–1461.

[4] Lulu Cheng et al. "Ultra-Efficient Passive Daytime Radiative Cooling Enabled by Dual-Selective Inorganic SiO2/Si3N4 Photonic Emitter". In: Laser & Photonics Reviews 19.12 (2025), p. 2500068.

[5] Yao Zhai et al. "Scalable-manufactured randomized glass-polymer hybrid metamaterial for daytime radiative cooling". In: Science 355.6329 (2017), pp. 1062–1066.

[6] Jyotirmoy Mandal et al. "Hierarchically porous polymer coatings for highly efficient passive daytime radiative cooling". In: Science 362.6412 (2018), pp. 315–319.

[7] Xiangyu Li et al. "Ultrawhite BaSO4 paints and films for remarkable daytime subambient radiative cooling". In: ACS applied materials & interfaces 13.18 (2021), pp. 21733–21739.

[8] Minjae Lee et al. "Photonic structures in radiative cooling". In: Light: Science & Applications 12.1 (2023), p. 134.

[9] Chengxuan Gong and Gaige Zheng. "Selective properties of mid-infrared Tamm phonon-polaritons emitter with Silicon carbide-based structures". In: Micromachines 13.6 (2022), p. 920.

[10] Francisco J Alfaro-Mozaz et al. “Deeply subwavelength phonon-polaritonic crystal made of a van der Waals material”. In: Nature communications 10.1 (2019), p. 42.

[11] Yeqing Zhu et al. “Quasi-periodic selective multilayer emitter for sub-ambient daytime radiative cooling”. In: AIP Advances 11.2 (2021).

[12] Krutarth Khot, Prabudhya Roy Chowdhury, and Xiulin Ruan. “Machine learning-based design optimization of aperiodic multilayer coatings for enhanced solar reflection”. In: International Journal of Heat and Mass Transfer 224 (2024), p. 125303.

[13] Huaiyuan Yin and Chunzhen Fan. “Realization of an Efficient Radiative Cooling Emitter with Only Double Layer Inorganic Sio2 and Tio2 Metamaterial”. In: Available at SSRN 4257697 ().

[14] Chongjia Lin et al. “Pushing radiative cooling technology to real applications”. In: Advanced Materials 37.23 (2025), p. 2409738.

[15] Weimin Wang et al. “Performance assessment of a photonic radiative cooling system for office buildings”. In: Renewable Energy 118 (2018), pp. 265–277.

[16] Yile Fan et al. “Angular selective optical metasurfaces: Fundamentals, progress and applications”. In: Materials Science and Engineering: R: Reports 166 (2025), p. 101055.

[17] Tao Wang et al. “Colored Radiative Cooling: from Photonic Approaches to Fluorescent Colors and Beyond”. In: Advanced Materials 37.15 (2025), p. 2414300.

[18] Siavash Shahriarbahrami Pour and Amir Nader Askarpour. “A simple, cheap and effective glass coating for selective solar transmittance and radiative cooling applications”. In: Optical Materials 147 (2024), p. 114751.

[19] Shixiong Yu et al. “Photonic-structure colored radiative coolers for daytime subambient cooling”. In: Nano Letters 22.12 (2022), pp. 4925–4932.

[20] Junren Wen et al. “Thin film-based colorful radiative cooler using diffuse reflection for color display”. In: PhotoniX 4.1 (2023), p. 25.

[21] Seok-Beom Seo et al. “Visible transparency modulated cooling windows using pseudorandom dielectric multilayers”. In: Nanophotonics 14.10 (2025), pp. 1587–1595.

[22] Muhammad A Butt. "Thin-film coating methods: a successful marriage of high-quality and cost-effectiveness—a brief exploration". In: Coatings 12.8 (2022), p. 1115.

[23] Andrea Felicelli et al. "Thin layer lightweight and ultrawhite hexagonal boron nitride nanoporous paints for daytime radiative cooling". In: Cell Reports Physical Science 3.10 (2022).

[24] Gopalakrishna Gangisetty and Ron Zevenhoven. "A review of nanoparticle material coatings in passive radiative cooling systems including skylights". In: Energies 16.4 (2023), p. 1975.

[25] Tong Wang et al. "A structural polymer for highly efficient all-day passive radiative cooling". In: Nature communications 12.1 (2021), p. 365.

[26] Linhu Li et al. "Durable hybrid metamaterial with hierarchically porous structure for efficient passive daytime radiative cooling". In: Chemical Engineering Journal 498 (2024), p. 155516.

[27] Kaixin Lin et al. "Hierarchically structured passive radiative cooling ceramic with high solar reflectivity". In: Science 382.6671 (2023), pp. 691–697.

[28] Hongchen Ma et al. "Flexible daytime radiative cooling enhanced by enabling three-phase composites with scattering interfaces between silica microspheres and hierarchical porous coatings". In: ACS Applied Materials & Interfaces 13.16 (2021), pp. 19282–19290.

[29] Shaoning Zeng et al. "Hierarchical-morphology metafabric for scalable passive daytime radiative cooling". In: Science 373.6555 (2021), pp. 692–696.

[30] Jinru Liu et al. "Hierarchical gradient structural porous metamaterial with selective spectral response for daytime passive radiative cooling". In: Advanced Functional Materials 34.45 (2024), p. 2406393.

[31] Lyu Zhou et al. "Graded nanocomposite metamaterials for a double-sided radiative cooling architecture with a record breaking cooling power density". In: arXiv preprint arXiv:2003.10495 (2020).

[32] Qi Sun et al. "Bioinspired all-day adaptive radiative cooler with high-power cooling and efficient suppressing overcooling". In: Building and Environment 266 (2024), p. 112119.

[33] Chenyang Cai et al. “Bioinspired durable daytime radiative cooling wood: realizing outdoor longtime use”. In: Nano Letters 25.11 (2025), pp. 4369–4378.

[34] Juliana Jaramillo-Fernandez et al. “Highly-scattering cellulose-based films for radiative cooling”. In: Advanced Science 9.8 (2022), p. 2104758.

[35] Liao Huang et al. “Designing nanoporous polymer films for high-performance passive daytime radiative cooling”. In: ACS Applied Materials & Interfaces 16.40 (2024), pp. 54401–54411.

[36] Jianing Song et al. “Durable radiative cooling against environmental aging”. In: Nature communications 13.1 (2022), p. 4805.

[37] Po-Chun Hsu et al. “Radiative human body cooling by nanoporous polyethylene textile”. In: Science 353.6303 (2016), pp. 1019–1023.

[38] Giuseppe Emanuele Lio et al. “Nanoporous film layers to enhance the performance of passive radiative cooling paint mixtures”. In: International Journal of Thermophysics 45.11 (2024), p. 153.

[39] Seyed Hamidreza Ghaffar and Mizi Fan. “Structural analysis for lignin characteristics in biomass straw”. In: Biomass and Bioenergy 57 (2013), pp. 264–279. ISSN: 0961-9534. DOI: https://doi.org/10.1016/j.biombioe.2013.07.015. URL: https://www.sciencedirect.com/science/article/pii/S0961953413003395.

[40] Agilent Technologies. Cary 5000 UV-Vis-NIR Spectrophotometer. https://www.agilent.com/en/product/molecular-spectroscopy/uv-vis-uv-vis-nir-spectroscopy/uv-vis-uv-vis-nir-systems/cary-5000-uv-vis-nir. 2025.

[41] SARA LEVORIN. “Optical Characterization and Analysis of Disordered Materials Based on Hollow Silicon Dioxide Microparticles for Passive Daytime Radiative Cooling”. In: ().

[42] Barry R Masters. Fundamentals of Light Microscopy and Electronic Imaging. 2013.

[43] Joseph I Goldstein et al. “Scanning electron microscope (SEM) instrumentation”. In: Scanning Electron Microscopy and X-Ray Microanalysis. Springer, 2017, pp. 65–91.

[44] M. Lin. "11 - Nanotechnology-based approaches for rapid detection of chemical and biological contaminants in foods". In: Nanotechnology in the Food, Beverage and Nutraceutical Industries. Ed. by Qingrong Huang. Woodhead Publishing Series in Food Science, Technology and Nutrition. Woodhead Publishing, 2012, pp. 317–334. ISBN: 978-1-84569-739-6. DOI: https://doi.org/10.1533/9780857095657.2.317. URL: https://www.sciencedirect.com/science/article/pii/B9781845697396500113.

[45] Jeremy Wèrlè et al. "FRESCO-Board: A Low-Cost Open Platform for Comprehensive Testing of Passive Radiative Cooling Materials". In: Available at SSRN 5132927 ().

[46] Mouser Electronics. Semitec JT Series NTC Thermistors. https://eu.mouser.com/c/circuit-protection/thermistors/?m=Semitec&series=JT. 2025.

[47] Futura Group. Sensore di temperatura e umidità DHT22 – FuturaShop. https://futuranet.it/prodotto/sensore-di-temperatura-e-umidita-dht22/?srsltid=AfmBOooDJweOOeMGusfZJoCUkzdpWHqx3P4vMT1-bmtnhlioQi8GzETx. 2025.

[48] Adriano Gandolfo. BH1750 GY-302 Sensore di luce. https://www.adrirobot.it/bh1750-gy-302-sensore-di-luce/. 2025.

[49] Extron Electronics. IR Sensor – Remote IR Receiver. https://www.extron.it/product/irsensor. 2025.

[50] Latief Ahmad et al. "Measurement of Atmospheric Pressure". In: Experimental Agrometeorology: A Practical Manual. Cham: Springer International Publishing, 2017, pp. 75–81. ISBN: 978-3-319-69185-5. DOI: 10.1007/978-3-319-69185-5_11. URL: https://doi.org/10.1007/978-3-319-69185-5_11.

[51] Consorzio LaMMA. Dati stazioni – Osservazioni e dati. https://www.lamma.toscana.it/meteo/osservazioni-e-dati/dati-stazioni. 2025.

[52] Maria-Guglielmina Pelizzo et al. "Enhanced Thermal Emissivity through Boron Nitride Nanofiber Scatterers for Passive Radiative Cooling". In: (2025).

[53] Min Li et al. “Fabrication of fibrous nanofiber membranes for passive radiation cooling”. In: Journal of Materials Science 57.33 (2022), pp. 16080–16090.

[54] Qiaoran Zhang et al. “Highly stable polyimide composite nanofiber membranes with spectrally selective for passive daytime radiative cooling”. In: ACS Applied Materials & Interfaces 16.30 (2024), pp. 40069–40076.

[55] José M Pérez-Escudero et al. “Suppressed-scattering spectral windows for radiative cooling applications”. In: Optics Express 31.4 (2023), pp. 6314–6326.

[56] Junyu Sun et al. “Daytime passive radiative cooling materials based on disordered media: A review”. In: Solar Energy Materials and Solar Cells 236 (2022), p. 111492.

[57] Moladad Nikbakht. “Radiative heat transfer in fractal structures”. In: Physical Review B 96.12 (2017), p. 125436.

Acknowledgments

Thank to Professor Maria and Professor Giuseppe, who have been by my side throughout my studies and whose support I have felt at all times. I am also grateful to the peeople at the CNR-IFN LUXOR laboratory for opening their doors to us throughout our experimental studies and facilitating our work. As with every journey I have taken, I sincerely thank my family, who I felt by my side every moment of my master's adventure.
Also, my deepest gratitude to all my friends I met during this time at university. I would like to thank my dear friend Engin, whose strong support I have always felt and will always feel. Thanks to Mehveş and Eren, with whom I have accumulated endless memories and overcome every hardship. I would also like to thank Ece, Jeremy, Alin and Duru, who were there for me every day and with whom I had so many enjoyable and funny memories.
My dear housemates, I am very grateful to you for the countless conversations we had together and for making me feel at home.
To my best friend and comrade, Görkem, I am so lucky that our paths crossed in high school and that you walked this path with me.
Finally, my deepest gratitude goes to my dear cousin Eren, who has been the greatest witness to every step I have taken since day one and who has helped me realize every dream we have dreamt together.

Padova, 7th October 2025 Atakan Erdogan